Modelling and numerical study of 3D effect on glassy polymer fracture

Shu Guo

N° d'ordre 2013-ISAL-0069 Année 2013

THESE

présentée devant
L'**I**nstitut **N**ational des **S**ciences **A**ppliquées de **Lyon**

pour obtenir
Le grade de Docteur

Ecole doctorale des sciences des matériaux :
Spécialité : Génie des matériaux

Par
Shu GUO

MODELISATION et SIMULATION 3D de la RUPTURE des POLYMERES AMORPHES

Soutenue le 8 juillet 2013 devant la Commission d'examen

Jury MM.

L. DAVID	Pr.	IMP – Université Lyon 1	Président du Jury
L. LAIARINANDRASANA		M.R.(HDR)CDM – EMParis	Rapporteur
F. ZAIRI	M.C. HDR	MDL – Université de Lille 1	Rapporteur
G. PARRY	M.C.	SIMaP – Grenoble-INP	Examinateur
C. OLAGNON	Pr.	MATEIS – INSA Lyon	Examinateur (directeur)
R. ESTEVEZ	Pr.	SIMaP – Université Joseph Fourier	Examinateur

Cette thèse a été préparée au Laboratoire MATEIS (UMR CNRS N° 5510) de L'INSA de Lyon en collaboration avec le SIMaP UMR 5266 de Grenoble-INP

SIGLE	ECOLE DOCTORALE	NOM ET COORDONNEES DU RESPONSABLE
	CHIMIE DE LYON Responsable : M. Denis SINOU	M. Denis SINOU Université Claude Bernard Lyon 1 Lab Synthèse Asymétrique UMR UCB/CNRS 5622 Bât 308 2ème étage 43 bd du 11 novembre 1918 69622 VILLEURBANNE Cedex Tél : 04.72.44.81.83 Fax : 04 78 89 89 14 sinou@univ-lyon1.fr
E2MC	**ECONOMIE, ESPACE ET MODELISATION DES COMPORTEMENTS** Responsable : M. Alain BONNAFOUS	M. Alain BONNAFOUS Université Lyon 2 14 avenue Berthelot MRASH M. Alain BONNAFOUS Laboratoire d'Economie des Transports 69363 LYON Cedex 07 Tél : 04.78.69.72.76 Alain.bonnafous∂ish-lyon.cnrs.fr
E.E.A.	**ELECTRONIQUE, ELECTROTECHNIQUE, AUTOMATIQUE** M. Daniel BARBIER	M. Daniel BARBIER INSA DE LYON Laboratoire Physique de la Matière Bâtiment Blaise Pascal 69621 VILLEURBANNE Cedex Tél : 04.72.43.64.43 Fax 04 72 43 60 82 Daniel.Barbier@insa-lyon.fr
E2M2	**EVOLUTION, ECOSYSTEME, MICROBIOLOGIE, MODELISATION** **http://biomserv.univ-lyon1.fr/E2M2** **M. Jean-Pierre FLANDROIS**	M. Jean-Pierre FLANDROIS UMR 5558 Biométrie et Biologie Evolutive Equipe Dynamique des Populations Bactériennes Faculté de Médecine Lyon-Sud Laboratoire de Bactériologie BP 1269600 OULLINS Tél : 04.78.86.31.50 Fax 04 72 43 13 88 E2m2∂biomserv.univ-lyon1.fr
EDIIS	**INFORMATIQUE ET INFORMATION POUR LA SOCIETE** http://www.insa-lyon.fr/ediis M. Lionel BRUNIE	M. Lionel BRUNIE INSA DE LYON EDIIS Bâtiment Blaise Pascal 69621 VILLEURBANNE Cedex Tél : 04.72.43.60.55 Fax 04 72 43 60 71 ediis@insa-lyon.fr
EDISS	**INTERDISCIPLINAIRE SCIENCES-SANTE** http://www.ibcp.fr/ediss M. Alain Jean COZZONE	M. Alain Jean COZZONE IBCP (UCBL1) 7 passage du Vercors 69367 LYON Cedex 07 Tél : 04.72.72.26.75 Fax : 04 72 72 26 01 cozzone@ibcp.fr
	MATERIAUX DE LYON http://www.ec-lyon.fr/sites/edml M. Jacques JOSEPH	M. Jacques JOSEPH Ecole Centrale de Lyon Bât F7 Lab. Sciences et Techniques des Matériaux et des Surfaces 36 Avenue Guy de Collongue BP 163 69131 ECULLY Cedex Tél : 04.72.18.62.51 Fax 04 72 18 60 90 Jacques.Joseph@ec-lyon.fr
Math IF	**MATHEMATIQUES ET INFORMATIQUE FONDAMENTALE** http://www.ens-lyon.fr/MathIS M. Franck WAGNER	M. Franck WAGNER Université Claude Bernard Lyon1 Institut Girard Desargues UMR 5028 MATHEMATIQUES Bâtiment Doyen Jean Braconnier Bureau 101 Bis, 1er étage 69622 VILLEURBANNE Cedex Tél : 04.72.43.27.86 Fax : 04 72 43 16 87 wagner@desargues.univ-lyon1.fr
MEGA	**MECANIQUE, ENERGETIQUE, GENIE CIVIL, ACOUSTIQUE** http://www.lmfa.ec-lyon.fr/autres/MEGA/index.html M. François SIDOROFF	M. François SIDOROFF Ecole Centrale de Lyon Lab. Tribologie et Dynamique des Systèmes Bât G8 36 avenue Guy de Collongue BP 163 69131 ECULLY Cedex Tél :04.72.18.62.14 Fax : 04 72 18 65 37 Francois.Sidoroff@ec-lyon.fr

A mes parents, à mon frère

Remerciements

L'étude présentée dans ce mémoire a été réalisée au Laboratoire de Groupe d'Etudes de Métallurgie Physique et de Physique des Matériaux (GEMPPM) de l'INSA de LyonPr. Je remercie le professeur Jean-Yves CAVAILLE directeur du GEMPPM pour m'avoir accueillie au sein du laboratoire.

Mes plus vifs remerciements vont à Rafael ESTEVEZ et Christian OLAGNON, directeurs de thèse. Merci d'avoir été toujours disponibles malgré les nombreuses autres responsabilités, pour m'avoir soutenu tout au long de ce travail avec patience, intérêt et compétence. Ce travail leur doit beaucoup, moi aussi. Je remercie également Roland SEGUELA pour sa contribution constructive à l'avancement de ce travail.

Je suis profondément reconnaissante à Monsieur Costantino CRETON et Madame Noëlle BILLON d'avoir accepté d'être les rapporteurs de ce travail. Je remercie également Messieurs Hans-Henning KAUSCH, Henry SAUTERAU et Laurent CANGEMI pour s'être intéressés à ce travail et pour leur participation à ce jury.

Je voudrais remercier tous les membres du GEMPPM et plus particulièrement Guy MASSAL et Jacques BIGOT pour leurs aides précieuses à la réalisation d'éprouvettes d'essais.

Enfin, je ne saurais oublier de remercier et d'exprimer ma gratitude à toute ma famille :ma mère, ma sœur et mon mari avec une mention particulière à mon fils Ezzeddine « Zizou » pour m'avoir comblée d'amour et d'espoir. Merci également à mes amis: Ali, Nadia, Emilie, Elodie, Adel, Sondess, Marcos et Lassad pour leurs soutiens moral et leurs encouragements.

GENERAL INTRODUCTION

Fracture in glassy polymers is governed by the competition between shear yielding and crazing. Shear yielding is observed corresponds to the localization of the plastic deformation with a softening upon yielding followed by progressive hardening at continued deformation. In ductile polymers like polycarbonate (PC), shear yielding appears in tension by the propagation of necking across the material. For fracture specimens, shear yielding takes place in the form of shear bands similar to Hill's slip line fields [HIL50, LAI97]. The specific mechanical response of glassy polymers is intrinsically prone to strain localization. The shape of the plastic zone depends on the test geometry, with necking in uniaxial tension and shear bands in crack tip plasticity. However, for thin sample and in polymer film, a flame like plastic zone with no evidence of shear banding is observed [HAS00, COR07]. It appears that plasticity in ductile polymers depends on the stress triaxiality as the thickness varies for a given geometry.

Crazing is the mechanism underlying failure with three stages [KAU83, KAU90] consisting in (i) initiation for a local critical stress, (ii) craze thickening with the development of a web of craze fibrils up to (iii) their breakdown and the nucleation of a crack locally. Crazing is also a mechanism involving localized plasticity, although at a smaller scale, as the maximum craze opening is of the order of some microns in glassy polymers.

Both mechanisms are known to be pressure dependent with an asymmetric yield stress between tension and compression of the bulk and a mean stress dependence of the craze initiation conditions. In the literature, the investigations of the bulk plasticity initiated with 2D analysis [ISH77, LAI97] and during the last decade, 3D calculations have been reported [GEA04, KAT13]. The analysis of crazing still remains restricted to 2D analysis, generally under the assumption of plane strain conditions [TIJ00, EST00], for brittle materials like PMMA [SAA06] or polystyrene. However, in ductile polymer fracture, and in more general terms the mechanical response of polymer based composite for which the resistance to fracture is promoted by voiding of rubber particles, the resistance to fracture of PC-like material is intrinsically a 3D problem. The distribution of the mean stress and the stress triaxiality between the shear stress to the mean stress governs the fracture characteristics. Recent studies [GEA04, KAT13] attempt to investigate the competition between the bulk plasticity and failure when a critical plastic stretch of a critical mean stress is attained, by performing a 3D continuum analysis with a realistic constitutive law for the bulk. The use of a fracture criterion based on a critical mean stress or critical plastic stretch is able to qualitatively predict failure by ductile tearing in thin samples or by crazing in thick specimens.

The present work extends these studies by performed a detailed analysis of the crack tip fields observed in ductile polymer fracture. The specific constitutive law for glassy polymers is accounted for and implemented in a UserMATerial in Abaqus [ABA10]. A simple cohesive model for crazing is adopted so that the competition with bulk plastic deformation is investigated for all specimens' geometry and in particular samples as thin as 0.25 mm to 10mm thick. A blunt notch is considered with radius R=0.25mm. This is motivated by practical aspects in the preparation of the fracture tests: reproducible sharp cracks are difficult to machine while well controlled blunt notch can be machined.

The motivation of the present study is to gain insight on the appropriate specimen geometry for the estimation of the material's toughness and also to discuss whether or not simple criteria used in [GEA04,KAT13] are relevant.

INTRODUCTION

In this chapter, we review the models available for the description of constitutive laws for glassy amorphous polymers. The description of fracture by crazing is also reported. Recent investigations of 3D effects are presented which conclude this chapter.

Table of contents

I. Introduction 1

Table of contents 2

I.1. Introduction 3

I.2. Viscoplastic Deformation of Amorphous Polymers 4

I.3. Fracture in glassy polymers by crazing 9

I.3.1. Craze initiation 9

I.3.2. Craze thickening 11

I.3.3. Craze breakdown 13

I.4. Cohesive surface model for crazing 19

I.4.1. Craze initiation 20

I.4.2. Craze thickening 21

I.4.3. Craze breakdown 21

I.4.4. Traction versus thickening law for the cohesive surfaces 22

I.4.5. Alternative descriptions 25

I.5. 3D effects in mechanical response of glassy polymers 26

I.1. Introduction

Amorphous polymers exhibit two mechanisms of localized plasticity: crazing and shear yielding. These are generally thought of separately with crazing corresponding to a brittle response while shear yielding is associated to ductile behavior with the development of noticeable plastic deformation prior to fracture. Shear yielding is plastic flow localized in a shear band caused by the inherent strain softening after yield followed by re-hardening at continued deformation. Crazing is also a mechanism of localized plasticity but at a different scale, and has a distinctly different appearance. Crazes are planar crack-like defects but unlike cracks, the craze surfaces are bridged with polymer fibrils resulting in some load-bearing ability. Following the presently available description of crazing, we present how it can be modeled by cohesive surfaces. The related constitutive response is written in terms of a traction-opening law which incorporates the stress-state dependence for initiation, the rate dependent thickening during fibrillation and the fibril breakdown for a critical craze thickness.

Most of the analyses of crazing found in the literature so far assume that the bulk surrounding the craze remains elastic. This assumption is certainly a limitation to the analysis of glassy polymers fracture since crazing and shear yielding can appear simultaneously [ISH77]. Since both are rate-dependent processes, the competition between their kinetics for a given loading (defined by its level and its rate) is expected to control which mechanism is developing first and dominates, thus defining a ductile or brittle response.

We present recent results on the analysis of the interaction between plasticity and crazing at the tip of a pre-existing crack under mode I loading conditions. Illustrations of the competition between these mechanisms are obtained from a finite element model in which a cohesive surface is laid out in front of the crack.

As the loading rate increases, thermal effects need to be accounted for and the analysis is extended to a coupled thermo-mechanical framework. Evidence of temperature effects in glassy polymer fracture is found e.g. in [DOL73, FUL75] with a temperature increase beyond the glass transition temperature T_g . The influence of thermal effects on the fracture process is also reported.

Tensors are denoted by bold-face symbols, $\otimes$ is the tensor product and $\bullet$ the scalar product. For example, with respect to a Cartesian basis $\boldsymbol{e}_i$, $\boldsymbol{AB} = A_{ik}B_{kj}\boldsymbol{e}_i \otimes \boldsymbol{e}_j$, $\boldsymbol{A} \bullet \boldsymbol{B} = A_{ij}B_{ij}$ and $\boldsymbol{C}^{\mathrm{e}}\boldsymbol{B} = C^{\mathrm{e}}_{ijkl}B_{kl}\,\boldsymbol{e}_i \otimes \boldsymbol{e}_j$, with summation implied over repeated Latin indices. The summation convention is not used for repeated Greek indices.

I.2. Viscoplastic Deformation of Amorphous Polymers

We present a constitutive model for amorphous polymers in their glassy state ($T<T_g$) when no crazing take place (like in shear or in compression). The formulation is supplemented with a simple description of the material response when the temperature gets higher than T_g as found experimentally to occur at sufficiently high loading rates [DOL73, FUL75]. Therefore, two descriptions for the viscoplastic response of amorphous polymers are used, depending on the temperature. The two viscoplastic processes are described within the same framework.

Following the original ideas due to Haward and Thackray [HAW68], the three dimensional basis for modeling the deformation of glassy polymers is due to Boyce et al. [BOY88]. The constitutive model is based on the formulation of Boyce et al. [BOY88] but we use a modified version introduced by Wu and Van der Giessen [Wu93]. Details of the governing equations and the computational aspects are presented by Wu and Van der Giessen in [Wu96]. The reader is also referred to the review by Van der Giessen [VAN97] together with a presentation of the thermomechanical framework in [BAS02].

The constitutive model makes use of the decomposition of the rate of deformation $\boldsymbol{D}$ into an elastic, $\boldsymbol{D}^e$, and a plastic part, $\boldsymbol{D}^p$, as $\boldsymbol{D}=\boldsymbol{D}^e+\boldsymbol{D}^p$. Prior to yielding, no plasticity takes place and $\boldsymbol{D}^p=0$. In this regime, most amorphous polymers exhibit visco-elastic effects but these are neglected here since we are primarily interested in those of the bulk plasticity. Assuming the elastic strains and the temperature differences (relative to a reference temperature T_0) to remain small, the thermoelastic part of the response is expressed by the hypoelastic law

$$\overset{\nabla}{\boldsymbol{\sigma}} = \boldsymbol{C}_e \boldsymbol{D}^e - K\alpha_c \dot{T}\boldsymbol{I}\,, \tag{1}$$

where $\overset{\nabla}{\boldsymbol{\sigma}}$ is the Jaumann rate of the Cauchy stress, $\boldsymbol{C}_e$ the usual fourth-order isotropic elastic modulus tensor. The coefficients K and α_c are the bulk modulus and the coefficient of cubic thermal expansion, respectively. Assuming that the yield response is isotropic, the isochoric plastic strain rate $\boldsymbol{D}^p$ is given by the flow rule

$$\boldsymbol{D}^p = \frac{\dot{\gamma}^p}{\sqrt{2}\tau}\bar{\boldsymbol{\sigma}}'\,, \tag{2}$$

which is specified in terms of the equivalent shear strain rate $\dot{\gamma}^p = \sqrt{\boldsymbol{D}^p \bullet \boldsymbol{D}^p}$, the driving stress $\bar{\boldsymbol{\sigma}} = \boldsymbol{\sigma} - \boldsymbol{b}$ and the related equivalent shear stress $\tau = \sqrt{1/2\,\bar{\boldsymbol{\sigma}}' \bullet \bar{\boldsymbol{\sigma}}'}$. The back stress tensor $\boldsymbol{b}$ describes the progressive hardening of the material as the strain increases and will be defined later on.

The equivalent shear strain rate $\dot{\gamma}^p$ is taken from Argon's expression [ARG73]

$$\dot{\gamma}^{\mathrm{p}} = \dot{\gamma}_0 \exp\left[-\frac{As_0}{T}\left\{1-\left(\frac{\tau}{s_0}\right)^{5/6}\right\}\right] \quad \text{for } T<T_{\mathrm{g}}\,, \tag{3}$$

where $\dot{\gamma}_0$ and A are material parameters and T the absolute temperature (note that plastic flow is inherently temperature dependent through Eq. (3)). In Eq. (3) the shear strength s_0 is related to elastic molecular properties in Argon's original formulation but is considered here as a separate material parameter. In order to account for the effect of strain softening and for the pressure dependence of the plastic strain rate, s_0 in (3) is replaced by $s+\alpha p$, where α is a pressure sensitivity coefficient and $-p = 1/3\ \mathrm{tr}(\boldsymbol{\sigma})$. Boyce et al. [5] have suggested a modification of (3) to account for intrinsic softening by substituting s_0 with s which evolves from the initial value s_0 to a steady state value s_{ss} according to $\dot{s} = h\left(1-s/s_{\mathrm{ss}}\right)\dot{\gamma}^{\mathrm{p}}$, with h controlling the rate of softening. The energy dissipation rate per unit volume is given by

$$\dot{D} = \bar{\boldsymbol{\sigma}}' \bullet \boldsymbol{D}^{\mathrm{p}} = \sqrt{2}\tau\dot{\gamma}^{\mathrm{p}}\,. \tag{4}$$

The constitutive model is completed by the description of the progressive hardening of amorphous polymers upon yielding due to deformation-induced stretch of the molecular chains. This effect is incorporated through the back stress $\boldsymbol{b}$ in the driving shear stress τ in Eq. (2). Its description is based on the analogy with the stretching of the cross-linked network in rubber elasticity, but with the cross-links in rubber being replaced with the physical entanglements in a flowing amorphous glassy polymer [BOY88]. The deformation of the resulting network is assumed to be affine with the accumulated plastic stretch [Wu93] so that the principal back stress components b_α are functions of the principal plastic stretches λ_β as

$$\boldsymbol{b} = \sum_\alpha b_\alpha (\boldsymbol{e}_\alpha^{\mathrm{p}} \otimes \boldsymbol{e}_\alpha^{\mathrm{p}}),\quad b_\alpha = b_\alpha(\lambda_\beta)\,, \tag{5}$$

in which $\boldsymbol{e}_\alpha^{\mathrm{p}}$ are the principal directions of the plastic stretch. In a description of the fully three-dimensional orientation distribution of non-Gaussian molecular chains, Wu and Van der Giessen [Wu93] showed that $\boldsymbol{b}$ can be estimated accurately with the following combination of the classical three-chain model and the eight-chain description of Arruda and Boyce [ARR93]:

$$b_\alpha = \left(1-\xi\right) b_\alpha^{\text{3-ch}} + \xi b_\alpha^{\text{8-ch}}\,, \tag{6}$$

where the fraction $\xi = 0.85\bar{\lambda}/\sqrt{N}$ is based on the maximum plastic stretch $\bar{\lambda} = \max(\lambda_1, \lambda_2, \lambda_3)$ and on N, the number of segments between entanglements. The use of Langevin statistics for calculating b_α implies a limit stretch of $\sqrt{N}$. The expressions for the principal components of $b_\alpha^{\text{3-ch}}$

and $b_\alpha^{8\text{-ch}}$ contain a second material parameter: the initial shear modulus $C^R = nk_BT$, in which n is the volume density of entanglements (k_B is the Boltzmann constant).

Based on a study of the temperature dependence of strain-induced birefringence in amorphous polymers, Raha and Bowden [RAH72] suggested that the thermal dissociation of entanglements can be described by

$$n(T) = B - D\exp\left(-E_a / \mathrm{R}T\right) \tag{7}$$

In the above expression, E_a is the dissociation energy, R is the gas constant, while B and D are material parameters. Such evolution of the entanglement density is used to model a reduction of the hardening with temperature. As pointed out by Arruda et al. [ARR95], this evolution law is subject to the side condition nN=constant in order to keep the number of molecular links constant. Therefore, the back stress according to (5) is also temperature dependent through $N(T)$ and $C^R = n(T)k_BT$. The material parameters B and D are estimated here from the assumption that the back stress vanishes as the temperature approaches T_g, resulting in $n(T_g) = 0$ so that $B/D = \exp(-E_a / \mathrm{R}T_g)$.

The formulation above is assumed to hold for temperatures up to the glass transition T_g. For $T > T_g$, most studies found in the literature focus on the description of the molten state [AGA 91] due to its practical importance while little attention is paid to the response of glassy polymers in the rubbery state, near T_g. For strain rates larger than 1 s^{-1}, the mechanical response of the molten material is non-Newtonian for most polymers and described by $\tau = \eta\dot{\gamma}^m$, where η and m are material parameters. We assume that this non-Newtonian response prevails as soon as T_g is exceeded. Hence, within the same framework as used below T_g, the equivalent plastic strain rate (3) is replaced by

$$\dot{\gamma}^p = \dot{\gamma}_0 \aleph \left(\frac{\tau}{s_0}\right)^{1/m} \quad \text{for } T \geq T_g. \tag{8}$$

In this expression, η has been substituted for convenience by $\eta = s_0 / \left(\aleph\dot{\gamma}_0\right)^m$ with s_0 and $\dot{\gamma}_0$ being below-T_g parameters in (3), and $\aleph$ a non-dimensional constant. The deformation in the molten state is generally believed to involve chain slippage and temporary entanglements between the moving chains resulting in the non-Newtonian viscosity [AGA 91]. The details of the deformation process are lumped into the parameters η (or $\aleph$) and m so that no back stress contribution is considered above T_g: $\bar{\boldsymbol{\sigma}} \equiv \boldsymbol{\sigma}$ and $\tau = \sqrt{1/2\,\boldsymbol{\sigma}\bullet\boldsymbol{\sigma}}$.

The exponent *m* is observed to vary between 0.3 and 1 for molten polymers [AGA91] but for those exhibiting a marked non-Newtonian response like most glassy polymers, *m* ranges from 0.3 to 0.5; the value $m = 0.4$ is adopted here. For a given temperature, the evolution of the viscosity η with increasing strain rate is observed to decrease from a Newtonian value η_0 at low strain rates to a level five or six decades smaller [AGA91,VAN90]. For a temperature around T_g, the value of η_0 can be estimated from [VAN90] to be of the order of some MPa.s for materials like PMMA or PC. A smaller value is expected in the non-Newtonian regime so that for temperatures above T_g, a constant value of η=0.35 MPa.s ($\aleph = 0.02$) is used to describe the material response in the molten state. With this simple description, we only aim at being able to continue our calculations if the temperature exceeds T_g locally, which may happen during crack propagation at high loading rates. We need to keep in mind that we are primarily concerned with temperatures below T_g and the incorporation of more sophisticated models as found in [AGA91,VAN90] is out of the scope of the present investigation.

Figure 1 shows the response to simple shear that is obtained with the constitutive model described above under isothermal and adiabatic conditions i.e. when the energy originating from the viscoplasticity is dissipated into heat as

$$\rho c_v \dot{T} = \dot{D}, \tag{9}$$

in which $\dot{D}$ is defined in Eq. (4), ρ is the volume density and c_v the specific heat. The temperature increase reduces the re-hardening due to the back stress tensor $\boldsymbol{b}$ since the entanglement density *n* decreases with increasing temperature (see Eq. (7)) thus resulting in a higher maximum stretch $\sqrt{N}$ of the molecular strands .

The material parameters used are given in Table 1 and are representative of SAN. The parameters involved in adiabatic analyses (9) are reported in Table 2 and are expected to be representative for glassy polymers. For the lowest shear strain rate of 10^{-4}/s, adiabatic conditions moderately affect the orientational hardening which appears for a slightly larger deformation. As the loading rate is about 10^{-2}/s or higher, the final hardening is suppressed and the glass transition temperature is reached locally, corresponding to the loss of any load-bearing capacity of the material. It is unlikely that adiabatic conditions are met for a strain rate of 10^{-2}/s but as long as temperature effects need to be considered, this figure shows that the material may not harden, even for large deformations.

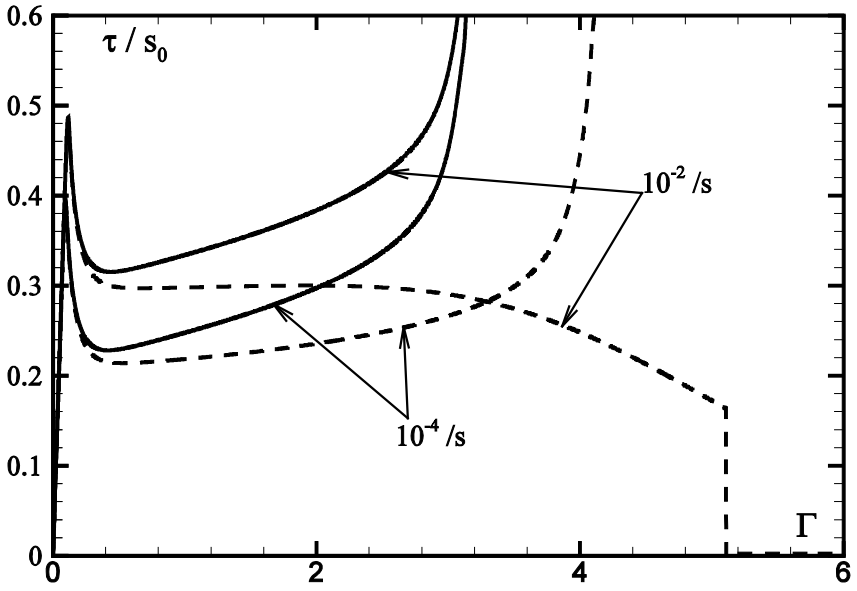

Figure 1: mechanical response of SAN to simple shear at an applied strain rate of 10^{-2}/s and 10^{-4}/s for isothermal or adiabatic conditions (solid and dashed lines resp.). The temperature increase delays the hardening for a strain rate of 10^{-4}/s which vanishes for 10^{-2}/s. In this case, the material reaches the glass transition temperature and enters the rubbery state resulting in a small load-bearing capacity.

	E/s_0	ν	s_{ss}/s_0	As_0/T	h/s_0	α	N	C^R/s_0	$\aleph$	m
SAN	12.6	0.38	0.79	52.2	12.6	0.25	12.0	0.033	0.02	0.4

Table 1: the set of parameters used for the description of the bulk response representative of SAN at room temperature supplemented with $\aleph$ and m involved in the description for $T>T_g$.

E_a/R	k	α_c	ρ	c_v
2.8×10^3K	0.35 W/mK	2×10^{-4}K^{-1}	1.08×10^{-3}kg/m^3	1.38×10^3J/kg K

Table 2: the set of parameters used in the thermal part of the analysis from Ref.[BAS02] and standard for glassy polymers.

I.3. Fracture in glassy polymers by crazing

Since early investigations of glassy polymer fracture, as reviewed in [KAM73], crazing is recognized as the mechanism preceding the nucleation of a crack. The major advances in the description of the crazing process are thoroughly presented in two volumes of the present series [KAU83, KAU90]. The mechanism of crazing involves three stages (see [KAM73, KAU87, KAU83, KAU90]): (i) initiation, (ii) thickening of the craze surfaces, (iii) breakdown of the craze fibrils and creation of a crack. The description presented here is phenomenological since the model is motivated by the mechanical considerations and the molecular aspects (e.g. the molecular weight or the entanglement density) are generally not incorporated.

Because crazing is a precursor to failure, pioneering studies on crazing have focused on the condition for craze initiation. Later on, the estimation of the toughness has motivated the examination of the craze thickening and the condition for the craze breakdown.

We present the major results established in the description of crazing and the recent developments in this field. Crazing has been investigated within continuum or discrete approaches (e.g. spring networks or molecular dynamics calculations to model the craze fibrils) which have provided phenomenological or physically based descriptions. Both are included in the presentation of the crazing process, since they will provide the basis for the recent cohesive surface model used to represent crazing in a finite element analysis [TIJ00, TIJ00b, EST00].

I.3.1. **Craze initiation**

The physical mechanism for craze initiation is not yet clearly identified and various criteria have been proposed depending on the assumed mechanism and length scale for its description. Experimentally, one observes an incubation time for craze formation when constant stress smaller than approximately half of the yield stress is applied. The total amount of craze nuclei reaches a saturation value which increases with applied stress [KAM73, ARG77]. For these stress levels, the incubation time can be greater than 100 s and this time decreases with increasing stress. Above half of the yield stress, the incubation time becomes negligible [ARG77]. Based on these observations and borrowing some ideas of ductile failure in metals, Argon and Hannoosh [ARG77] have developed a sophisticated criterion for time dependent craze initiation, which includes a negligible influence of time when the stress level is larger than half the yield stress. In this case the criterion reduces to

$$\left|\sigma_{\max} - \sigma_{\min}\right| = \frac{A}{C + 3\sigma_{\mathrm{m}} / 2\sigma_{\mathrm{y}} Q} \tag{10}$$

in which σ_{max} and σ_{min} refer to the maximum and minimum principal stresses, $\sigma_m = 1/3\,\mathrm{tr}\,\boldsymbol{\sigma}$ is the mean stress, A and C are material parameters while $Q = 0.0133$ is a factor controlling the dependence of the critical shear stress on the mean stress and σ_y is the tensile yield stress of the material [ARG77]. It is shown in [TIJ00] that the criterion (10) shows predictions for craze initiation under tension similar to those provided by a formulation based on stress bias conditions as used by Sternstein [STE69, STE73].

The stress bias criterion [STE69, STE73] refers implicitly to two mechanisms of micro-voids formation in a dilatational stress field and stabilization of the micro-voids through a deviatoric stress component and local plasticity. Its definition is

$$\sigma_b = |\sigma_1 - \sigma_2| \geq A^0 + \frac{B^0}{I_1}, \tag{11}$$

in which σ_b is a stress bias depending on the first stress invariant I_1. Crazing initiates for a positive I_1 and the plane of craze initiation is perpendicular to the direction of maximum principal stress σ_1. Sternstein et al. [STE 69] derive the above expression from experiments in which crazing initiates in the vicinity of a hole drilled in a thin plate of PMMA for which the principal stresses are $\sigma_1 > \sigma_2 > \sigma_3 = 0$. In a subsequent analysis on thin cylinders under combined tension and torsion loadings, the above formulation is observed to agree with experimental observations of craze initiation when $\sigma_1 > \sigma_3 = 0 > \sigma_2$, with σ_2 being the smaller stress in this case. This is pointed out by Oxborough and Bowden [OXB73] who suggested to define a critical strain as $\varepsilon_c \geq X + Y/\sigma_m$, which is also hydrostatic stress dependent. This criterion can be reformulated for an elastic material with ν being the Poisson coefficient and E the Young's modulus as

$$\sigma_1 - \nu\sigma_2 - \nu\sigma_3 \geq X' + \frac{Y'}{I_1}, \tag{12}$$

where $X' = EX$ and $Y' = EY$.

The criteria (11) and (12) are similar and are derived from studies on materials that are elastic at initiation of crazing while more ductile materials like polycarbonate show a more pronounced sensitivity to the hydrostatic tension. This has been found experimentally by Ishikawa and coworkers in [ISH77, ISH83] for notched specimens of polycarbonate. Crazing appears ahead of the notch root, at the intersection of well developed shear bands. From a slip line field analysis, the tip of the plastic zone corresponds to the location of the maximum hydrostatic stress. This has been confirmed by Lai and Van der Giessen [VAN97] with a more realistic material constitutive law. Therefore, Ishikawa and

coworkers [ISH77, ISH83] have suggested the use of a criterion for initiation based on a critical hydrostatic stress. Such a stress state condition can be expressed in (11) with $\sigma_b = 0$ and $I_1^{cr} = B^0 / A^0$. Thus, the criterion (11) can be considered general enough to describe craze initiation in many glassy polymers. For the case of polycarbonate, a similar criterion is proposed in [GEA04] as

$$\sigma_1^{cr} = A + \frac{B}{I_1} \tag{13}$$

in which σ_1^{cr} is the maximum principal stress, *A* and *B* are material parameters. The criterion (13) is indeed very similar to (11) or (12). As long as a better fundamental understanding of craze initiation is pending, the choice of which criterion to adopt is essentially dependent on the ability of capturing experimental results.

I.3.2. **Craze thickening**

Descriptions of craze thickening are based on the observed crazes at the tip of stationary crack tip for creep tests [DOL83, DOL 90] and on observations of crazes in thin films by transmission electronic microscopy (TEM) or small angle X-Rays scattering (SAXS) [KRA83, KRA90].

Döll and coworkers [DOL83, DOL90] have used interferometry to measure the evolution of craze length and craze thickness with time under constant load. By using the Dugdale plastic zone [DUG60] concept for the description of the craze at a stationary crack tip, the craze thickness and the craze length were observed to increase slightly up to 10^5 s and markedly for larger loading times [DOL83, DOL90]. The craze stress acting on the craze surfaces derived from the Dugdale analysis was observed to decrease with time while thickening continues [DOL83, DOL90], thus suggesting that crazing is a time dependent process. Before details of the craze microstructure provided by TEM [LAU79] or SAXS [BRO81] were available, extension of craze fibrils was thought to proceed by creep [KAM73]. If the latter mechanism is operating during craze thickening, it would result in a variation of the craze density along the craze length, since the craze material just after initiation is expected to have a higher density than in regions with longer craze fibrils. Such a variation of the volume fraction of the craze is not seen in TEM observations of crazes in thin films [KRA83, KRA90]. Instead, it has been found that the craze microstructure consists approximately of cylinders with a diameter $D \approx$5-15 nm for 'mature' fibrils, while those at the craze tip are thought to have an initial diameter of $D_0 \approx$20-30 nm, depending on the material [KRA83, KRA90]. Following Kramer [KRA83, KRA90], the diameter D_0 of the primitive fibrils is assumed to be approximately the fibril spacing in Fig. 2.

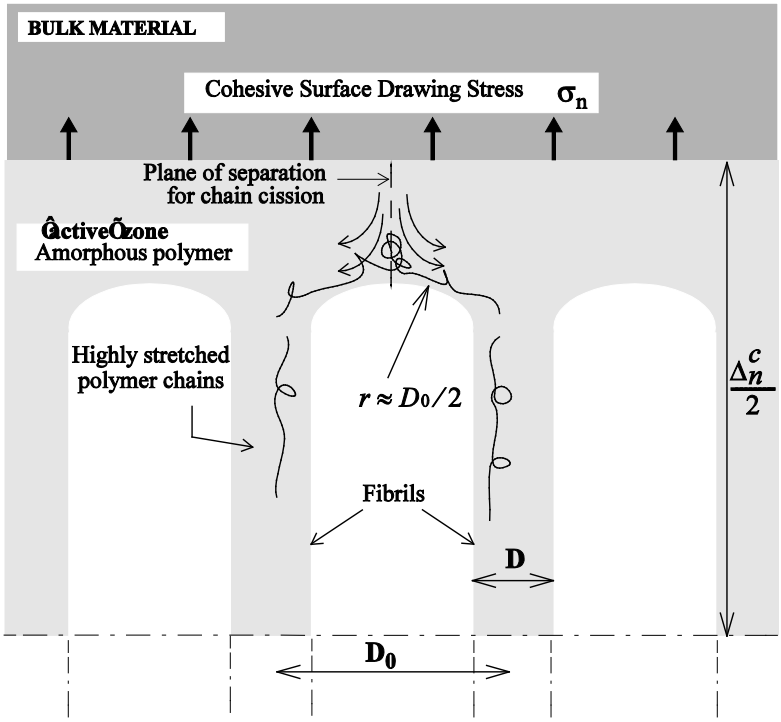

Figure 2: Description of the craze thickening process according to Kramer [KRA83] as drawing-in new polymers chains from the craze/bulk interface into the fibrils. The fibrils have a diameter D and distance of D_0.

These observations appear to be in contradiction with a creep mechanism for craze fibrillation and the currently accepted description refers to the drawing-in mechanism due to Kramer [KRA83, KRA90]. Kramer argued that fibrillation takes place within a thin layer (about 50 nm) at the craze-bulk interface in which the polymer deforms into highly stretched fibrils similar to the mechanism of drawing of polymer fibers, as illustrated in Fig. 2. Craze thickening is then a consequence of large viscoplastic deformations inside this 'active' plastic zone at the craze bulk interface. During fibrillation, stretching of the polymer chains is thought to be combined with chain scission and disentanglement along a plane of separation located at the top of the craze void. Craze fibrils are not only made of parallel cylinders perpendicular to the craze surfaces but lateral cross-tie fibrils connect the main fibrils. Kramer and Berger [KRA90] suggested that these cross-tie fibrils originate at the plane of separation, when disentanglement is not complete so that fibrillation results in a chain that belongs to two main fibrils.

The deformation of the polymer within a thin active zone was originally represented by a non-Newtonian fluid [KRA83] from which a craze thickening rate is thought to be governed by the pressure gradient between the fibrils and the bulk [KRA83, KRA90]. A preliminary finite element analysis of the fibrillation process which uses a more realistic material constitutive law [VAN97] is not fully consistent with this analysis. In particular, chain scission is more likely to occur at the top of

the fibrils where the stress concentrates rather than at the top of the craze void as suggested in [KRA90]. A mechanism of local cavitation can also be invoked for cross-tie generation [TIJ02].

More work on a detailed description of the fibrillation process is needed to clarify the underlying mechanism and its relationship with molecular aspects as the entanglement density or the molecular mobility. Nevertheless, based on the observations reported by Döll [DOL83, DOL90] of time dependent craze stress and Kramer's [KRA83, KRA90] description of fibrillation involving an 'active' plastic zone, one can conclude that craze thickening is a viscoplastic process.

I.3.3. **Craze breakdown**

Following the studies on craze initiation, several efforts have focused on the description of glassy polymer fracture, and especially on the characteristics of a craze developed at a crack tip. Kambour (see [KAM73]) has shown that the length and thickness of a craze developed at the tip of a pre-existing crack can be measured by interferometry and quantitative predictions have been reported in [DOL83, DOL90, BRO73].

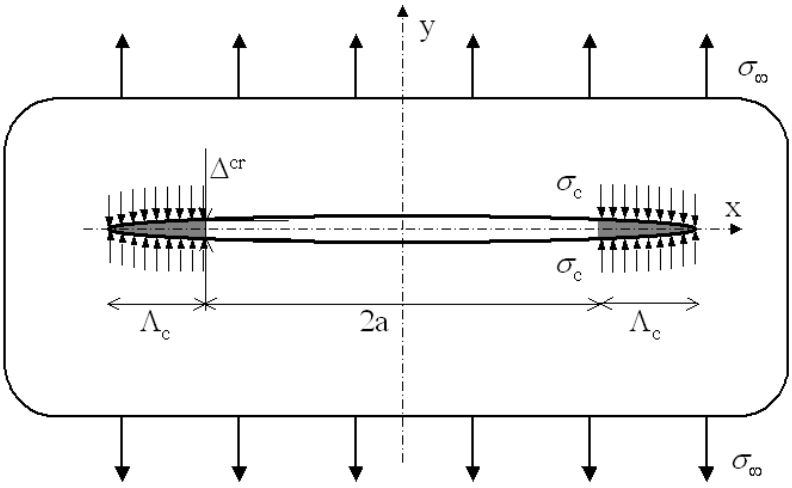

Figure 3: schematic of the Dugdale model. The plastic zone is modeled by a strip subjected to a constant normal stress σ_c. The length of the crack is 2*a* and the size of the plastic zone ahead of the crack tip is Λ_c.

The measure of the craze shape ahead of a propagating crack by Brown and Ward [BRO73] appears consistent with the geometry of the 'plastic' zone according to a Dugdale [KRA90] model of a craze. For a pre-cracked specimen under the remote load σ_∞ (Fig. 3), the craze is represented by plastic zone similar to a strip at the tip of the crack. The profile of the plastic zone varies from zero at the location $(a+\Lambda_c)$ to the value Δ^{cr} at the crack tip.

Typical values for crazes in glassy polymers [DOL83, DOL90, BRO73] are a few microns in thickness with tenths of millimeters in length. The measures of Δ^{cr} and Λ_c are used by Brown and Ward [BRO73] to estimate the toughness and the craze stress. On the other hand, the observation of a constant critical thickness Δ^{cr} at the tip of running crack [DOL83, DOL90, BRO73] has motivated the definition of a fracture criterion based on this parameter for crack propagation (e.g. in [MAR74, WIL84]). In PMMA with a high molecular weight (M_w=2×10^{6}g/mol), the measured critical craze thickness [DOL79] at the tip of moving cracks is observed to be approximately constant for crack velocities ranging from 10^{-8}mm/s to 20 mm/s, so that the crack velocity moderately affects the critical craze opening.

Depending on the material, a critical molecular weight for the observation of a stable craze has been found, for PMMA [DOL83, DOL90] and for polycarbonate [PIT79]. Below this critical value, crazes are not seen by interferometry and the material is very brittle. The molecular weight has to be sufficiently large (about M_w=3×10^{5}g/mol for PMMA and M_w=12×10^{3}g/mol for PC), for the development of a stable craze. The critical craze thickness and craze length (Δ^{cr} and Λ_c) are also temperature dependent [DOL83, DOL90, MOR77, WEI78] and this effect is amplified with increasing molecular weight [DOL83, DOL90].

Based on the description of craze thickening due to Kramer et al. [KRA 83, KRA 90], Schirrer [SCH90] proposed a phenomenological viscoplastic formulation for the 'fibril drawing velocity' similar to the Eyring model as

$$V_e = V_{e0} \exp\left(\frac{\sigma_c}{\sigma_V}\right), \tag{14}$$

in which σ_c in the craze stress and σ_V a reference stress (so that $1/\sigma_V$ refers to some activation volume). The maximum craze thickness is obtained by integration of the thickening velocity in (14) up to a critical time or 'lifetime' for the fibrils inside the craze. The lifetime is determined experimentally as $\tau_0 = \Lambda_c / \dot{a}$, in which Λ_c the craze length and $\dot{a}$ the crack velocity. This parameter is assumed to be stress dependent as

$$\tau_0 = \tau_{0i} \exp\left(\frac{-\sigma_c}{\sigma_t}\right) \tag{15}$$

similar to that of the fibril drawing velocity in (14). From the lifetime τ_0 in (15), and the fibril drawing velocity (14), the craze maximum thickness is [SCH90]

$$\Delta^{cr}\left(\sigma_c\right) = 2V_{e0}\tau_{0i} \exp\left(\sigma_c / \sigma_V - \sigma_c / \sigma_t\right), \tag{16}$$

for a constant craze stress. As the critical craze thickness results from the product of the craze thickening rate (14) and the lifetime (15), we can notice that if the craze stress σ_c is rate independent, the expression of Δ^{cr} in (16) is constant, while a rate dependent craze stress results in a rate dependent Δ^{cr}, as long as σ_V and σ_t are different. For PMMA, Schirrer [SCH90] indicates that these quantities are very close to each other so that a constant critical craze thickness is derived from (16). The origin of the craze fibril breakdown is lumped into the definition of the critical craze thickness or in the lifetime τ_0 due to Schirrer [SCH90], the latter formulation including some rate dependence in Δ^{cr} through (16).

The more recent developments in the description of crazing have addressed the physical origin of the critical craze thickness Δ^{cr} and the features governing its value. Kramer and Berger [KRA90] proposed that craze thickening continues until the entanglement reduction during fibrillation is critically

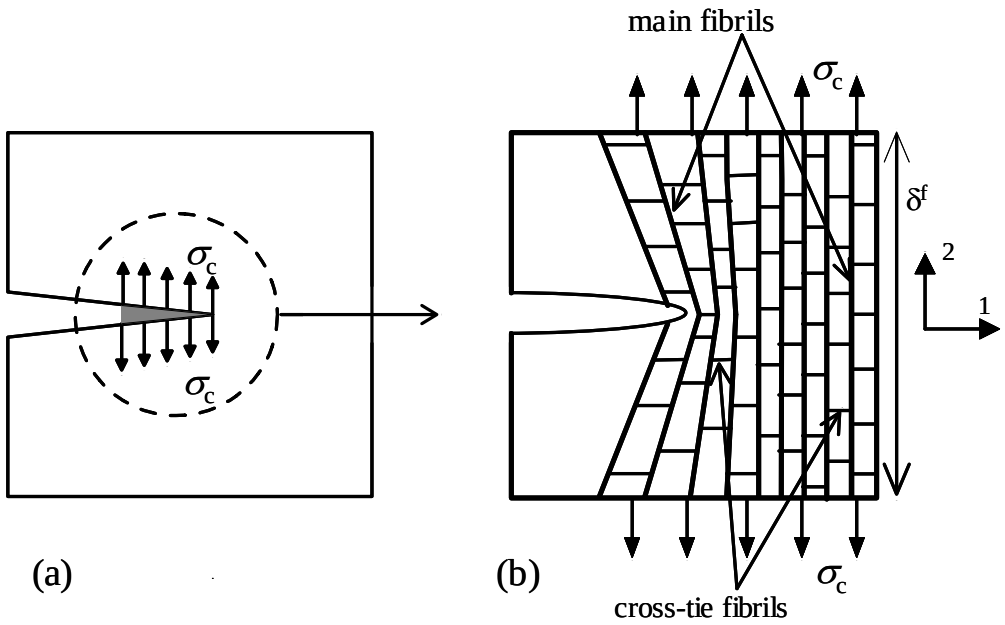

Figure 4: description of a craze (a) with a Dugdale zone, and the local analysis (b) as a long strip representing the anisotropic craze structure made of main fibrils oriented along the direction 2, connected with lateral cross-tie fibrils along 1.

enhanced by the presence of a flaw or a dust particle. Thus, the load-bearing ability locally vanishes and results in a stress concentration. The local increase of the stress triggers the breakdown of the surrounding fibrils and crack propagation within the craze strip. This process involves a statistical analysis presented in [KRA90] but this interpretation neither refers to intrinsic properties nor does it account for the influence of cross-tie fibrils.

Brown [BRO91] has demonstrated the importance of the fibrils inter-connecting the main fibrils (see Fig. 4 (b)). A two scale analysis of the craze strip is considered as presented in Fig. 4. In a Dugdale

description (Fig. 4 (a)), the craze zone is subjected to the constant stress σ_c and crack propagation occurs for the critical thickness Δ^{cr}. At the smaller scale represented in Fig. 4(b), the craze zone is regarded as a very long strip of thickness δ^f containing a crack. This strip is assumed to be subjected to the remote uniform stress σ_c in the region of the craze-crack transition. The analysis of this local problem aims in estimating the stress distribution within this craze zone and the condition for crack propagation in term of strip thickness, δ^f, and critical stress for fibril breakdown.

The craze is modeled by an elastic anisotropic medium with Young's moduli E_1 and E_2 corresponding to the stiffness of the cross-tie and the main fibrils ($E_1 << E_2$). As the strip thickens along the direction 2 (Fig. 4 (b)), the elastic energy density W is stored so that the energy release rate at failure is [BRO91]

$$g = \delta^f W = \delta^f \frac{\sigma_c^2}{2E_2}. \tag{17}$$

Brown suggested to use (17) together with the energy release rate estimated for an edge loaded elastic anisotropic specimen as [BRO91, SIH68]

$$g \approx \frac{K_I^2}{\sqrt{E_1 E_2}} = \delta^f \frac{\sigma_c^2}{2E_2} \tag{18}$$

to provide an estimate of the stress intensity factor K_I of the local problem. By considering the main fibrils approximately as cylinders of diameter D [KRA83, KRA90], the estimation of the stress at distance $D/2$ from the crack tip is $\sigma_{22}(D/2) = K_I / \sqrt{\pi D}$ so that the effective stress acting on the closest fibril to the crack tip is

$$\sigma_f = \lambda \sigma_{22}(D/2) = \lambda \sigma_c \left(\delta^f / 2\pi D\right)^{1/2} \left(E_1 / E_2\right)^{1/4}, \tag{19}$$

in which λ accounts for the isochoric transformation between primordial fibrils to mature fibrils which results in a reduction of the fibrils' cross-sectional area [KRA83, KRA90] (the fibril volume fraction is $v_f = 1/\lambda$). The condition for craze fibril breakdown corresponds to $\sigma_f^{cr} = \lambda \nu_s f_b$ in which ν_s is the surface density of entangled chains and f_b, the force required for chain breakage. From Eq. (19), the corresponding critical thickness $\delta^{f\,cr}$ for fibril breakdown is estimated from the material parameters (λ, ν_s, f_b). The connection between the two analysis comes from the thickness of the fibrillated structure δ^f, the thickness of the initial uncrazed strip δ_0 and the corresponding displacement of the craze surface Δ^c of the Dugdale problem as [KRA83, LAU79, BRO91] $\delta^f = \lambda \delta_0 = \Delta^c + \delta_0$. At the onset of craze fibrils breakdown, the latter relationship yields to $\Delta^{cr} = \delta^{f\,cr}\left(1 - v_f\right)$, in which Δ^{cr} is the

critical craze opening of the Dugdale problem and $\delta^{\mathrm{f\,cr}}$ the critical thickness of the craze strip. The energy release rate of the Dugdale problem in Fig. 4 (a) is

$$G_{\mathrm{c}} = \sigma_{\mathrm{c}} \Delta^{\mathrm{cr}} = \frac{\nu_{\mathrm{s}}^2 f_{\mathrm{b}}^2 2\pi D}{\sigma_{\mathrm{c}}} \left(\frac{E_2}{E_1} \right)^{1/2} \left(1 - \nu_{\mathrm{f}}\right), \tag{20}$$

which is distinct from the approximation used in (18) for the local problem which only aims in providing an estimate between the thickness δ^{f} and the stress on the fibril at the crack tip.

The toughness G_{c} (20) is related to material features as the surface density of entangled chains in the fibrils ν_{s} and the force for chain scission f_{b}. The value of ν_{s} depends on the amount of disentanglement induced by the fibrillation together with the 'initial' entanglement density of the bulk.

Therefore, the parameter ν_{s} provides an interpretation of the molecular dependence of the fracture toughness with molecular weight reported by Döll [DOL83]: fibrillation involves chain scission which can result in a vanishing ν_{s} for an already low molecular weight material to a constant value when stable fibrils are observed. The correlation between the toughness and the entanglement density as predicted by Brown in (20) has been observed experimentally by Wu [Wu90]. However, the relationship between the craze stress, the parameters of the craze microstructure (E_1, E_2 and D) and molecular aspects of the polymer chain (flexibility, type of the side group) still needs to be clarified and molecular dynamics calculations devoted to this investigation are emerging [ROT02, ROT03].

Following Brown's analysis on the influence of the cross-tie fibrils on craze breakdown, several improvements at a length scale between standard continuum mechanics and molecular dynamics have been reported. Hui et al. [HUI92] investigated the strip problem presented in Fig. 4 (b) with different remote conditions: the uniform craze stress σ_{c} is considered ahead of the crack tip only (x_1>0 with origin at crack tip) and $\sigma_{\mathrm{c}} = 0$ for x_1<0; and also a peak stress is used to represent a stress singularity at the crack-craze interface. Predictions of the stress level acting on the fibrils at the crack tip are provided but the general trends in term of entanglement surface density and force for chain breakage are similar to Brown's [BRO91]. Sha et al. [SHA95] use a discrete network of springs to model the fibrils of the craze strip. As two types of springs are used to represent the main or the cross-tie fibrils, estimates of the anisotropic moduli assumed by Brown [BRO91] in terms of the stiffnesses, the diameter and the volume fraction of the fibrils are presented.

More recently, Sha et al. [SHA99] pointed out the necessity to use a rate dependent drawing stress σ_{c} as reported in [DOL83, DOL90]. If only this dependence is included in Brown's model, the toughness in (20) would decrease with increasing craze stress which is in contradiction with Döll's data [DOL83, DOL90]. Therefore, Sha et al. [SHA99] incorporated a rate dependent critical craze thickness in order

to capture the evolution of the toughness with crack velocity. However, the evolution of the critical craze thickness predicted in [SHA99] decreases by a factor of five from low to fast crack velocities which is not fully consistent with experimental observations [DOL83, DOL90], thus indicating that the process of craze fibrils breakdown needs to be further clarified.

In conclusion, cross-tie fibrils are important for the interpretation of the mechanism of fibril breakdown, and can explain the influence of the chain entanglement density and chain breakage on the toughness. The analysis of craze breakdown has also pointed out the need for a rate dependent craze stress, as was already concluded from the craze thickening process. The critical craze thickness is very probably rate dependent as well, but the origin of this still has to be elucidated. Its value is approximately constant for a given temperature and molecular weight, and shows little variation (less that 20%) for PMMA for crack velocities varying over nine decades.

I.4. Cohesive surface model for crazing

In glassy polymers, crazes have typical dimensions of microns in thickness to tenths of millimeters in length so that one can generally neglect the craze thickness to the other relevant dimensions in the problem under consideration. Following the concept of a cohesive zone due to Needleman [NEE87], one can replace a craze by a cohesive surface, with constitutive properties that are based on the foregoing observations on crazing. Tijssens et al. [TIJ00] design a cohesive surface which mimics the three stages of initiation, thickening and breakdown. The methodology is illustrated in Fig. 5 with the (a) assumed craze structure, (b) the idealization of the craze process with the transition from initiation to craze thickening and ultimately the craze fibril breakdown and related crack nucleation, (c) the description in terms of cohesive elements within a finite element framework. When crazing has not yet initiated, the cohesive surfaces are adjacent and there is no discontinuity across the plane under consideration. Once crazing has nucleated, craze thickening develops and the separation between the two cohesive surfaces results in an opening Δ_n. The traction vector σ_n is energetically conjugate to Δ_n and the mechanisms underlying this process are lumped into a traction-opening law to be defined in the sequel. Once craze fibrils break down, a crack nucleates locally and this is accounted for by prescribing a vanishing traction on the corresponding location of the cohesive surface.

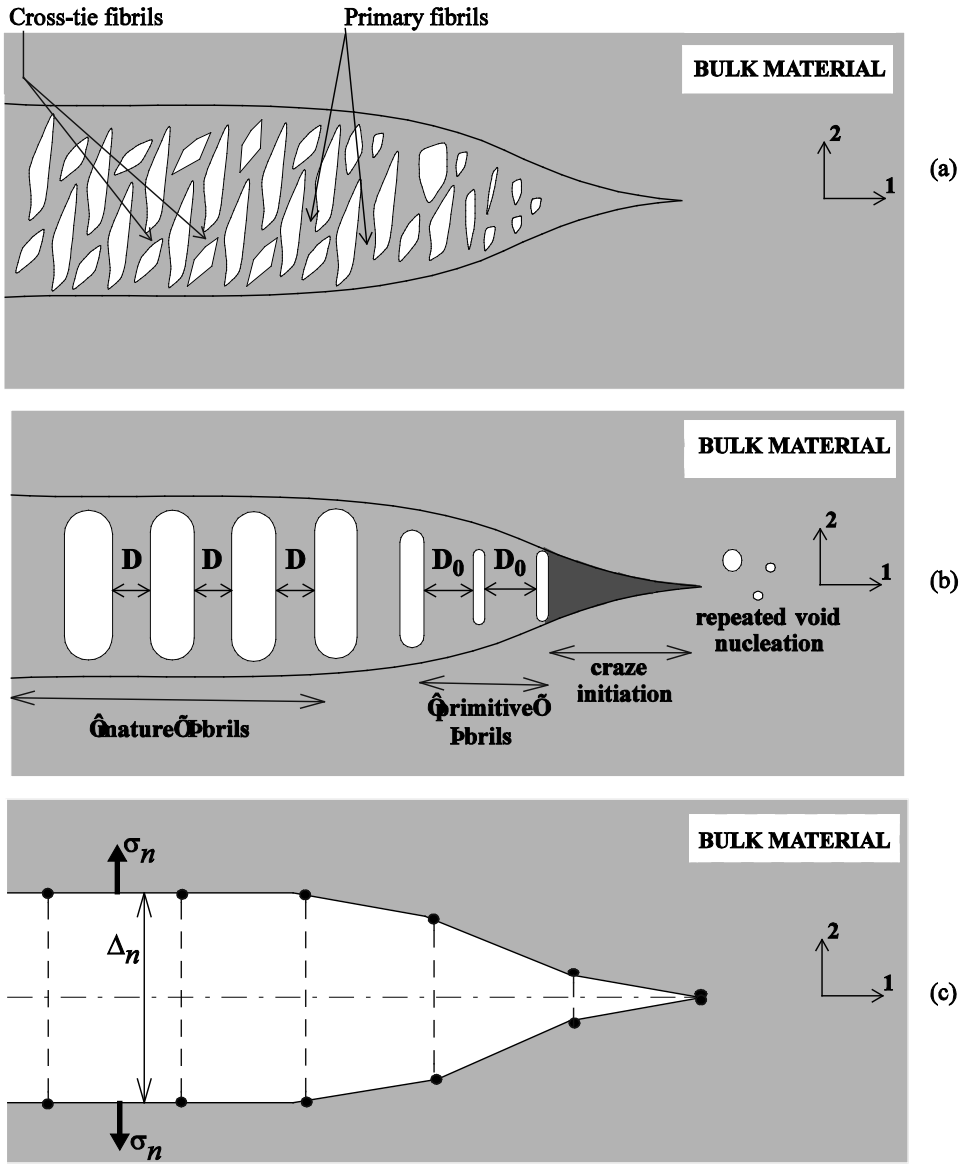

Figure 5: (a) schematic description of the craze structure, (b) idealization of the craze process according to Kramer and Berger [KRA90] for the craze thickening after initiation, (c) representation of crazes by discrete cohesive surfaces.

I.4.1. **Craze initiation**

Initiation is assumed to occur when a critical stress state is attained, according to one of the criteria reported in the literature as discussed in a preceding section. We choose to use the criterion formulated by Sternstein and Ongchin [STE69] to illustrate how it can be incorporated into the cohesive surface framework, which is flexible enough to account for another definition. The criterion is presented in (11) for a plane stress condition, with σ_1 the major principal stress and the first invariant, or $3\sigma_m$.

Within the cohesive surface description as in Fig. 5 (c), we assume that the direction of the major principal stress corresponds to the normal direction so that $\sigma_1 \equiv \sigma_n$ in (11).

By assuming plane strain conditions as relevant for crack studies and taking the hydrostatic stress as $\sigma_m = 1/3(1+\nu)(\sigma_1+\sigma_2) \approx (\sigma_1+\sigma_2)/2$, the criterion can be reformulated as [EST00]

$$\sigma_n \geq \sigma_m - \frac{A^0}{2} + \frac{B^0}{6\sigma_m} = \sigma_n^{cr}(\sigma_m). \tag{21}$$

Since σ_1 is the major principal stress, we have $\sigma_n = \sigma_1 \geq \sigma_m = (\sigma_1+\sigma_2)/2$ and the side condition that the normal stress has to exceed the hydrostatic stress for craze initiation is satisfied. Equation (21) defines a critical normal stress which appears to be hydrostatic stress dependent. As long as $\sigma_n < \sigma_n^{cr}(\sigma_m)$, crazing does not occur and when σ_n reaches $\sigma_n^{cr}(\sigma_m)$, crazing initiates. Once initiated, the craze thickens and the condition (21) is no longer relevant.

I.4.2. **Craze thickening**

As discussed in Sec.I.3.2, once a mature fibrils is created, further thickening occurs by a viscoplastic drawing mechanism which involves intense plastic deformation at the craze-bulk interface [KRA90]. Instead of using a non Newtonian formulation as in [KRA90] or a formulation based on Eyring's model [SCH90], but on the basis of a preliminary study of the process [VAN97], the craze thickening is described with a similar expression as the viscoplastic strain rate for the bulk in (3) as [TIJ00]

$$\dot{\Delta}_n^c = \dot{\Delta}_0 \exp\left[\frac{-A^c\sigma^c}{T}\left(1-\frac{\sigma_n}{\sigma^c}\right)\right], \tag{22}$$

in which $\dot{\Delta}_n^c$ is the craze thickening rate and $\dot{\Delta}_0$, A^c, σ^c are material parameters; $\dot{\Delta}_0$ characterizes the intrinsic mobility during the thickening process, A^c controls the temperature dependence and σ^c is the athermal stress for craze thickening. The above expression is phenomenological and will be shown to be able to capture the main features of glassy polymer fracture. Of course, a physically based formulation would be preferable and could be incorporated when available.

I.4.3. **Craze breakdown**

Craze breakdown is experimentally characterized by a critical craze thickness Δ^{cr} which is primary dependent (Eq. (20)) on the craze stress σ_c, the force for chain scission f_b and the entangled chain density along the craze surface ν_s. The craze stress σ_c is assumed to be rate and temperature

dependent. As the entanglement density before fibrillation is temperature dependent (Eq. (7)), the parameter ν_s probably reveals temperature dependence. Experimental observations [DOL83, DOL 90] indicate that the temperature can significantly influence Δ^{cr} but the rate dependence can be neglected as a first approximation.

Therefore, the condition for craze breakdown is incorporated in the cohesive zone description by adopting a critical thickness Δ^{cr} that is just material dependent. We will briefly explore the influence of a temperature-dependent critical thickness in some non-isothermal calculations by letting the value of Δ^{cr} increase by a factor of two from room temperature to T_g.

Such a phenomenological definition of the critical craze thickness Δ^{cr} hides much of the underlying physics. Further insight is expected to reveal how this parameter changes with loading rate as well as on the temperature dependence, which could then be incorporated in the present framework.

I.4.4. **Traction versus thickening law for the cohesive surfaces**

The three stages of the crazing process discussed in the foregoing subsections, are combined by the traction-opening law

$$\dot{\sigma}_n = k_n \left(\dot{\Delta}_n - \dot{\Delta}_n^c \right) = k_n \dot{\Delta}_n^e , \tag{23}$$

with $\dot{\Delta}_n$ the normal opening rate of the cohesive surface, $\dot{\Delta}_n^c$ the thickening rate of the craze according to (22) and k_n an elastic stiffness. The traction-opening law in (23) is used for the three stages of the crazing process. Prior to craze initiation, $\dot{\Delta}_n^c$ is not relevant and (23) reduces to $\dot{\sigma}_n = k_n \dot{\Delta}_n$ in which the stiffness k_n has to be 'infinitely' large to ensure that the elastic opening remains small and does not significantly affect the continuity of the fields.

When craze widening takes place, k_n represents the elastic stiffness of the fibrillated craze structure. From experimental observations of crazes in thin films, Kramer and Berger [KRA90] suggest that the early stages of fibrillation consists of the transformation of a primitive fibril into a mature fibril at a constant volume. Further fibrillation is due to the drawing process. By considering the primitive fibrils at craze initiation (Fig 5 (b)) as struts of diameter D_0 and height h_0, their transformation into a mature fibril of diameter D with height h corresponds to $h=\lambda h_0$ and $D=D_0/\lambda^{1/2}$, λ being the extension ratio. By assuming that $\Delta_n=h_0$ at craze initiation, the stiffness of the primitive fibrils is [EST00]

$$k_n^0 = \frac{\sigma_n^{cr}}{h_0} . \tag{24}$$

During this transformation from primitive to mature fibril, the force distribution acting on the craze-bulk interface remains constant so that $\sigma_n^{f0} = F / S_0$ and $\sigma_n^{f} = F / S$ in which σ_n^{f0} and σ_n^{f} represent the stress acting on the primitive and the elongated fibrils, respectively. By assuming that the elastic modulus of the fibrils, E_f, remains constant, we obtain $\sigma_n^{f0} = E_f \Delta_n / h_0$ and $\sigma_n^{f} = E_f \Delta_n / h$ from which we define the stiffness of the primitive fibrils at craze initiation and that of the mature fibril as

$$k_n^0 = \frac{E_f}{h_0} = \frac{\sigma_n^{cr}}{h_0} \text{ and } k_n = \frac{k_n^0}{\lambda}, \tag{25}$$

with $\lambda = h/h_0$. Once the 'mature' fibrils have formed, the craze consists of highly stretched coils. The overall instantaneous elastic stiffness of the craze, k_n, is therefore assumed to arise primarily from the freshly drawn-in material into the fibrils. The stiffness is thus assumed to remain constant and equal to the limiting value $k_n = k_n^0 / \lambda_N$ according to (25) in which $\lambda_N = \sqrt{N}$ is the maximum stretch of the polymer coil.

Prior to craze initiation, $\sigma_n < \sigma_n^{cr}(\sigma_m)$ in (21) and the stiffness has to be 'infinitely' large to ensure that 'no' separation occurs across the cohesive surface. We propose to use

$$k_n^{\infty} = \frac{\sigma_n^{cr}(\sigma_m)}{h_0} \tag{26}$$

in the traction-opening law (23) for numerical convenience, in which σ_m is the instantaneous hydrostatic stress. The stiffness k_n^{∞} in (26) becomes infinite when the mean stress vanishes and a limiting value is used when this happens, which is adjusted to about ten times the stiffness at craze initiation (24). When crazing initiates, the stiffness evaluated from (26) and that from (24) are identical with k_n^{∞} prior to initiation decreasing gradually to k_n^0.

We illustrate in Fig. 6 the full traction response to a constant widening rate $\dot{\Delta}_n$ derived from (23). The three regimes of the craze process can be readily distinguished:

1. during the loading, the normal stress σ_n increases but crazing has not initiated yet so that negligible thickening is observed,
2. after a short transition following craze initiation, the craze thickens and results in an opening Δ_n of the cohesive surface at approximately constant normal stress,
3. when the craze thickness attains the critical value Δ_n^{cr}, craze fibrils break down and a microcrack nucleates with a related vanishing normal stress.

During craze thickening, two trajectories are distinguished in Fig. 6, depending on the prescribed widening rate $\dot{\Delta}_n$ of the cohesive surfaces. After initiation, if the cohesive surface widening rate corresponds to $\dot{\Delta}_n > \dot{\Delta}_n^c$, the hardening-like response (2a) is observed while a softening-like response (2b) corresponds to $\dot{\Delta}_n < \dot{\Delta}_n^c$. The plateau is attained when the two opening rates are equal ($\dot{\Delta}_n = \dot{\Delta}_n^c$). The widening rate of the cohesive surfaces $\dot{\Delta}_n$ is governed by the prescribed loading rate while the craze thickening rate is determined by the craze

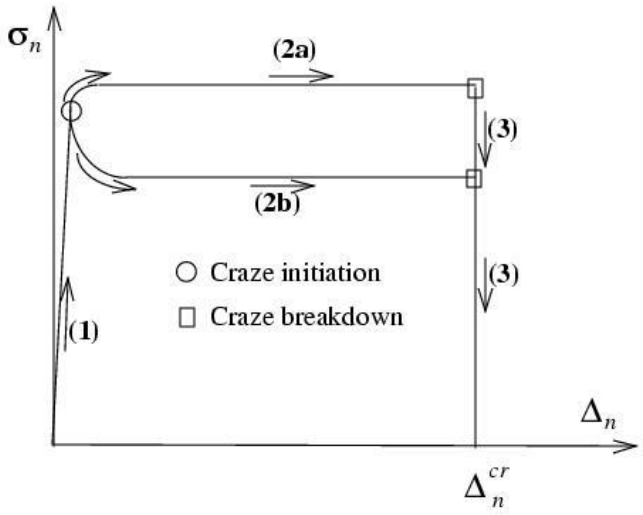

Figure 6: Schematic representation of the cohesive surface traction-opening law: (1) no crazing, (2) craze widening with (2a) hardening like response or (2b) softening like response depending on to the prescribed opening rate, (3) craze breakdown at $\Delta_n=\Delta_n^{cr}$.

fibrillation process (22). The evolution of the traction-opening law as (2a) or (2b) is controlled by the competition between these two. As the area under the traction-opening curve corresponds to the energy dissipated by the crazing process, it also corresponds to the energy release rate for crack propagation. With this formulation, the rate dependence of the energy release rate arises from the rate dependence of the craze thickening process.

The foregoing formulation for crazing focuses on the description along the normal direction. The formulation of Tijssens et al. [TIJ00, TIJ00b] accounts also for a tangential component in the cohesive properties with a tangential traction σ_t and a tangential displacement Δ_t being related by

$$\dot{\Delta}_t^c = \dot{\Gamma}_0 \left\{ \exp\left[-\frac{A^c \tau^c}{T}\left(1-\frac{\sigma_t}{\tau^c}\right)\right] - \exp\left[-\frac{A^c \tau^c}{T}\left(1+\frac{\sigma_t}{\tau^c}\right)\right]\right\}, \qquad (27)$$

during drawing ($\dot{\Gamma}_0$ and τ^c are material parameters). From a numerical point of view, an initially large tangential stiffness is necessary to prevent tangential sliding along the cohesive surfaces. The aim in [TIJ00, TIJ00b] is to use this phenomenological description of the tangential deformation of the

cohesive surface to investigate how a variation in the tangential load-carrying ability of the craze fibrils could affect crack propagation and related resistance curve. This is shown to be of minor importance in [TIJ00b] but the framework is flexible enough to incorporate such aspect when appropriate description is to be available.

I.4.5. **Alternative descriptions**

Beside the cohesive surface framework presented here, other approaches to model crazing within a finite element formulation have been reported recently. Boyce et al. [SOC01] define a thin craze element which accounts for craze initiation and craze thickening. Craze breakdown is not incorporated in [SOC01] since it was not of concern in the problem under investigation. In many aspects, this formulation resembles a cohesive surface development, but a standard continuum description is adopted which results in a stress-strain relation instead of a traction-opening law. Before crazing initiates in the craze (continuum) element, the related thin layer has the properties of the bulk. When the condition for craze initiation is fulfilled within the layer, the thin bulk transforms into a primordial craze. The description of craze thickening uses also a rate dependent formulation for the normal and the tangential components of the craze thickening but the analysis is restricted to the analysis of stable crazes and craze breakdown is not considered.

Gearing and Anand [GEA04] have also used a classical continuum approach to describe crazing. A viscoplastic stress-strain law is derived from an analysis of the material response in the presence of diffuse crazing. This can be motivated as long as multiple crazing is observed but becomes questionable when the loading conditions result in the development of a single craze as in mode I crack growth.

The cohesive surface description presented here has some similarities to the thermal decohesion model of Leevers [LEE95] which is based on a modified strip model to account for thermal effects, but a constant craze stress is assumed. Leevers focuses on dynamic fracture. The thermal decohesion model assumes that heat generated during the widening of the strip diffuses into the surrounding bulk and that decohesion happens when the melt temperature is reached over a critical length. This critical length is identified as the molecular chain contour.

I.5. 3D effects in mechanical response of glassy polymers

In glassy polymers, shear yielding and related strain localization with the development of controlled necking or notch/crack tip plasticity have been first investigated in 2D plane strain conditions [Wu95, MEL03, GEA04]. The extension to 3D calculations has emerged during the last ten years, which somehow revisit the 2D studies [TOM97, LIN08, LIN08b, KWE13]. For instance in the analysis of necking, the 2D analysis of Wu and Van der Giessen [Wu95] (see also for instance Melick et al. [MEL03]) show the importance of strain softening to trigger a shear band, its width being limited by the progressive hardening of the material at continued deformation. Strain hardening also promotes the propagation of the shear band's front with controlled necking by strain softening of the neighboring material. 3D studies of necking have emerged recently [LIN08, LIN08b, KWE13]. Lindgreen et al. [LIN08, LIN08b] have focused on the onset and development of necking in a tube subjected to internal pressure. The analysis of this specific problem is conducted in a 3D analysis. Kweon and Benzerga [KWE13] investigated the influence of the specimen geometry and more precisely its thickness on the development of shear bands. They point out that 2D calculations may overestimate the influence of the material's strain softening on localization. Softening could not be a necessary condition for observation of necking in 3D calculations. The influence of the specimen geometry on the patterning of the shear bands is reported. This work addresses specifically the influence of the sample thickness of the mechanical response, which is also examined in our thesis.

The same progression from 2D plane strain to full 3D calculations is observed in the investigation of notch/crack tip plasticity. This has been explored initially by Nimmer and Woods [NIM92] who show that the plastic zone observed around the notch of ductile polymer subjected to mode I is similar to that predicted with Hill's slip line. They consider a simplistic constitutive law consisting in an elastic perfectly plastic material with account for a pressure sensitive yield stress. The material response did not account for softening nor hardening of the material. However, it was found that a plastic zone similar to that observed in glassy polymer [ISH77, NIM92] can be predicted with a fairly good prediction.

With a realistic description of glassy polymers constitutive law that incorporates shear yielding with strain softening and progressive hardening at continued deformation, Lai and Van der Giessen [LAI 95] present a detailed investigation of the crack tip fields and related plastic zone. They observed a characteristic plastic zone similar to Hill's slip lines too but the pattern of the shear bands is shown clearly dependent on the amount of softening and aptitude to hardening. They point out that in the absence of softening, a kidney shape plastic zone is observed, similarly to that observed in metals. 3D calculations by accounting for a notched specimen are reported later [GEA04, TVE08]. The motivation for Gearing and Anand to use 3D calculations was to compare their fracture predictions in 3-points bending in a notched polycarbonate to experimental data. Tvergaard and Needleman

investigated the transient dynamic response of glassy polymers subjected to the IZOD test, with accounting for the specific constitutive law for glassy polymers. They explored the influence of the specimen thickness on the development of the plasticity during the impact load. From the observation of the shape of the plastic zone, a transition from plane strain to intermediate conditions combining plane strain and plane stress conditions are reported when the thickness decreases from a value larger than 6 mm to 3mm respectively, the notch tip radius being 0.25mm. Tvergaard and Needleman's contribution is thought to shed some light on the appropriate specimen size to characterise the material's resistance to the IZOD test and initiate a work comparable to that developed for the interpretation of the Charpy test for metals.

From the experimental point of view, 3D effects have been investigated by Parvin and Williams [PAR75] who analysed the toughness variation of polycarbonate samples subjected to mode I loads with their thickness. They observed a progressive reduction of the toughness with increasing thickness up to a stable value. In order to capture this variation, they proposed an empirical relationship which combines the value of the toughness for thin samples (though to be under plane stress) with that of thick samples (dominantly under plane strain) to capture their experimental data.

Conclusion

The review of the bibliography shows that the analysis of the mechanical and fracture response of glassy polymers has now reached a stage as mature in metals from the continuum point of view: realistic constitutive laws are available [BOY88, Wu96, ANA03], physically based descriptions of fracture by crazing [TIJ00, EST00, SAA06] are available as well. While most of the pioneering investigations were restricted to 2D plane strain conditions, 3D calculations are now tractable and studies have emerged for the last 10 years [GEA04, GEA04b, LIN08, LIN08b, TVE08, KWE13]. In the present thesis work, we account for a constitutive law for the glassy polymer response and investigate first the notch/crack tip fields with the objective to assess when plane stress or plane strain conditions prevail and how to characterize this. This is the purpose of chapter 2. In chapter 3, we investigate 3D effects on polymer fracture with a description of the failure process with a simplified cohesive model. Actually, in ductile polymer, the bulk viscoplastic response governs the local kinematic fields and the use of a rate dependent cohesive description as in [TIJ00, EST00] is not mandatory. In all cases, the predictions reported in the present study can be compared to available experimental data found in the literature (for instance [PAR75]). The chapter 4 is a conclusion with a gathering of the main results and suggestions for future work.

References for Chapter I

[ABA10] Abaqus, version 6.10-2, simulia, Dassault systems.

[AGA91] Agassant JF, Avenas P, Sergent JPh, Carreau PJ (1991) Polymer processing: principles and modelling, Hanser Gardener Pubns, Munich

[ANA03] L. Anand, M. E. Gurtin, 2003, IJSS, A theory of amorphous solids undergoing large deformations, with application to polymeric glasses 40: 1465-1487

[ARG73] Argon AS (1973) Phil Mag 28:839

[ARG77] Argon AS, Hannoosh JG (1977) Phil Mag 36:1195

[ARR93] Arruda EM, Boyce MC (1993) J Mech Phys Sol 41:389

[ARR95] Arruda EM, Boyce MC, Jayachandran R (1995) Mech Mat 19:193

[BAS02] Basu S, Van der Giessen E (2002) Int J Plast 18:1395

[BJE03] Bjerke TW, Li Z, Lambros J (2003) J Mech Phys Sol 51:1147

[BOY88] Boyce MC, Parks DM, Argon AS (1988) Mech Mat 7:15

[BRO73] Brown HR, Ward IM (1973) Polymer 14:469

[BRO81] Brown HR, Kramer EJ (1981) J. Macromol. Sci.-Phys B19:487

[BRO91] Brown HR (1991) Macromolecules 24:2752

[DOL73] Döll W (1973) Engng Fract Mech 5:229

[DOL79] Döll W, Schinker MG, Könczöl L (1979) Int J. Fract 15:R145

[DOL83] Döll W (1983) Adv Polym Sci 52-53:106

[DOL90] Döll W, Könczöl L (1990) Adv Polym Sci 91-92:138

[DUG60] Dugdale DS (1960) J Mech Phys Sol 8:100

[EST00] Estevez R, Tijssens MGA, Van der Giessen E (2000) J Mech Phys Sol 48:2585

[EST04] Estevez R, Basu S, Van der Giessen E (2004) Int J Fract in preparation

[FUL75] Fuller KNG , Fox PG , Field JE (1975) Proc R Soc Lond A341:537

[GEA04] Gearing B.P. and Anand L., 2004, IJSS, Notch-sensitive fracture of polycarbonate 41:827-845

[GEA04b] Gearing B.P. and Anand L., 2004, IJSS, On modeling the deformation and fracture response of glassy polymers due to shear-yielding and crazing, 41:3125-3150

[HAW68] Haward RN, Thackray G (1968) Proc R Soc Lond A302:453

[HUI92] Hui CY, Ruina A, Creton C, Kramer EJ (1992) Macromolecules 25:3948

[ISH77] Ishikawa M, Narisawa I (1977) J Polym Sci 15:1791

[ISH83] Ishikawa M , Narisawa I (1983) J Mat Sci 2826

[KAM73] Kambour RP (1973) J Polymer Sci 7:1

[KAU83] Crazing in Polymers (1983) Kausch HH ed, Advances in Polymer Science, 52-53, Heidelberg-Berlin: Springer

[KAU87] Kausch HH (1987) Polymer Fracture, 2nd edn., Springer Berlin Heidelberg New York

[KAU90] Crazing in Polymers Vol. 2(1990) Kausch HH ed, Advances in Polymer Science, 91-92, Heidelberg-Berlin: Springer

[KRA83] Kramer EJ (1983) Adv Polym Sci 52-53:1

[KRA90] Kramer EJ, Berger LL (1990) Adv Polym Sci 91-92:1

[LAU79] Lauterwasser BD, Kramer EJ (1979) Phil Mag A 39:469

[LEE95] Leevers PS (1995) Int J Fract 73:109

[LIN08] Lindgreen B. , Tvergaard V. , Needleman A., 2008, Dynamic neck development in a polymer tube under internal pressure loading, IJSS, 45:580-592

[LIN08b] Lindgreen B. , Tvergaard V. , Needleman A., 2008, Bulge formation and necking in a polymer tube under dynamic expansion, Model. Simul. Mat. Sci. Engng., 16 (2008) 085003 (14pp)

[MAR74] Marshall GP, Coutts LH, Williams JG (1974) J Mat Sci 9:1409

[MEL03] Melick, H.G.H.V., Govaert, L.E., Meijer, H.E.H., 2003. Localisation phenomena in glassy polymers: influence of thermal and mechanical history. Polymer 44,3579-3591.

[MOR77] Morgan GP, Ward IM (1977) Polymer 18:87

[NEE87] Needleman A (1987) J Appl Mech 54:525

[NIM 92] Nimmer, R.P., Woods, J.T., 1992. An investigation of brittle failure in ductile notch-sensitive thermoplastics. Polymer Engineering and Science 32, 1126–1137.

[OXB73] Oxborough RJ, Bowden PB (1973) Phil Mag 28:547

[PAR75] Parvin M., Williams J.G. Ductile-Brittle transitions in polycarbonate, Int J Fracture. 1975, 11:963-972

[RAH72] Raha S, Bowden PB (1972) Polymer 13:174

[PIT79] Pitman GL, Ward IM (1979) Polymer 20:895

[RIT96] Rittel D, Maigre H. An investigation of dynamic crack initiation in PMMA. Mech Mat. 1996, 23:229

[RIT98] Rittel D. Experimental investigation of transient thermoplastic effects in dynamic fracture. Int. J. Sol Struct. 1998, 35:2959

[ROT02] Rottler J, Robins MO. Jamming under tension in polymer crazes. Phys Rev Let. 2002, 89:1955

[ROT03] Rottler J, Robins MO. Shear yielding of amorphous glassy solids: Effect of temperature and strain rate. Phys Rev E. 2003, 68:118

[SCH90] Schirrer R. Adv Polym Sci. 1990, 91-92:215

[SHA95] Sha Y, Hui CY, Ruina A, Kramer EJ. Macromolecules. 1995, 28:2450

[SIH68] Sih GC Liebowitz H. In: Liebowitz H (ed) Fracture. 1968, Academic Press, San Diego, 2:67

[SHA99] Sha Y, Hui CY, Kramer EJ. J Mat Sci. 1999, 34:3695

[SOC01] Socrate S, Boyce MC, Lazzeri A. Mech Mat. 2001, 33:155

[STE69] Sternstein SS, Ongchin L. Polym Preprints. 1969, 10:1117

[STE73] Sternstein SS, Myers FA. J Macromol Sci -Phys B. 1973, 8:539

[TIJ00] Tijssens MGA, Van der Giessen E, Sluys LJ. Modeling of crazing using a cohesive surface methodology. Mech Mat. 2000, 32:19.

[TIJ00b] Tijssens MGA, Van der Giessen E, Sluys LJ. Int J Sol Struct. 2000, 37:7307

[TIJ02] Tijssens MGA, Van der Giessen E. A possible mechanism for cross-tie fibril generation in crazing of amorphous polymers. Polymer. 2002, 43:831

[TVE08] Tvergaard V., Needleman A. An analysis of thickness effects in the Izod test. IJSS. 2008, 45:3951–3966

[VAN90] Van Krevelen DW. Properties of Polymers, 3rd edn., Elsevier. 1990.

[VAN97] Van der Giessen E. Eur J Mech. 1997, 16:87.

[VAN97] Van der Giessen E, Lai J. Proc. 10th Int. Conf. on Deformation, Yield and Fracture of Polymers. 1997, Cambridge 35.

[WAD92] Wada H. Determination of dynamic fracture toughness for PMMA. Engng Fract Mech. 1992, 41:821.

[WAD96] Wada H, Seika M, Kennedy TC, Calder CA, Murase K. Investigation of loading rate and plate thickness effects on dynamic fracture toughness of PMMA. Engng Fract Mech. 1996, 54:805-812.

[WEI78] Weidman GW, Döll W. Int J Fract. 1978, 14:R189.

[WIL81] Williams JG, Hodgkinson JM. Crack-blunting mechanisms in impact tests on polymers. Proc R Soc Lond A. 1981, 375:231.

[WIL84] Williams JG. Fracture Mechanics of Polymers. 1984, Ellis Horwood, New York.

[Wu90] Wu.S. Polym Engng Sci. 1990, 30:753.

[Wu93] Wu, P.D., Van der Giessen, E. On improved network models for rubber elasticity and their applications to orientation hardening in glassypolymers. J. Mech. Phys.Solids.1993, 41:427.

[Wu95] Wu, P.D., Van der Giessen, E. On neck propagation in amorphous glassy polymers under plane strain tension. Int. J. Plast. 1995, 11:211-235.

[Wu96] Wu, P.D., Van der Giessen, E. Computational aspects of localized deformations in amorphous glassy polymers. Eur. J. Mech. A. 1996, 15:799-823.

List of symbols

notations

$\otimes$	tensor product
$\sqcup$	scalar product
$()'$	deviatoric part of a second-order tensor
tr	trace of a tensor

Tensors and vectors

$\boldsymbol{e}_i$	basis unit vector
$\boldsymbol{I}$	second-order unit tensor
$\boldsymbol{D}$	deformation rate tensor
$\boldsymbol{D}^{\mathrm{e}}$	elastic part of the deformation tensor
$\boldsymbol{D}^{\mathrm{p}}$	plastic part of the deformation tensor
$\boldsymbol{\sigma}$	Cauchy stress tensor
$\boldsymbol{b}$	back stress tensor
$\bar{\boldsymbol{\sigma}}$	effective stress tensor
$\boldsymbol{\pi}, \boldsymbol{T}$	second Piola-Kirchhoff stress tensor and related traction vector
$\boldsymbol{\eta}, \boldsymbol{u}$	Lagrangian strain tensor and displacement vector
$\overset{\nabla}{\boldsymbol{\sigma}}$	Jaumann rate of the Cauchy stress tensor
$\boldsymbol{C}_{\mathrm{e}}$	fourth-order isotropic elastic modulus tensor

for the description of the bulk response

T_g	glass transition temperature
E	Young modulus
K	bulk modulus
ν	Poisson's coefficient
α_c	coefficient of cubic thermal expansion
$\dot{\gamma}^p$	equivalent shear strain rate
τ	equivalent shear stress
p	hydrostatic pressure
α	pressure sensitivity coefficient
s_0	initial shear strength
s_{ss}	steady state shear strength
h	scalar parameter controlling the rate of softening
$\dot{\gamma}_0$	pre-exponential shear strain rate factor
A	parameter for the temperature dependence of the shear strain rate
$\dot{D}$	energy dissipation rate per unit volume
λ_α	principal plastic stretches $(\alpha = 1,\ldots,3)$
$\bar{\lambda}$	largest plastic stretch
$\boldsymbol{e}_\alpha^p$	principal directions of the plastic stretch
$b_\alpha^{3\text{-ch}}$, $b_\alpha^{8\text{-ch}}$	three chains and eight chains description for the estimate of the back stress tensor $\boldsymbol{b}$
λ_N	maximum stretch of the polymer coil
N	number of segments between entanglements
n	volume density of entanglements

k_B	Boltzmann constant
C^R	shear modulus of the plastically activated entangled network
R	gas constant
E_a	entanglements dissociation energy
η	viscosity in the non-Newtonian response above T_g
m	exponent of the non-Newtonian response above T_g
k	thermal conductivity
ρ	mass density
c_v	isochoric specific heat

for the description of crazing

σ_y	tensile yield stress
σ_m	mean stress
I_1	first stress invariant
$\sigma_1, \sigma_2, \sigma_3$	principal stresses
σ_{max} , σ_{min}	maximum and minimum principal stresses
σ_b	stress bias
A^0, B^0	parameters in the craze initiation criterion of Sternstein et al. [24]
X', Y'	parameters in the craze initiation criterion of Oxborough and Bowden [26]
Δ^{cr}	critical craze thickness
Λ_c	craze length

D_0, D	primitive and mature fibril diameter
V_e	craze thickening rate
τ_0	fibril lifetime
σ_c	craze stress in the Dugdale description (see Figs. 3-4)
f_b	force for chain breakage
ν_s	surface density of entangled chains
E_1, E_2	Young moduli to represent the anisotropic craze fibrils structure

for the modeling of crazing with cohesive surfaces

σ_n	traction vector normal to the cohesive surface
σ_n^{cr}	critical traction for craze initiation
σ_t	traction vector tangential to the cohesive surface
$\dot{\Delta}_n^c$	craze thickening rate along the direction normal to the craze plane
$\dot{\Delta}_0, A^c, \sigma^c$	material parameters for the normal craze thickening rate: pre-exponential thickening rate, temperature dependence, athermal normal stress
$\dot{\Delta}_t^c$	tangential craze thickening rate
$\dot{\Gamma}_0, \tau^c$	material parameters for the tangential craze thickening rate: pre-exponential thickening rate, athermal shear stress
k_n	stiffness of the cohesive surface
h_0	thickness of the craze at the onset of craze initiation
$\boldsymbol{q}$	heat flux through the cohesive surfaces

G_c	energy release rate

K_I mode I stress intensity factor

$\dot{K}_I$ rate of the mode I stress intensity factor

material features

M_w weight average molecular weight

PMMA Polymethylmethacrylate

PC Polycarbonate

SAN Styrene acrylonitrile

K Kelvin

CRACK-TIP PLASTICITY IN GLASSY POLYMERS

In this chapter, a detailed analysis of the notch tip fields for ductile glassy polymers subjected to Single Egde Notch Tension tests is presented. Three materials with a polymer like mechanical response are considered, with a different magnitude in the strain softening, a fourth one typical of metal is also investigated for a comparison purpose. 2D plane strain calculations are reported first prior to full 3D simulations. The influence of the specimen's thickness is investigated as well as that of the magnitude of the strain softening upon yielding on the magnitude of the strain localization. A different plastic zone from the surface where plane stress conditions prevail toward the center is observed. Not only the extent of the plasticity is changed but also the ability to trigger shear bands and related localized plasticity. A critical thickness over notch tip radius ratio is found to ensure plane strain dominated conditions. This is helpful in defining the size requirements for fracture tests for this class of materials. The analysis of the distribution of the maximum mean stress with thickness confirms this observation.

Table of contents

II. crack-tip plasticity in glassy polymers 1
Table of contents 2
II.1. Introduction 3
II.2. Constitutive law for glassy polymers 4
II.2.1. Modelling background 4
II.2.2. Materials under considerations 7
II.3. Problem formulation 9
II.3.1. Description of geometry and mesh discretization 9
II.4. 2D and 3D Crack tip plasticity investigations 12
II.4.1. Qualitative description of a SENT with blunted notch experiment 12
II.4.2. 2D plane strain crack tip plasticity 13
II.4.3. 3D crack tip plasticity : reference material A 18
II.4.4. Influence of the strain softening on 3D crack tip plasticity 25
II.4.5. Influence of the notch radius on 3D crack tip plasticity 28
II.5. Discussion 33
II.6. Conclusion 35
References For Chapter II 37

II.1. Introduction

The objective of this chapter is to gain insight for the estimation on whether plane stress and/or plane strain conditions are dominant or mixed in the characterization of glassy polymer fracture, under quasi-static conditions. A numerical study is carried out with implementation of Boyce et al. constitutive law [BOY88] in the version modified by Wu and Van der Giessen [Wu96] through a UMAT routine in Abaqus [ABA10]. The Single Edge Notched Tension (SENT) configuration is considered with given dimension regarding the length, width and crack length. The thickness is varied and three notch tip radii are considered. A configuration with a notch specimen is preferred to that with a natural crack as experimentally machining a natural crack is difficult in ductile polymers while preparing a blunted one is tractable.

We investigate the shape of the plastic zone for various thicknesses and use the ratio between the thickness t and the notch radius R to distinguish the samples geometry. 2D calculations are first carried out under the assumption of plane strain conditions. The specific crack tip plastic zones in 2D plain strain cases are used as reference for the analysis of 3D calculations, in which the plastic zones at the surface and in the center of the specimen are systematically compared. The distribution of the cumulated plastic strain and its strain rate serve to identify plane stress, mixed plane stress – plane strain and plane strain dominant conditions. These observations are thought to provide some guidance in the definition of an experimental configuration that ensures plane strain dominant conditions in the case of a ductile polymer, i.e. when fracture is preceded by large plastic deformations. A critical ratio between the thickness t to the notch tip radius R is observed that separates plane stress to plane strain dominant conditions. This is confirmed by observing the variation of the maximum mean stress during the loading for all samples.

II.2. Constitutive law for glassy polymers

II.2.1. **Modelling background**

In the absence of crazing, glassy polymers can undergo a deformation up to 100% with an intriguing constitutive law with softening upon yielding followed by hardening. In an analysis of the crack tip plasticity under a mode I loading, Lai and Van der Giessen [LAI97] have shown that the observed softening is intrinsic to the material response and is not due to a structure or geometrical effect. Their prediction of the shape of the plastic zone and trajectories of the shear bands is in good agreement with reported observations of Ishikawa et al. [ISH77]. The constitutive law used to model the large strain plastic behaviour is based on original ideas due to Boyce et al. [BOY88] but with some modifications introduced later by Wu and Van der Giessen [WU93] for the hardening part. We present the governing equations to point out the parameters to be identified. The constitutive equations presented here have been implemented in a UMAT subroutine in Abaqus [ABA10] following the [WU96] for the computational aspects.

The mechanics of fully three-dimensional large strain deformation involves the deformation gradient tensor $\boldsymbol{F}$, which maps a material point of the reference configuration into the current configuration. The deformation gradient is multiplicatively decomposed as $\boldsymbol{F} = \boldsymbol{F}^{\boldsymbol{e}}\boldsymbol{F}^{\boldsymbol{p}}$, with $\boldsymbol{F}^{\boldsymbol{P}}$ a deformation from the initial to an intermediate, “relaxed” or “natural” configuration, followed by an elastic transformation $\boldsymbol{F}^{\boldsymbol{e}}$ up to the final deformation $\boldsymbol{F}$. The velocity gradient in the current configuration is $\boldsymbol{L} = \dot{\boldsymbol{F}}\boldsymbol{F}^{-1} = \dot{\boldsymbol{F}}^{\boldsymbol{e}}\boldsymbol{F}^{-\boldsymbol{e}} + \boldsymbol{F}^{\boldsymbol{e}}\dot{\boldsymbol{F}}^{\boldsymbol{p}}\boldsymbol{F}^{-\boldsymbol{p}}\boldsymbol{F}^{-\boldsymbol{e}}$ of which symmetric and anti-symmetric part correspond to the strain and spin tensor respectively. When the elastic part $\boldsymbol{F}^{\mathrm{e}}$ of the deformation gradient is small compared to the plastic one $\boldsymbol{F}^{\mathrm{p}}$ (i.e. $\boldsymbol{F}^{\mathrm{e}} \approx \boldsymbol{I}$), the velocity gradient results in $\boldsymbol{L} \approx \boldsymbol{L}^{\mathrm{e}} + \boldsymbol{L}^{\mathrm{p}}$ so that the total strain rate $\boldsymbol{D}$ becomes the sum of the elastic and plastic parts as $\boldsymbol{D} = \boldsymbol{D}^{\boldsymbol{e}} + \boldsymbol{D}^{\boldsymbol{p}}$. Prior to the yield stress, most amorphous polymers show a non linear stress-strain response due to small viscoelastic effects. These are not considered explicitly but their effect on the mechanical response is accounted for by using a secant Young modulus instead of that derived from ultra-sonic measurements of the elastic wave velocities. Its value is estimated from unixial compression tests and an average value for

different strain rates of $E^{secant}=\sigma_y/\varepsilon_y$, with σ_y the yield stress and ε_y the corresponding yield strain, is used. In view of these approximations, the hypo-elastic law is used to express the bulk mechanical response as

$$\overset{\nabla}{\boldsymbol{\sigma}} = \boldsymbol{\mathcal{L}_e D^e} = \boldsymbol{\mathcal{L}_e (D - D^P)} \tag{1}$$

where $\overset{\nabla}{\boldsymbol{\sigma}}$ is the Jaumann rate of the Cauchy stress, $\boldsymbol{\mathcal{L}_e}$ the fourth-order isotropic elastic tensor in terms of secant Young modulus E^{secant} and Poisson's ratio ν, which is in Cartesian components

$$\mathcal{L}_{ijkl} = \frac{E^{secant}}{2(1+\nu)}\left[\left(\delta_{ik}\delta_{jl}+\delta_{il}\delta_{jk}\right)+\frac{2\nu}{1-2\nu}\delta_{ij}\delta_{kl}\right].$$

Within the elastic-viscoplastic framework used here, the plastic strain rate $\boldsymbol{D^P}$ is

$$\boldsymbol{D^P} = \dot{\gamma}^P \frac{\overline{\boldsymbol{\sigma}}'}{\sqrt{2}\tau}, \tag{2}$$

with $\dot{\gamma}^P\left(\tau, p, T\right)$ the equivalent shear strain rate which is temperature and stress dependent, and $\tau = \sqrt{\overline{\sigma}' : \overline{\sigma}'/2}$ the equivalent shear stress. In Eq. 2, the tensor $\overline{\boldsymbol{\sigma}}'$ corresponds to the deviatoric part of the driving or effective stress which is the difference between the applied Cauchy stress $\boldsymbol{\sigma}$ and a back stress $\boldsymbol{b}$ as $\overline{\boldsymbol{\sigma}} = \boldsymbol{\sigma} - \boldsymbol{b}$. The back stress tensor $\boldsymbol{b}$ is due to the entropic back forces generated by the deformation of the polymer chains during the plastic deformation, and will be defined later on. The equivalent plastic shear strain rate $\dot{\gamma}^P$ is taken according to Argon's original idea [ARG73]

$$\dot{\gamma}^P = \dot{\gamma}^0 \exp\left[-\frac{A(s_0+\alpha p)}{T}\left(1-\left(\frac{\tau}{s_0+\alpha p}\right)^{5/6}\right)\right], \tag{3}$$

in which A and $\dot{\gamma}^0$ are material parameters and T is the absolute temperature. The athermal shear strength s_0 in Argon's original formulation is $s_0 = \frac{0.077\times G}{1-\nu}$, with G the shear modulus at high frequency and ν the Poisson ratio. It is worth noting here that the shear modulus G involved in (3) is *not* connected to the the secant Young modulus E^{secant} used in the bulk constitutive law (1). The first determines the activation energy responsible for plasticity locally while the E^{secant} is thought to represent the influence of viscoelastic effects on the bulk mechanical response. This choice for the

value of *G* seems more consistent than an estimate from a tensile or compression tests for which the value derived is dependent on the prescribed strain rate or stress level at which the measurement is performed. The coefficient α represents the pressure sensitivity of the polymer which results in an asymmetric yield stress in tension and compression, for instance.

From a micromechanical point of view, the expression of the temperature and rate dependency of Eq. 3 is general enough to describe the variation of the yield stress of glassy polymers due to viscoplasticity and we adopt this expression even if the physical arguments underlying Argon's view do not receive full agreement in the polymer community.

Following Boyce et al. [BOY88], intrinsic softening is accounted for with the definition of an internal variable s which varies from s_0 to s_{ss} at continued plastic deformation. The internal law $\dot{s} = h\left(1 - s / s_{ss}\right)\dot{\gamma}^P$ governs its variation during deformation, with h a parameter controlling the rate of softening and s_{ss} the value of s in a steady state regime.

The progressive hardening due to the plastic deformation and induced molecular orientation results in a back stress tensor $\boldsymbol{b}$ which can be considered as the development of internal stresses during the deformation. Its description is based on ideas borrowed from theories for rubber elasticity with the cross-links of the rubbers considered as "entanglements" in the case of glassy polymers [BOY88, Wu93]. The deformation of the resulting network is assumed to derive from the cumulated plastic stretch [Wu93] so that the principal back stress components b_α are functions of the principal plastic stretches λ_β as

$$\boldsymbol{b} = \sum_\alpha b_\alpha \left(\boldsymbol{e}_\alpha^p \otimes \boldsymbol{e}_\alpha^p\right),\ b_\alpha = b_\alpha\left(\lambda_\beta\right), \tag{4}$$

in which $\boldsymbol{e}_\alpha^p$ are the principal directions of the plastic stretch. The estimate of the back stress $\boldsymbol{b}$ used in our description is due to Wu and Van der Giessen [Wu93] on the basis of their analysis of the fully three-dimensional orientation distribution of molecular chains in a non-Gaussian network. Wu and

Van der Giessen have shown that a fairly good estimate of the back stress tensor $\boldsymbol{b}$ can be obtained with the following combination of the three-chains and eight-chains [ARR93] models as

$$b_\alpha^{n-ch} = (1-\rho) b_\alpha^{3-ch} + \rho b_\alpha^{8-ch}, \tag{5}$$

with $\rho = 0.85\,\bar{\lambda}/\sqrt{N}$, $\bar{\lambda} = \max(\lambda_1, \lambda_2, \lambda_3)$ the maximum plastic stretch and N the average number of segments between entanglements. The limit stretch of a molecular chain is $\lambda_{\max} = \sqrt{N}$. The expressions for the principal components of b_α^{3-ch} and b_α^{8-ch} contain an additional parameter: the shear modulus C^R of the network taken as $C^R = nk_BT$, n being the entanglement density, k_B the Boltzmann constant and T the temperature.

The above constitutive model has been implemented in a user-define UMAT subroutine in Abaqus [ABA10] 'standard'. Quasi-static calculations are carried out. The time integration scheme and related tangent stiffness matrix presented in [Wu96] are used and implemented in the UMAT. The back stress (Eq. 5) is calculated from the current value of the plastic strain tensor. The related non linear constitutive equations (1-5) are solved with an iterative Newton Raphson procedure.

II.2.2. Materials under considerations

A set of bulk parameters representative of polycarbonate is used and named 'Material A-REF'. Two others glassy like materials with a progressively larger softening are considered and named 'Material B' and 'Material C'. In order to compare the predicted notch tip fields for typical glassy polymers to a characteristic constitutive law for metals, without softening, the 'Material M' is also considered. Their response for uniaxial compression at a constant strain rate $\dot{\varepsilon}_0 = 1\times10^{-3}/\mathrm{s}$ is presented in Figure II-1. The corresponding parameters are presented in Table II-1. The four materials under considerations differs only by the ratio between the steady state yield strength s_{ss} with respect to the initial one s_0. The temperature is T=293K and a typical value s_0=88MPa is used. The notch tip plasticity for a Single Edge Notch Tension (SENT) is examined next for two dimensional (2D) plane strain conditions and in three dimension (3D) calculations. Neither crazing nor failure are considered in this chapter. This is postponed for the next chapter III.

	E/s_0	ν	α	As_0/T	$\dot{\gamma}_0(/s)$	s_{ss}/s_0	h/s_0	C^R/s_0	N
Mat A	14.7	0.39	0.08	649.	9.2×10^{-9}	0.77	5.1	0.19	3
Mat B	14.7	0.39	0.08	649.	9.2×10^{-9}	0.66	5.1	0.19	3
Mat C	14.7	0.39	0.08	649.	9.2×10^{-9}	0.55	5.1	0.19	3
Mat M	14.7	0.39	0.08	649.	9.2×10^{-9}	1.	5.1	0.19	3

Table II-1 : Bulk parameters for the materials under consideration, for the reference material A, for polymer like materials (B and C) exhibiting a larger strain softening and for a hardening-metal like-material M.

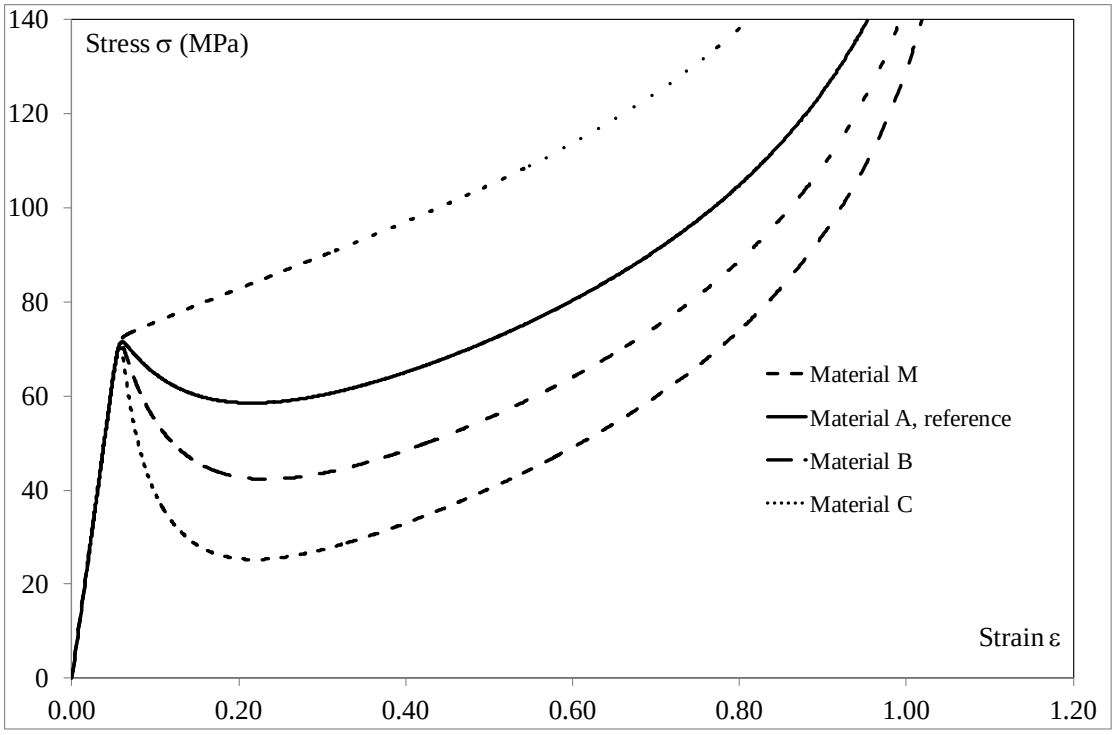

Figure II-1**:** Stress – Strain response of the materials under consideration for uniaxial compression at strain rate $\dot{\varepsilon} = 1\times10^{-3}$/s for the reference material A, for polymer like materials (B and C) exhibiting a larger strain softening and for a hardening-metal like-material M.

II.3. Problem formulation

In this section, we present the geometry of the specimen under consideration and the mesh used for the finite element analysis.

II.3.1. **Description of geometry and mesh discretization**

The 2D and 3D SENT specimens have an identical geometry with height *h*=40 mm, width *w*=20mm and a crack length *a*=10mm. The geometry and mesh discretization are presented in Figure II-2. Refined elements are used around the notch to capture accurately the stress-strain fields. In the region remote from the notch area, coarser elements are used. The element type is CPER for the 2D plane strain calculations consisting in four nodes quadratic elements with a reduced integration. In the 3D calculations, the 3D elements are C3D20R consisting in 20-node quadratic bricks, with reduced integration. The amount of elements across the thickness is increased with the thickness increasing, their dimension remaining identical. For instance with *R*=0.25 mm and thickness *t*=1 mm, the mesh comprises of 12 layers of elements through the thickness of the specimen; a total number of 15558 quadratic elements and 70574 nodes are employed. The smallest element has an edge of 0.0027mm. A constant displacement rate $\dot{u}$=5 mm/s is prescribed on the top surface to mimic a Single Edge Notch Tension for all calculations. An example of a 3D geometry and mesh of thickness t=4mm is presented in Figure II-3. Different mesh densities are used to reduce the total amount of nodes. The larger mesh density is found around the notch. This progressively decays with the distance from the notch. Each part is meshed separately and 'TIE' conditions are prescribed between each part consisting in abaqus in prescribing a continuous displacement. The remote displacement rate is $\dot{u}_0 = 5\,\mathrm{mm/s}$ corresponding to a strain rate $\dot{\varepsilon}_0 = \dot{u}_0 / h = 1.25\times10^{-1}/s$. For such a strain rate, thermal effects are likely to be observed (see for instance [BAS02, SAA06] and a coupled thermomechanical calculations necessary. This has not been considered here as varying the strain rate induces only a variation of the apparent yield stress and a vertical shift in the mechanical response presented in Figure II-1. Thus, the choice of the prescribed strain rate is somehow arbitrary but we have used the same remote conditions for all calculations.

We use a blunted notch that would correspond to the blunting of a sharp crack up to this initial geometry. This is also motivated by experimental issues in which practically machining a sharp notch in ductile polymers like polycarbonate is difficult if not impossible experimentally. The preparation of a blunted notch is preferred for the fracture measurements to be reproducible. The foregoing constitutive law is implemented in a UMAT subroutine in Abaqus 6.10-2 [ABA10] and used for the calculations to be presented in the sequel.

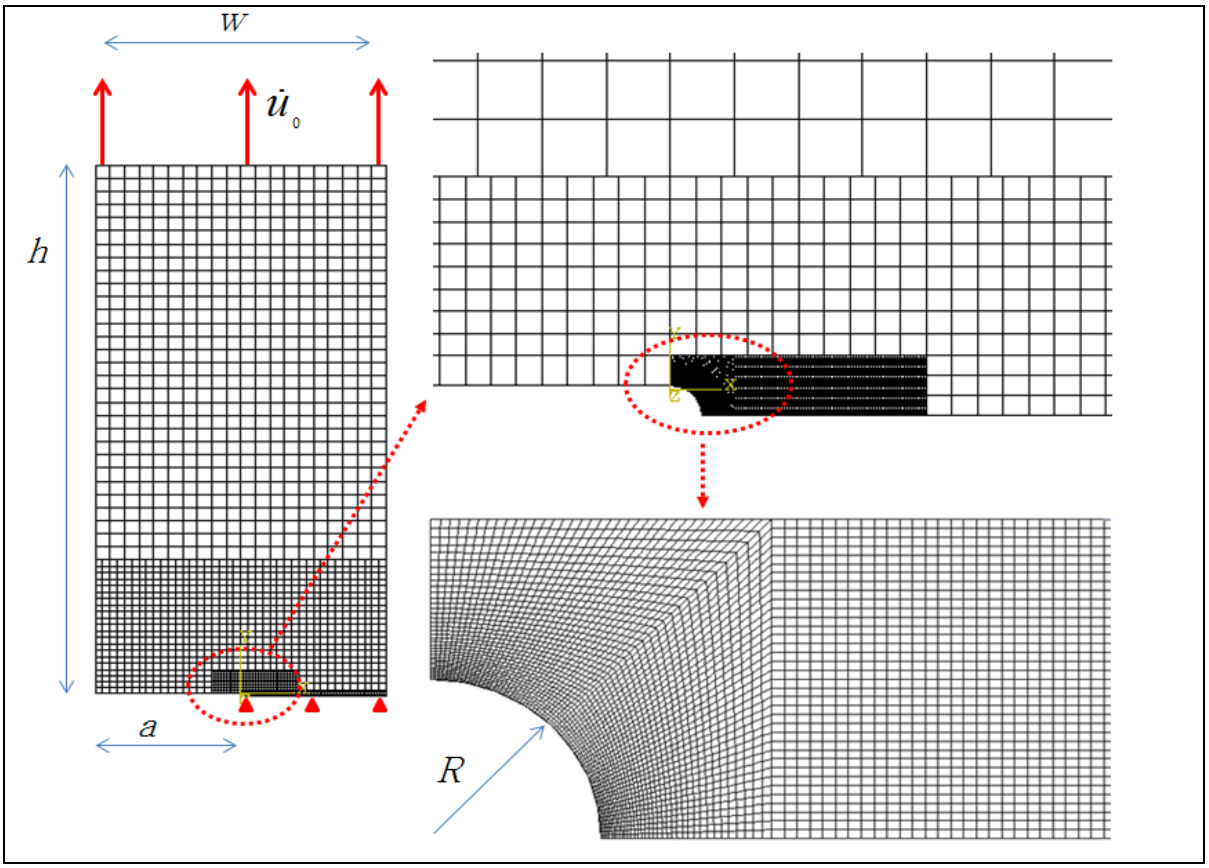

Figure II-2: Description of the mesh used for the 2D plane strain calculations. For 3D simulations, an extrusion of the above section is performed along the thickness t. The total height h=40mm, the width is w=20mm and the initial notch length is a=10mm. The mesh is refined around the notch of which radius is denoted R=0.25mm taken as a reference notch radius. The sample is subjected to a uniform displacement rate $\dot{u}_0 = 5\,\text{mm/s}$ corresponding to the strain rate $\dot{\varepsilon}_0 = \dot{u}_0 / h = 1.25\times10^{-1}\,/\,s$.

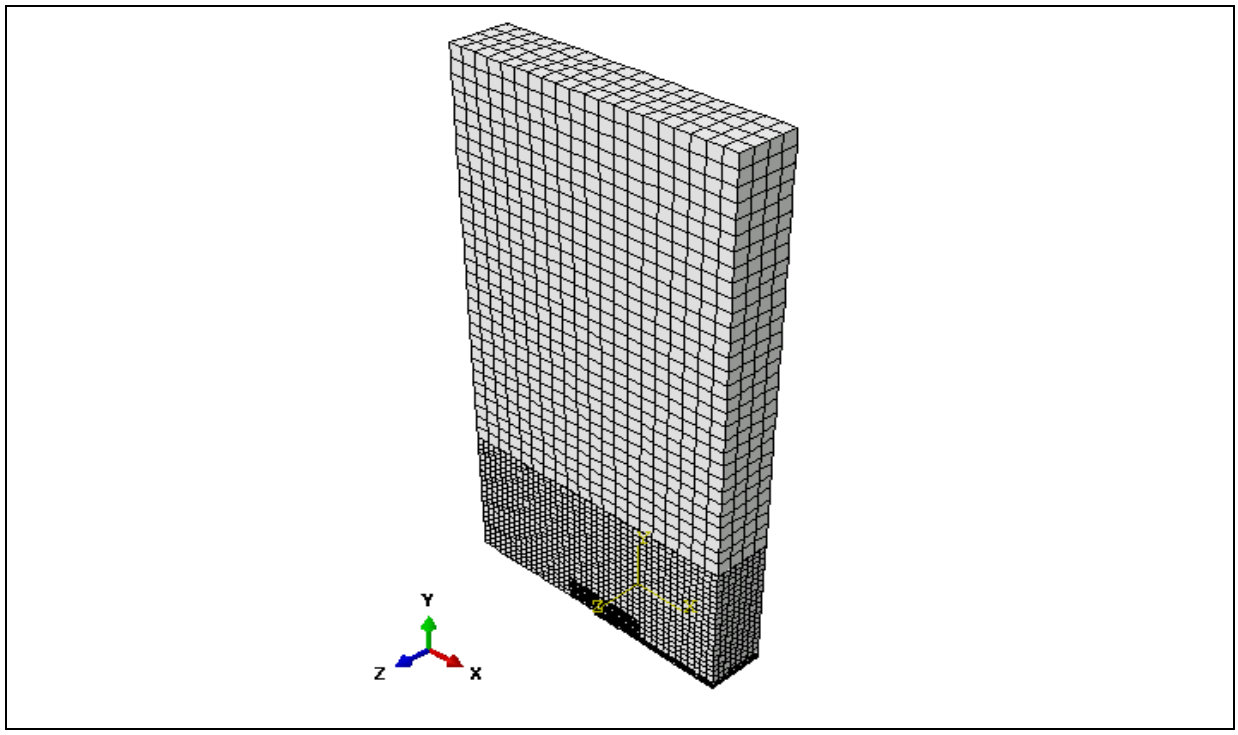

Figure II-3: Example of a 3D sample extruded from Figure II-2 up to a thickness t = 4mm.

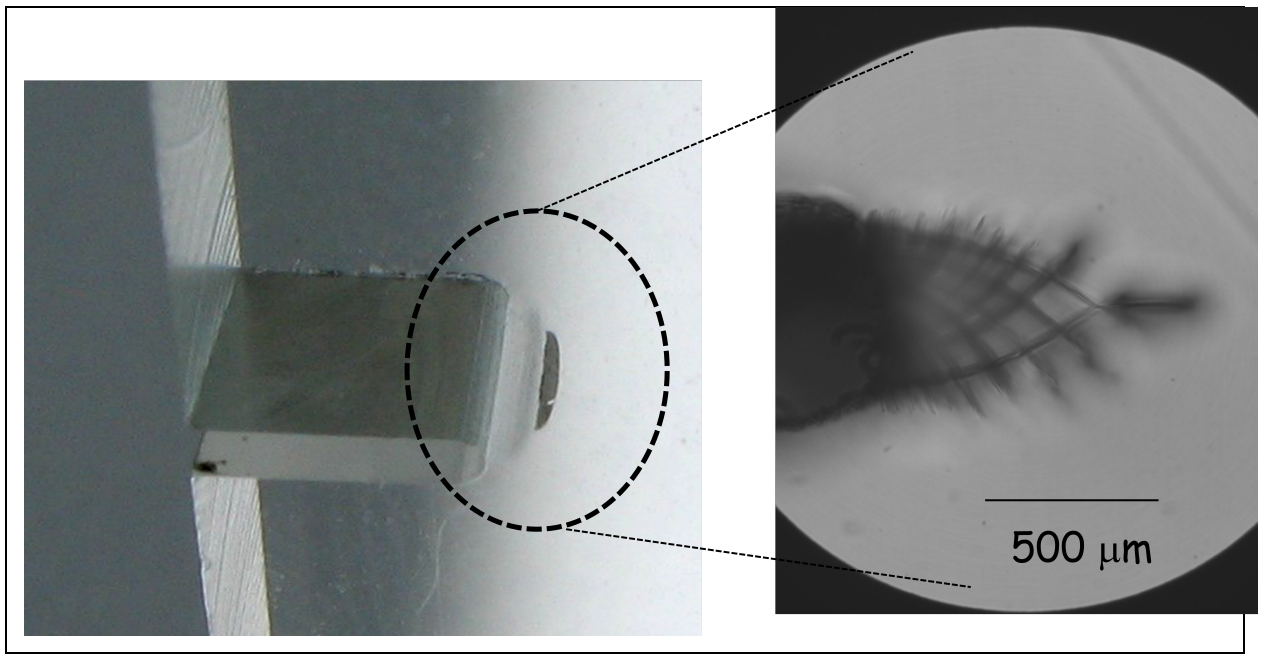

Figure II-4: SENT sample of polycarbonate loaded under tension (geometry identical to that presented in Figure II-2). Observations by transmission plastic zone (opaque zone on the left, slip lines on the right) at the tip of the plastic zone, a stable crack has initiated, where the maximum mean stress is located.

II.4. 2D and 3D Crack tip plasticity investigations

II.4.1. Qualitative description of a SENT with blunted notch experiment

In order to help in analysing the forthcoming simulations, we present a simple experiment performed on a sample of polycarbonate that has the same geometry as that reported in Figure II-2. A slower average strain rate $\dot{\varepsilon}_0 = 1\times10^{-3}/\mathrm{s}$ is prescribed so that the test can be interrupted when a noticeable plastic zone has developed around the notch, at the onset of crazing and related stable crack growth. Observations by light transmission are reported in Figure II-4. On the left, the entire crack length and notch are presented, across the thickness of the sample (t=10mm). Around the notch, an opaque zone can be distinguished and at its tip, a mirror like zone corresponds to the nucleation of a crack. On the right, a closer observation under crossed polarisers is reported: shear bands in the form of slip lines are clearly observed. These are similar to the observations reported by Ishikawa et al. [ISH77] for a notched polycarbonate under bending. The experiment reported here serves essentially to illustrate the type of plastic zone expected for a relatively thick sample (t=10mm) with respect to the initial notch radius R=0.25mm. Slip lines are characteristic for glassy polymers with an angle at their intersection distinct from $\pi/2$ found in elastic perfectly plastic materials (Hill's solution [HIL50]).

In the case of a thin sample, for a geometry corresponding to thin sheets of polymer films usually below 1mm thickness, the plastic zone is totally different from that observed in Figure II-4: a flame like profile parallel to the notch plane is reported for instance by Cortet et al. or Hashemi and Williams [COR07, COR08, HAS00] with no clear evidence of a strain localization from a single (or various) shear band(s).

These two cases enable to distinguish plane stress or plan strain dominant conditions from the observations of the shape of the plastic zone. This will be used in the analysis of the predicted plastic zones from the simulations to be presented in the sequel and accompanying analysis of the stress tip field.

II.4.2. **2D plane strain crack tip plasticity**

We first present 2D plane strain calculations for the four materials under consideration in Figure II-1. The geometry and mesh used for the calculations are those presented in Figure II-2 and the initial notch radius is R = 0.25 mm. A constant displacement rate $\dot{u}_0 = 5\,\text{mm/s}$ is prescribed. The calculations are performed under the assumption of isothermal conditions so that the material's mechanical response shows softening upon yielding followed by progressive hardening for materials A-B-C, and a hardening like response for material M. Neither a contribution from temperature effect resulting in an enhanced strain softening nor a delayed or vanishing back stress are considered. The distribution of the plastic shear strain rate $\dot{\gamma}^P$ normalized with the average strain rate $\dot{\varepsilon}_0 = \dot{u}_0 / h$, $\dot{\gamma}^P / \dot{\varepsilon}_0$, is reported in Figure II-5. The cumulated plastic shear strain γ^P is presented in Figure II-6. The calculations under consideration in this section are comparable to the cases investigated by Lai and Van der Giessen [LAI97] who analyzed the crack tip plasticity by investigating the distribution of the plastic shear strain rate. In the present study, we report the distribution of both the plastic shear strain rate and cumulated plastic shear strain for identical remote load levels. These are represented by 'Time steps' which correspond to the fraction of a total prescribed displacement u_0 = 5mm corresponding to a total axial strain $E_{\text{axial}}^{\text{TOT}} = 5/40 = 12.5\%$. For instance, a time step of 0.1 corresponds to a prescribed macroscopic strain $E_{\text{axial}} = 0.1 \times E_{\text{axial}}^{\text{TOT}} = 1.25\%$.

For the reference material A, plasticity initiates at the notch tip and expands in the form of a single shear band that can be tracked with the distribution of the plastic shear strain rate(see Figure II-5). The onset of strain localization starts at the notch tip and propagates along the free surface of the notch at 45° from the normal. The corresponding distribution of the cumulated plastic shear strain (see Figure II-6) shows a maximum near the surface that decays ahead in the bulk. The shape of the plastic zone is typical of glassy polymers [LAI97] with a profile similar to that predicted by Hill's [HIL50] for a perfect plastic material. As observed by Lai and Van der Giessen from the plastic shear strain rate distribution, the shear bands cross the notch symmetry plane with an angle different than 90° predicted by Hill's slip lines.

For the material B with a larger strain softening compared to material A, the plastic shear strain rate appears more heterogeneous(see Figure II-5). A primary shear band that emerges from the notch surface and propagates similarly to a slip line, similarly to the case of material A, is also observed. However, additional shear bands are triggered from the notch symmetry plane that propagates at approximately 45° from the horizontal symmetry plane. This case has also been studied by Lai and Van der Giessen [LAI97] who showed that these secondary shear bands initiate at the crossing of the primary strain localization regions. Here, we also present the cumulated plastic shear strain which is observed to be more heterogeneous (see Figure II-6) to that of material A, with well defined regions of cumulated plastic deformation. The distribution of the plastic strain of material B with a heterogeneous plastic zone in the form of shear bands is qualitatively in very good agreement with available observations of plastic deformation around a notch (for instance [ISH77]).

For the material C with the largest magnitude in strain softening under consideration here, more heterogeneous shear bands are also observed. The plastic shear strain rate distribution (Figure II-5) represents that the plastic activity is more heterogeneous to that observed for material B with peaks at various locations in the bulk. More insight is provided by the distribution of the cumulated plastic deformation (Figure II-6) where thin and multiple shear bands are observed.

For the three polymer like materials A-B-C, the plastic strain rate distributions presented in Figure II-5 serves to track the instantaneous plastic activity $\dot{\gamma}^P$ during the loading. This is useful to capture the location of current strain localization in the case of material A for which the plastic zone is quite homogeneous (see Figure II-6). However, the cumulated plastic strain for materials B and C are observed heterogeneous with marked shear bands. These distributions can be directly compared qualitatively with plastic regions observed experimentally by light transmission (see [ISH77] for instance) where dark lines due to local modification of the material's birefringence is thought to be connected to the extension of polymer chains and local strain localization. Unlike studies reported in the literature that characterize strain localization in glassy polymers with the distribution of the plastic strain rate (for instance Lai and Van der Giessen [LAI97], Kweon and Benzerga [KWE13]), insight is

also provided by the contours of the cumulated plastic strain for material having enough strain softening.

To complete these 2D plane strain analyses of the plastic zone, the material M without strain softening and only a hardening like response during deformation is now considered. This stress-strain response is representative of most metals. The plastic shear strain rate and the cumulated plastic deformation are presented in Figure II-5 and Figure II-6. Plasticity initiates at the notch tip and increases with the loading. The contour of the plastic strain rate and cumulated plastic deformation are similar and their shape is typical of metals with an expansion of the plastic region to a kidney shape. This is presented in Lai and Van der Giessen [LAI97] but for the load levels considered here, only the onset of a kidney shape profile is observed.

In Figure II-7 the distribution of the mean stress for the four materials are presented. For the polymer like materials A-B-C, the location of the maximum mean stress is initially at the crack tip while the response is elastic, this is progressively shifted ahead of the notch tip, as plasticity develops. This observation was presented by Lai and Van der Giessen [LAI97]. In ductile polymers, failure proceeds by crazing of which initiation is usually governed by the maximum mean stress. Therefore, an accurate estimation of its magnitude and location is necessary in ductile polymer fracture problem. This will be further investigated in the 3D calculations presented in the next section. For the hardening metal like material, a similar variation of the location of the maximum mean stress is observed when plasticity develops around the notch. However, the shape of the plastic zone of material M is different from that of materials A-B-C.

The 2D plane strain calculations presented in this section show that the joined presentation of the distribution of the plastic shear strain rate and cumulated plastic deformation serve to characterize the crack tip plasticity. The plastic zones of polymer like materials A-B-C are qualitatively in agreement with available experimental observations. These are thought relevant for ‘thick’ specimens. 2D calculations also constrain the development of shear bands on a plane along the thickness direction as well as a negligible deformation along the thickness. The evaluation of how much the thickness needs

to be to ensure plane strain dominant conditions remains to be evaluated. This is presented in the next section. However, the information on the crack tip plasticity together with the estimation of the mean stress distribution obtained from the 2D simulations will be used in the 3D analyses to assess whether or not plane strain conditions prevail.

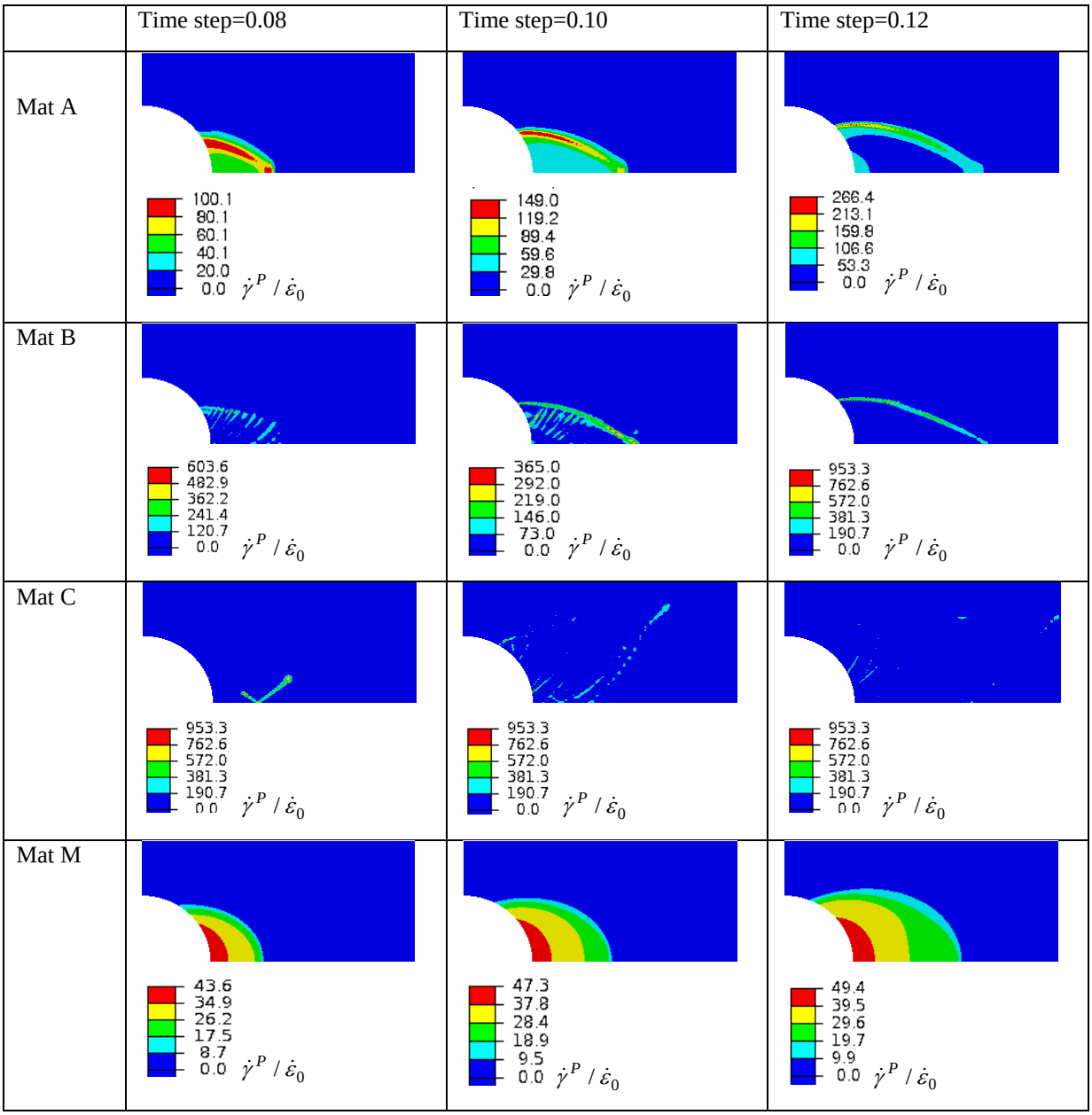

Figure II-5 : Distribution of the shear plastic strain rate normalized with the average strain rate $\dot{\gamma}^P / \dot{\varepsilon}_0$ around the notch for 2D plane strain calculations at various loading times for the four materials presented in Figure II-1

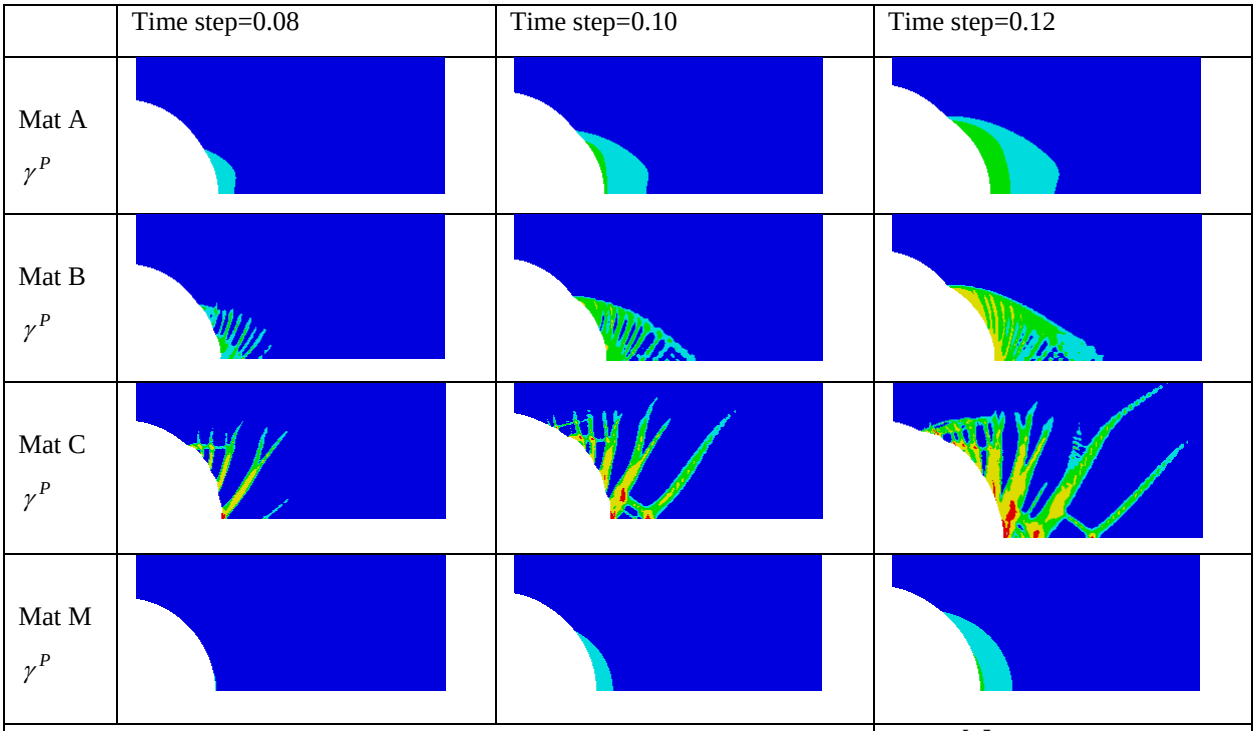

Figure II-6: Distribution of the cumulated plastic shear strain γ^P around the notch for 2D plane strain calculations at various loading times for the four materials presented in Figure II-1 (contour legend identical for all figures).

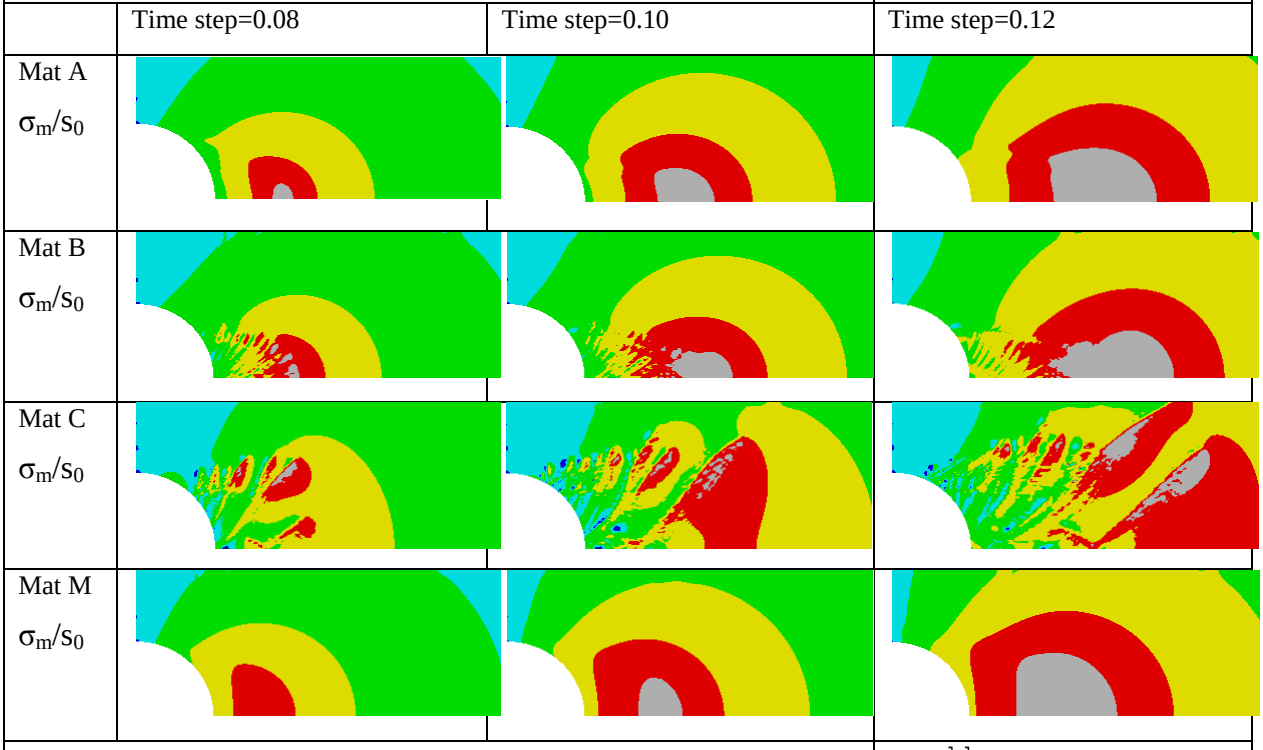

Figure II-7 : Distribution of the mean stress σ_m normalized with the shear strength s_0 around the notch for 2D plane strain calculations at various loading times for the four materials presented in Figure II-1 (contour legend identical for all figures)

II.4.3. 3D crack tip plasticity : reference material A

The material A is first used to investigated 3D crack tip plasticity. For the 3D calculations, 20 nodes quadratic brick elements with a reduced integration are used. Each calculation is run with 4 CPUs and each calculation takes between one day and on week in a standard linux bi-processor four core available of 2012. A reference notch tip R=0.25mm is used and the specimen thickness t is defined with respect to R. Systematically, the plastic shear strain rate $\dot{\gamma}^P$ and cumulated plastic deformation γ^P on the surface and in the center of the thickness are compared, for identical load levels to those reported in the foregoing Figure II-5 and Figure II-6. The samples with t/R = 1, 4 and 16 are first investigated, corresponding to a thickness of 0.25 mm, 1 mm and 4 mm. The plastic strain rate and plastic deformation are presented in Figure II-8 and Figure II-9. The plastic activity is better represented by the distribution of the strain rate reported in Figure II-8. For the thickness t = 4mm (t/R=16), a plastic zone similar to that observed for plane strain conditions (see Figure II-5) is observed with the development of a marked shear band and the shape of the plastic zone typical for glassy polymer. In this case and presumably for larger thicknesses, the plastic zone predicted from 2D plane strain conditions is observed at the center of the specimen. Their magnitude is also comparable to that reported in Figure II-5 for 2D plane strain calculations. At the surface, the magnitude of plasticity is smaller and a reduced amount of plastic deformation takes place. This is confirmed by the distribution of the cumulated plastic strain (Figure II-9) which is larger in the center compared to that of the surface.

For the case with t/R=4 (thickness of 1mm), a modification of the development of plasticity around the notch can be observed: in Figure II-8, in the center there is still not any strain localization and no shear bands are observed at the center. The contour of the plastic strain rate zone becomes broader and is not really oriented towards the notch symmetry plane. The cumulated plasticity reported in Figure II-9 show that this configuration corresponds to a transient regime for which the magnitude of plasticity at the surface and that in the center of the specimen becomes comparable.

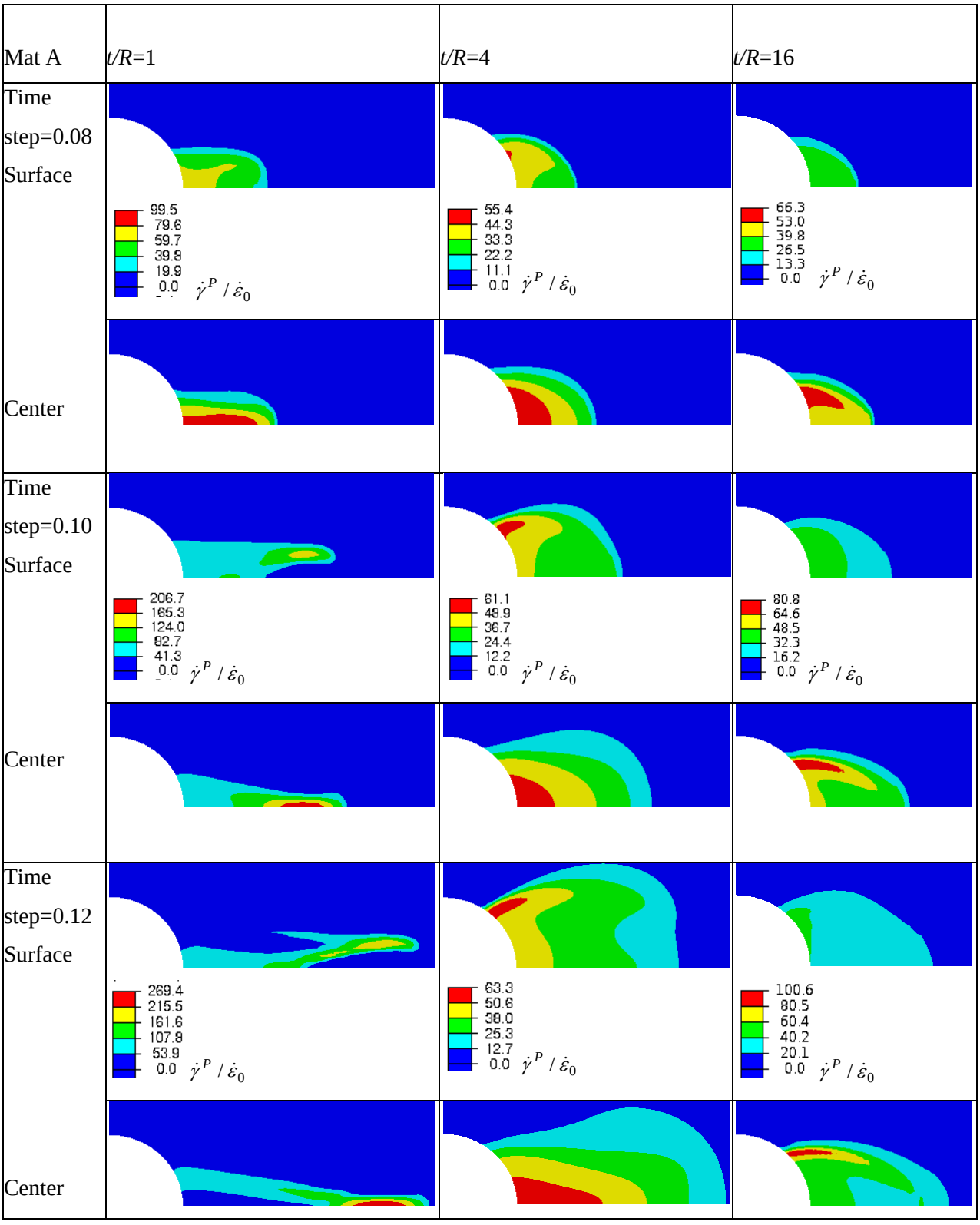

Figure II-8: Distribution of the shear plastic strain rate normalized with the average strain rate $\dot{\gamma}^P / \dot{\varepsilon}_0$ around the notch for 3D calculations at various loading times for the material A, the thickness t is normalized with the notch radius R,R=0.25mm. For each cell, the distribution on the top corresponds to that in the surface, in the bottom to that in the center of the thickness.

Mat A	*t*/*R*=1	*t*/*R*=4	*t*/*R*=16
Time step=0.08 Surface	 γ^P	 γ^P	 γ^P
Center		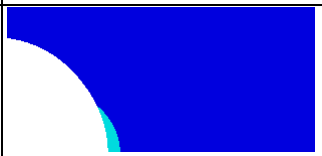	
Time step=0.10 Surface	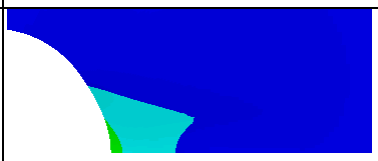 γ^P	 γ^P	 γ^P
Center	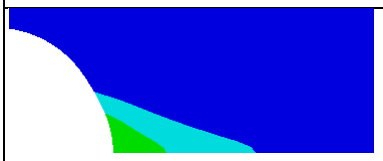		
Time step=0.12 Surface	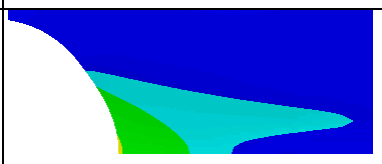 γ^P	 γ^P	 γ^P
Center	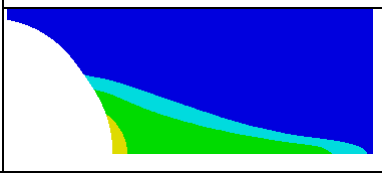	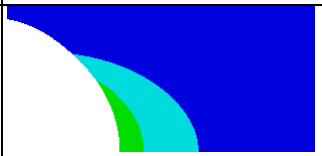	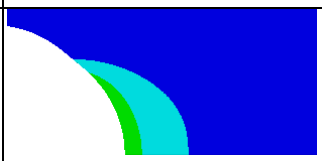

Figure II-9: Distribution of the cumulated shear plastic strain γ^P around the notch for 3D calculations at various loading times for the material A, the thickness *t* is normalized with the notch radius *R*,*R*=0.25mm. For each cell, the distribution on the top corresponds to that in the surface, in the bottom to that in the center of the thickness (contour legend identical for all figures)

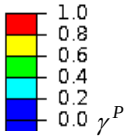

When the thickness is further reduced to 0.25mm (*t/R*=1), a totally different development of plasticity at the notch tip is observed: the plastic strain rate is now completely different from that predicted in the 2D plane strain calculations with a maximum observed along the notch plane at the center of the specimen and no formation of slip lines (see Figure II-8). A more diffused distribution is observed at the surface but the development of the plastic strain rate also follow a direction parallel to the notch plane without initiation of shear bands as in for *t/R*=16. The distribution of the cumulated plastic deformation confirms this observation with a flame like profile in the center of the specimen and a similar one at the surface. This indicates that plane stress conditions prevail for this configuration with *t/R*=1. Actually, the distribution of the plastic deformation for *t/R*=1 (see Figure II-9) resembles to that observed experimentally around notch of polymer sheets or polymer film as reported by Cortet et al. [COR07, COR08] and also in studies devoted to the characterization of the essential work of fracture in polymer film (for instance [HAS00]).

In Figure II-10, the distribution of the mean stress σ_m normalized with the yield strength s_0 at the center of the specimen during the loading for the three thicknesses *t/R*=1, 4 and 16 is presented. The distribution for *t/R*=16 (*t*=4mm) is similar to that reported in Figure II-7 with a marked maximum located at the crack symmetry plane observed ahead the notch tip. For the case with *t/R*=4 (*t*=1mm), a similar mean stress distribution is observed. The magnitude of the maximum mean stress is smaller than the case with *t/R*=16. For the smallest thickness (*t*=0.25mm), the contours of the mean stress appear totally different with the thick sample (*t/R*=16) but still a maximum located along the notch symmetry plane but with a flame like shape related to that of the plastic zone. The variation of the maximum mean stress and related profile are related to the stress constrain (or the absence of constrain) across the thickness: when plane stress conditions prevail as in *t/R*=1, the lowest maximum mean stress is observed for a given load level. This maximum increases with the thickness and the largest value is observed for *t/R*=16.

Mat A	*t*/*R*=1	*t*/*R*=4	*t*/*R*=16
Time step=0.08 Center	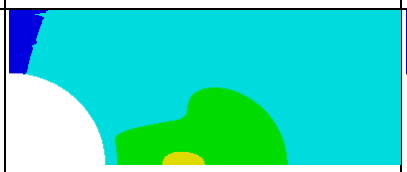		
Time step=0.10 Center			
Time step=0.12 Center	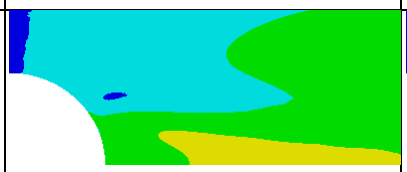		
Figure II-10 : Distribution of the mean stress σ_m normalized with the shear strength s_0 around the notch for 3D calculations at various loading times for the material A , the thickness *t* is normalized with the notch radius *R*,*R*=0.25mm. For each cell, the distribution on the top corresponds to that in the surface, in the bottom to that in the center of the thickness, material A.(contour legend identical for all figures)			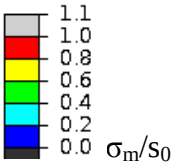

Additional calculations have been performed with different thicknesses with *t*/*R*=8, 12 and 24 corresponding to intermediate thicknesses of *t* = 2 mm and 3mm (*t*/*R* = 8 and 12, respectively) and a larger one with t = 6mm (*t*/*R* = 24). The distribution of the plastic shear strain rate is presented in Figure II-11. Strain localization in the form of a single shear band can be distinguished as soon as t=2mm, *t*/*R*=8 and for larger thickness. The plasticity localizes in the form of a broad shear bands across a broad plastic zone, as seen in in Figure II-8. For the case with thickness of 3 mm, the shear bands that emerges at the center tends to propagate towards the notch symmetry plane. This is not as marked as in the case with *t* = 6mm (*t*/*R*=24) but the distribution for *t* = 3mm (*t*/*R*=12) at the time step =0.12 becomes comparable to a slip lines picture.

For the 2D plane strain calculation and for all 3D configurations with a thickness increasing from 0.25mm to 15 mm, the variation of the maximum mean stress versus thickness, located along the crack

symmetry plane *and* in the center of the specimen is plotted against the loading (Time step of which value times the reference macroscopic strain rate $\dot{\varepsilon}_0$ determines the prescribed macroscopic axial strain), as shown in Figure II-12. The variation of the maximum is examined as this quantity is usually used for the criterion for craze initiatrion that provides some insight of the resistance to fracture of a given polymer. The plot corresponding to the variation for 2D plane strain is observed above all the other cases. The smallest thickness with t = 0.25mm corresponds to 2D plane stress conditions. The 3D calculations with a thickness of 1, 2, 3, 4, 6, 8,12 and 15mm are observed in between these two cases that appear to bound the variation of the maximum mean stress during the loading. For a given load level, the observed maximum mean stress increases with the thickness. This can be interpreted with a progressive transition from plane stress to plane strain conditions. However, even for a thickness as large as 8mm(12mm and 15mm thick specimens have also been investigated), the corresponding plot is below that for a pure plane strain assumption. The corresponding amount of plasticity with a cumulated plastic deformation as large as 0.4 to 0.6 (see Figure II-9) induces a noticeable deformation in the thickness so that plane strain conditions are not totally fulfilled: the mean stress distribution from 3D calculations in the center is still below that predicted in 2D plain strain calculation (see Figure II-12). This observation has an important consequence in the analysis of polymer deformation around a notch: a full 3D calculation is necessary for the estimation of the stress distribution, even if the crack tip plastic fields are similar when comparing 2D plane strain calculation and 3D calculations as long as the ratio *t/R* is larger than 16. The implication of the 2D plane strain versus 3D calculations will be examined in the next chapter with the investigation of fracture.

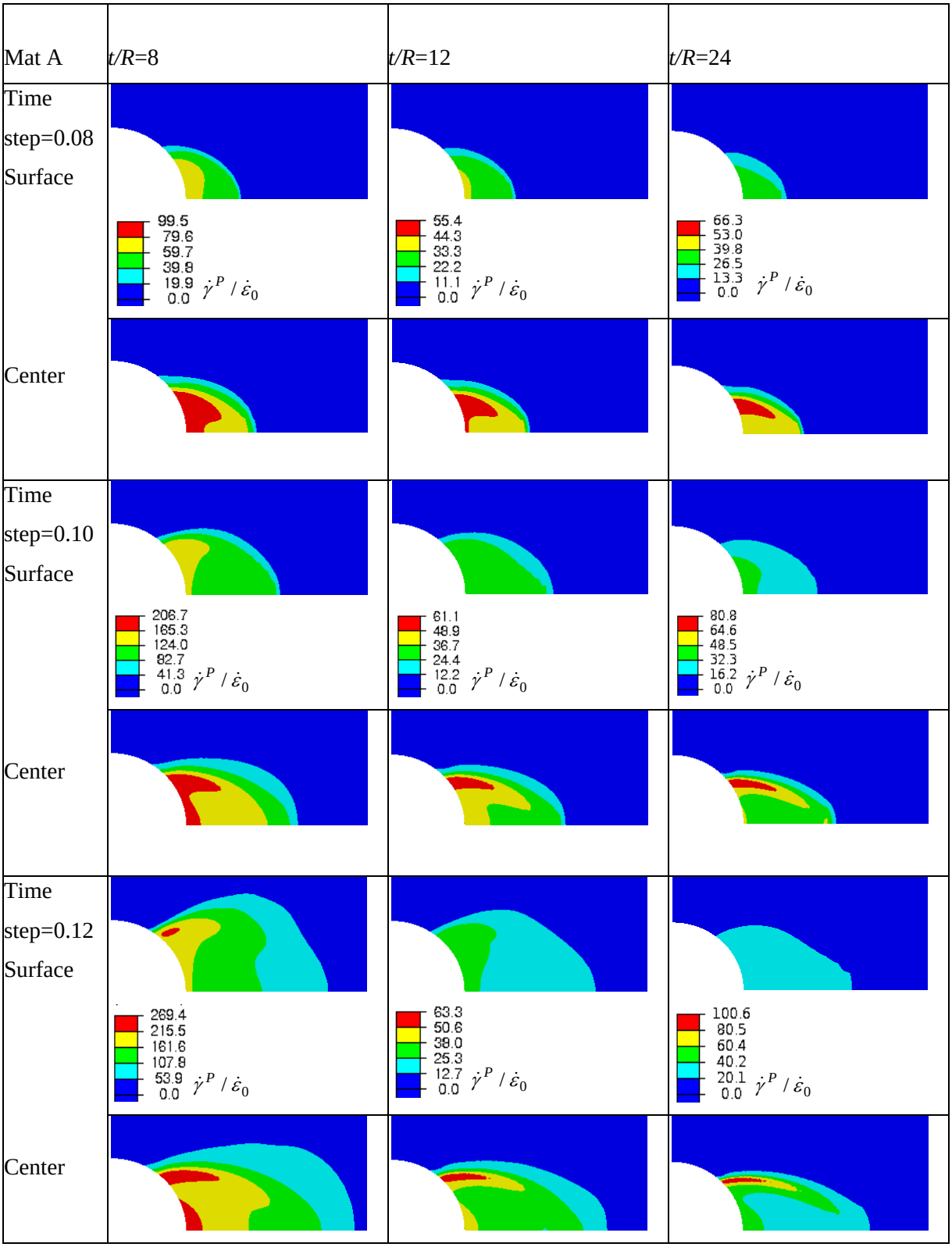

Figure II-11: Distribution of the shear plastic strain rate normalized with the average strain rate $\dot{\gamma}^P / \dot{\varepsilon}_0$ around the notch for 3D calculations at various loading times for the material A, the thickness *t* is normalized with the notch radius *R*,*R*=0.25mm. For each cell, the distribution on the top corresponds to that in the surface, in the bottom to that in the center of the thickness.

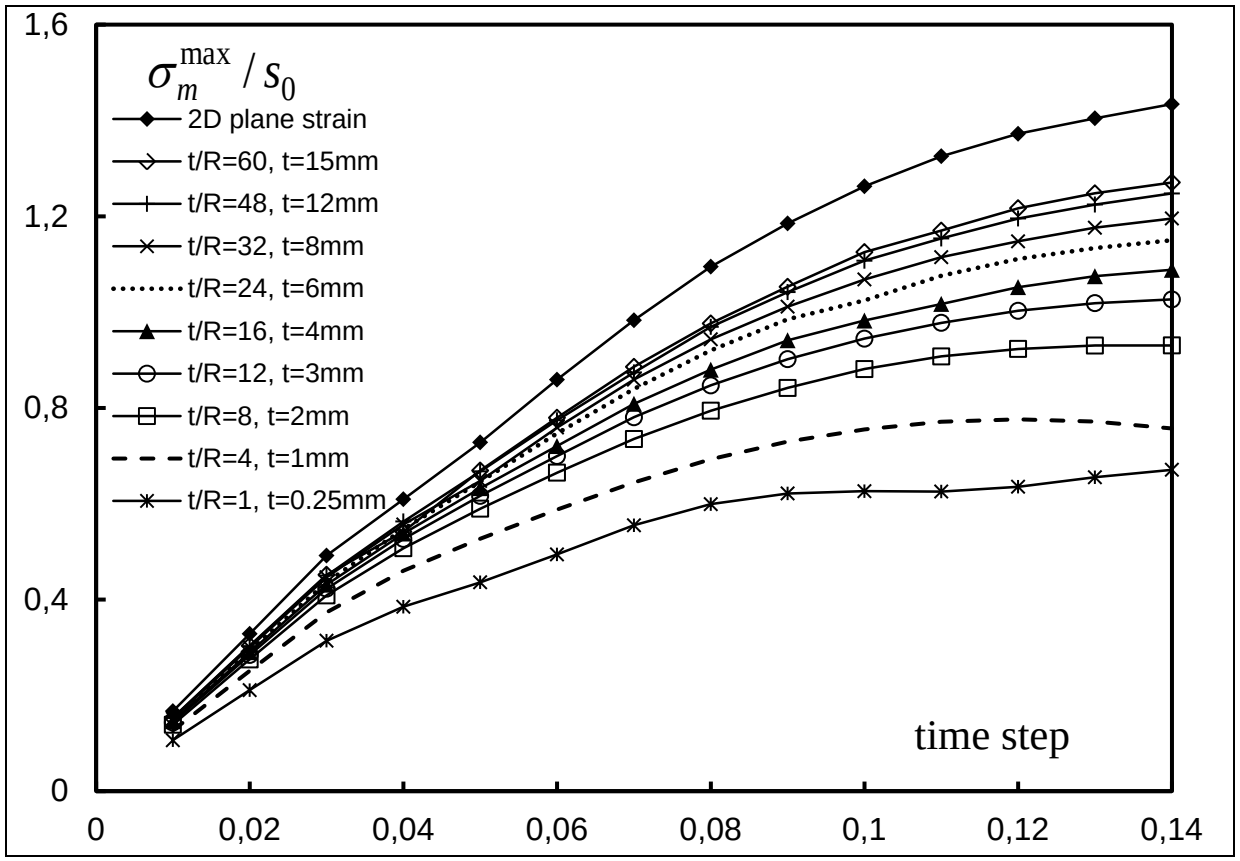

Figure II-12 : Variation of the maximum mean stress on the notch symmetry plane during the loading for 2D plane strain conditions and the 3D samples of thickness increasing from 0.25mm to 8 mm and two additional cases with a thickness of 12mm and 15mm, the notch tip radius is 0.25mm, material A.

II.4.4. Influence of the strain softening on 3D crack tip plasticity

The influence of the strain softening typical for glassy polymers is now investigated for the material B. Around the notch tip, strain softening triggers the formation of shear bands which develop towards the notch symmetry plane, which is crossed by the shear bands for sufficiently large deformation. At the location of the shear bands crossing, the mean stress is enhanced to ensure the material's continuity(see Figure II-7). Thus, the shear bands patterning and magnitude of the plastic deformation inside a band are likely to influence the mean stress distribution discussed in the forgoing section. This is examined in the present section.

Mat B	*t*/*R*=1	*t*/*R*=4	*t*/*R*=16
Time step=0.08 Surface	 γ^P	 γ^P	 γ^P
Center	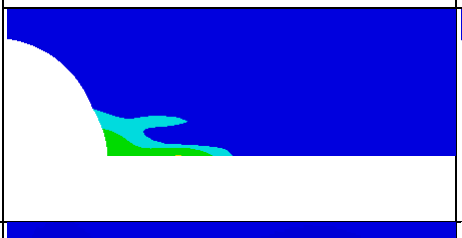	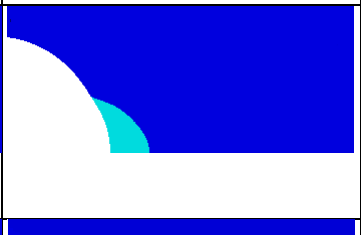	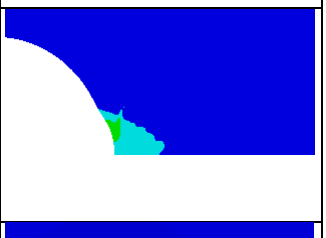
Time step=0.10 Surface	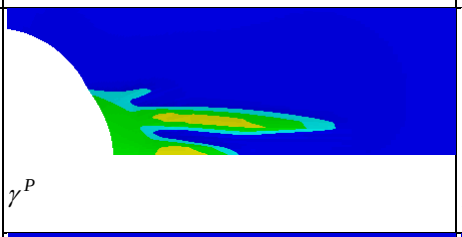 γ^P	 γ^P	 γ^P
Center	 γ^P	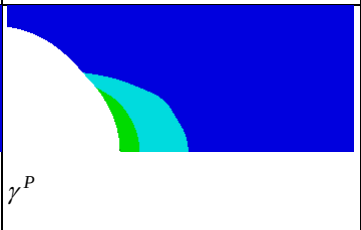 γ^P	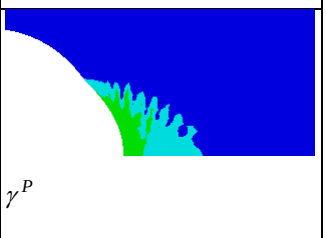 γ^P
Time step=0.12 Surface	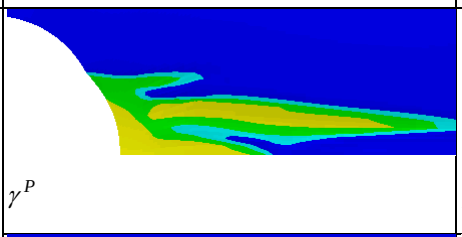 γ^P	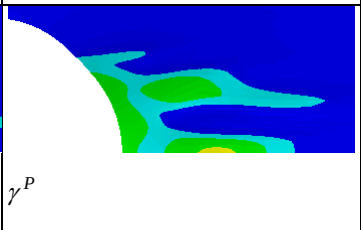 γ^P	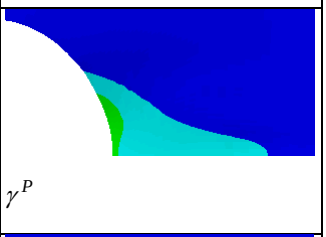 γ^P
Center	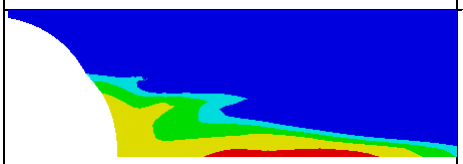	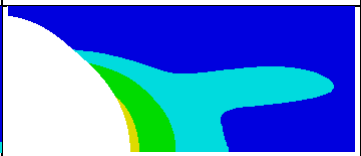	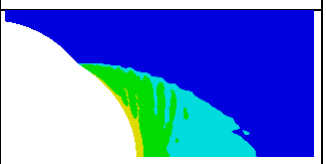

Figure II-13: Distribution of the cumulated shear plastic strain γ^P around the notch for 3D calculations at various loading times for the material B, the thickness *t* is normalized with the notch radius *R*,*R*=0.25mm. For each cell, the distribution on the top corresponds to that in the surface, in the bottom to that in the center of the thickness (common contour legend)

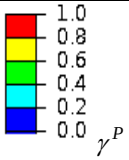

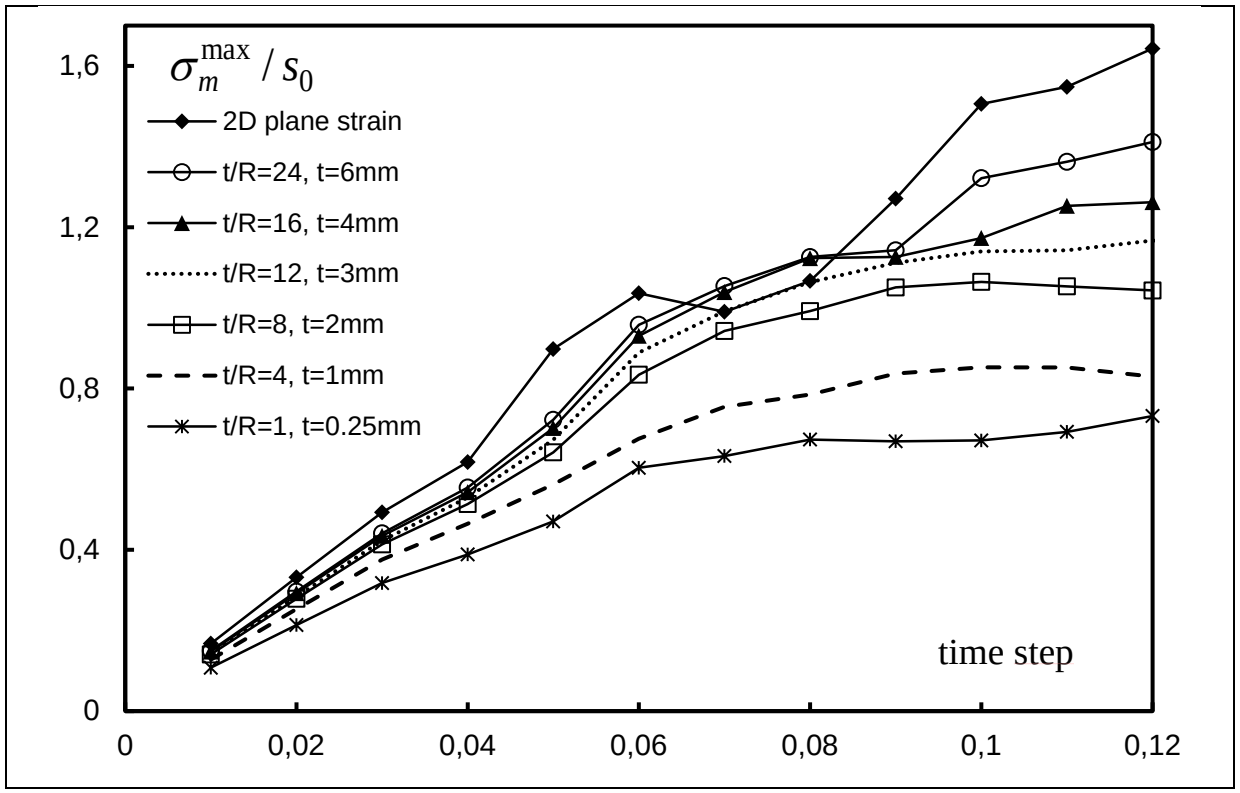

Figure II-14 : Variation of the maximum mean stress on the notch symmetry plane during the loading for 2D plane strain conditions and the 3D samples of thickness increasing from 0.25mm to 6 mm, the notch tip radius is 0.25mm, material B.

In Figure II-14, we present the variation of the maximum mean stress on the notch symmetry plane during the loading. For the 2D plane strain calculation, the mean stress increases up to the time step 0.06. For this load level, a decrease is observed followed by a progressive increase from time step equals to 0.10. In Figure II-7, we observe that for material B at load level equals to 0.08, the maximum mean stress is not located on the crack symmetry plane but above from this axis, where the shear bands cross. Thus, for the 2D calculation, the maximum mean stress is first located along the crack symmetry plane, then its location is shifted away from this axis and is again observed in the symmetry plane as the loading continues. In the 3D calculations corresponding to the thinner thickness, *t/R*=1, the maximum mean stress first increases and then reaches a plateau at approximately a load level equals to 0.07. As the thickness increases, a monotonic grows of the maximum mean stress is observed but some inflexion points can appear corresponding to a maximum located out of the plane.

Thus, a largest strain softening can induce a distribution of the maximum mean stress that is not always located on the notch symmetry plane but out of this axis, where shear bands intersect. Similarly to the case for material A (see Figure II-12), the maximum mean stress increases with thickness. However, even for the largest thickness t=6mm, its magnitude is always smaller than that the corresponding to the 2D plane strain assumption. Here also, the distribution of the plastic deformation for 2D plane strain conditions is similar to that observed in 3D calculations in the center as long as the ratio thickness / notch tip radius t/R is larger than 16. However, the 2D plane strain simulations overestimate the magnitude of the stress distribution and 3D calculations are necessary for accurate stress evaluation. Again, the assumption for negligible deformation in the thickness is not fulfilled due to large plasticity and related material's contraction in the notch region.

II.4.5. Influence of the notch radius on 3D crack tip plasticity

For the reference material A, we now investigate how the notch tip radius influences the development of the notch tip plasticity, and in particular investigate the ratio thickness versus notch tip t/R=1, 4 and 16. This is performed for a smaller notch radius R=0.1mm and a larger one R=0.5mm and 3D calculations are reported. By varying the notch radius, the stress concentration at the tip is enhanced when R decreases while it is reduced when R increases. In Figure II-15 and Figure II-16 the plastic strain rate distribution for the specimens with a notch radius R = 0.1mm and R = 0.5 mm are presented respectively. By comparing these contours with the corresponding ones for the reference notch radius R = 0.25mm (see Figure II-9), we observe that the distribution is similar *except* that the corresponding load levels (time step) are different. The plastic strain rate distribution for the reference case with R=0.25mm at the time steps 0.08, 0.10 and 0.12 now correspond to 0.05, 0.06 and 0.07 for the smaller notch radius (R=0.1mm) while 0.11, 0.13 and 0.15 are shown for R=0.5mm. For all these cases, the ratio thickness over notch tip, t/R, is observed to determine the transition between plane stress conditions to plane strain for the development of plasticity. In particular, to consider the value of the thickness only is not sufficient to assess if plane stress conditions prevail. The observation of the shape of the plastic zone with a flame like profile for plane stress and strain localization in the form of

shear bands is a better criterion to distinguish between these two bounds in terms of loading conditions.

The distributions of the mean stress (normalised with the shear strength s_0) for the specimens with notch radii R=0.1mm and R=0.5mm for the cases under consideration are presented in Figure II-17 and Figure II-18, respectively. We observe that for the smaller thickness over ratio, t/R=1, the magnitude of the maximum mean stress is smaller than the case with t/R=16 corresponding to a 'thick' specimen. The mean stress contour for a given ratio t/R is similar for the three notch radii considered and as distinct with R=0.1, 0.25 and 0.5mm. Thus, the previous observation made for the characteristic development of plasticity is also in place here: the mean stress distribution and contour is not governed by the value of the thickness but the governing parameter to distinguish between plane stress versus plane strain dominant conditions appears to be the ratio between the thickness and the notch radius.

This is an important issue for the definition of the sample geometry in fracture tests of their analysis when crack blunting takes place. An initial blunted notch is considered here but blunting is observed in ductile polymers with initially sharp cracks. A blunted crack can be represented by one of the geometry under consideration here. Thus, depending of the sample's thickness, different loading conditions are taking place on the notch. Plane stress conditions for t/R = 1 and when t/R is smaller than 4 corresponds to a transient configuration between plane stress and plane strain dominant conditions. For a larger thickness and t/R equal or larger than 16, plane strain like conditions are met for the distribution of plastic deformation but, as reported in the previous section, 3D calculations are necessary for a realistic estimation of the stress distribution. Failure and fracture tests are investigated in the next chapter.

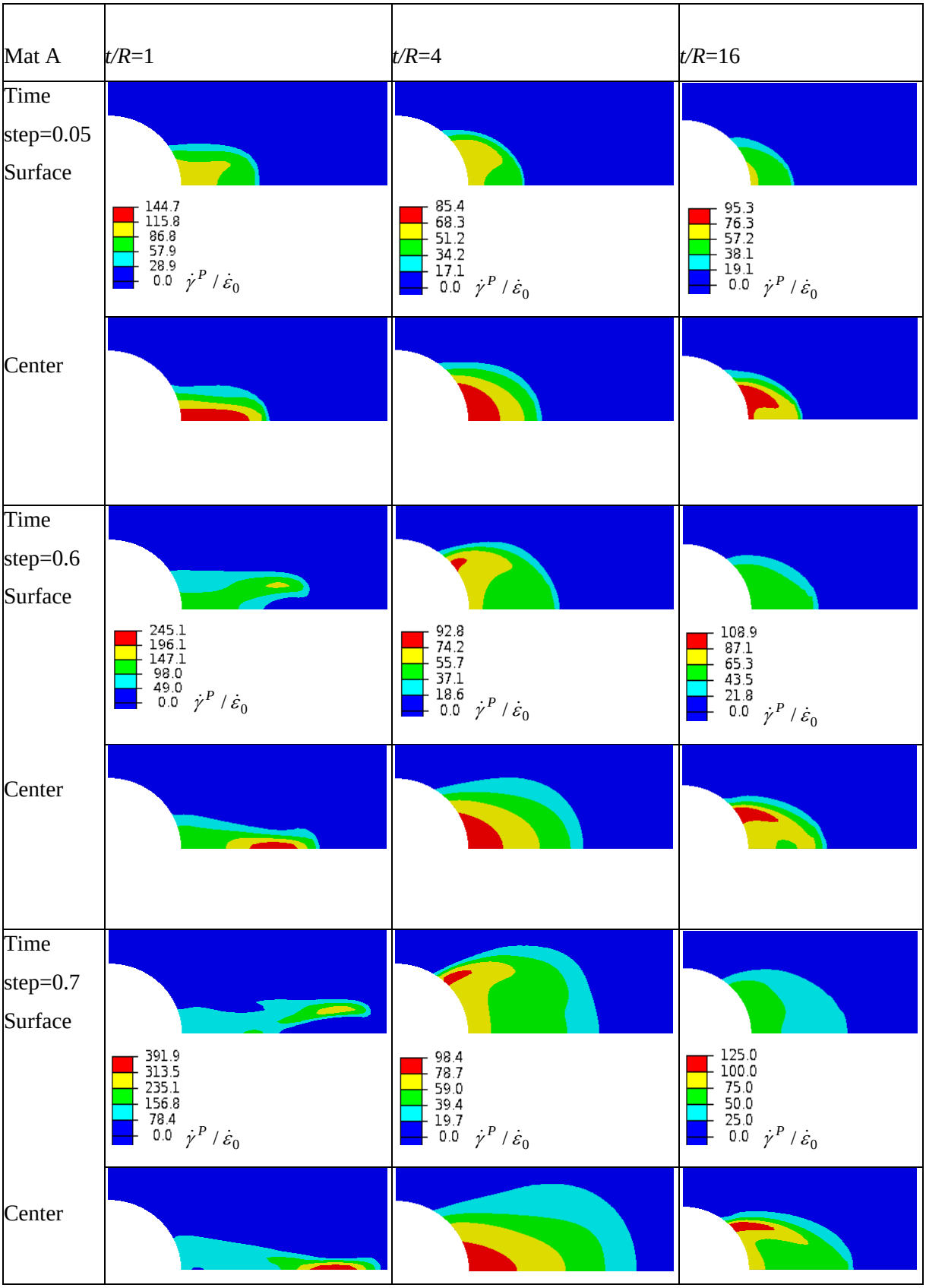

Figure II-15: Distribution of the plastic strain rate for material A, notch tip radius R=0.1mm, for thickness *t* equals to 0.1mm, 0.4mm and 1.6mm. For each time step, the contour in the top corresponds to that at the surface, at the bottom that in the center of the specimen.

Mat A	*t*/*R*=1	*t*/*R*=4	*t*/*R*=16
Time step=0.11 Surface	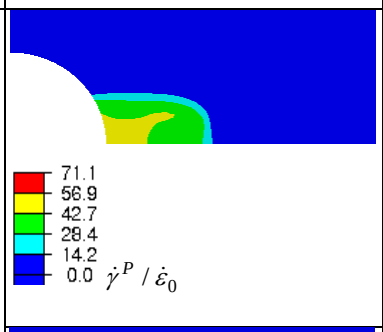	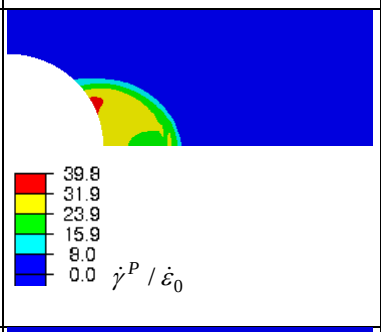	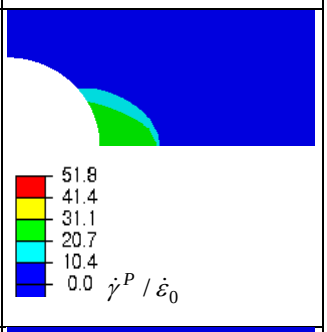
Center	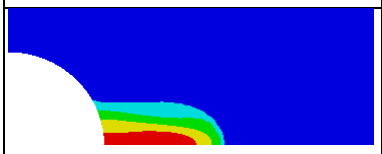	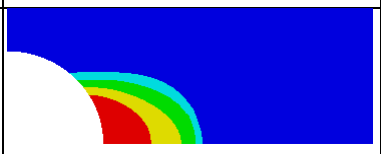	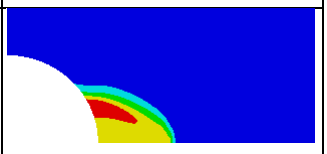
Time step=0.13 Surface	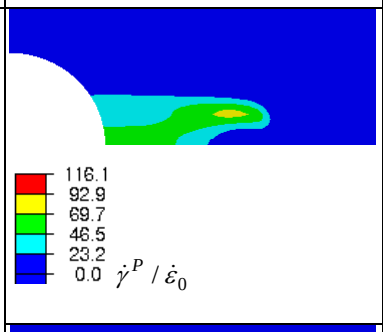	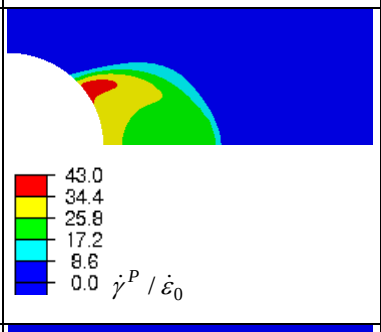	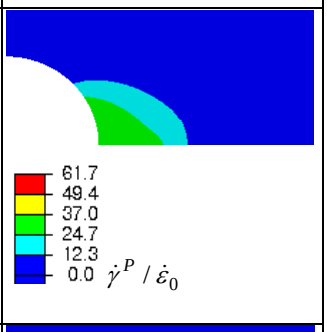
Center	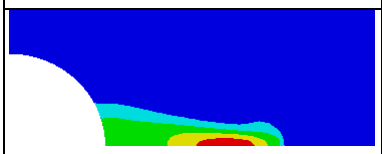		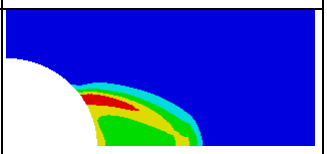
Time step=0.15 Surface	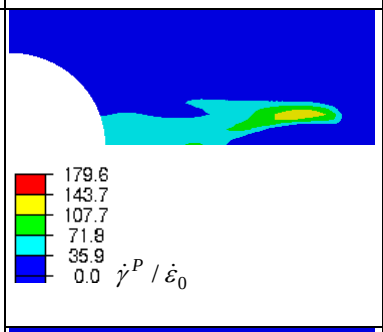	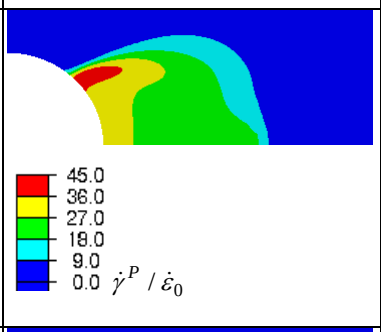	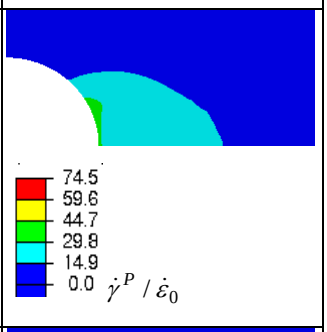
Center	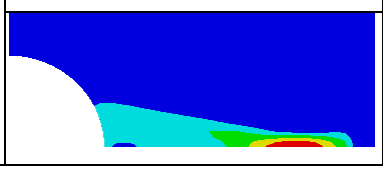		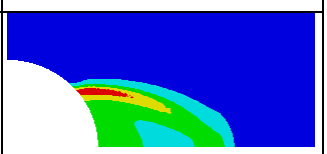

Figure II-16: Distribution of the plastic strain rate for material A, notch tip radius R=0.5mm, for thickness *t* equals to 0.5mm, 2mm and 8mm. For each time step, the contour in the top corresponds to that at the surface, at the bottom that in the center of the specimen.

Mat A	*t*/*R*=1	*t*/*R*=4	*t*/*R*=16
Time step=0.05 Center		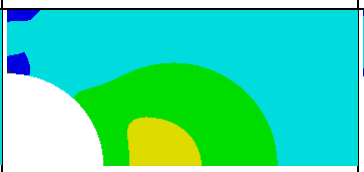	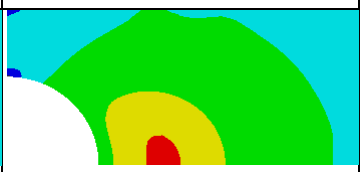
Time step=0.06 Center			
Time step=0.07 Center			

Figure II-17 : Mean stress distribution normalized with the shear strength s_0 for material A and the geometry with notch radius R=0.1mm for a thickness t as t/R=1, 4 and 16(contour legend identical for all figures).

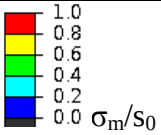

Mat A	*t*/*R*=1	*t*/*R*=4	*t*/*R*=16
Time step=0.11 Center	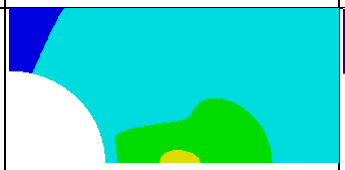		
Time step=0.13 Center			
Time step=0.15 Center			

Figure II-18: Mean stress distribution normalized with the shear strength s_0 for material A and the geometry with notch radius R=0.5mm for a thickness t as t/R=1, 4 and 16(contour legend identical for all figures).

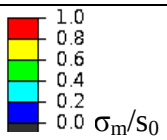

II.5. Discussion

In the 2D plane strain and the 3D calculations reported here, strain localization in the form of shear bands are observed for the strain softening materials. In a numerical investigation of inelastic deformation and localization in polycarbonate, Lu and Ravi-Chandar [LU99] pointed out that macroscopic softening of the specimen does not necessarily imply softening to be an intrinsic property of the material. Shear bands and related strain localization are not observed for a material with a hardening like response, neither in 2D plane strain nor in the 3D calculations. As noted by Kweon and Benzerga [KWE13], in the case of a perfectly plastic material, strain localization with shear bands similar to those predicted in Hill's slip lines analysis [HIL50] is possible, but how realistic this is for polymers? With a constitutive law with no softening nor hardening, the rate dependence of the yield stress of polymers cannot result in perfect plasticity and some hardening like response is expected around the notch, because of the heterogeneous strain rate. Thus, the observation of shear bands originates in the polymer's intrinsic strain softening. Their geometry and magnitude depends strongly on the amount of stress drop after yielding. This is observed in the present study for both the 2D and the 3D calculations. Thus, intrinsic softening is necessary to capture the localized strain fields observed experimentally as in Ishikawa et al.[ISH77, NAR80, ISH83].

3D crack rip fields around a notch have been investigated by Tvergaard and Needleman [TVE08] in the modeling of the IZOD test. Although their study consider dynamic effects, the constitutive law they use accounts for softening followed by progressive hardening as in the present work. The influence of the thickness is investigated by Tvergaard and Needleman who observe that for a sufficiently large thickness (about 6 mm), the plastic zone observed in 3D appears similar to that found for 2D plane strain calculations. A similar result is found in the present work for the shape of the plastic zone: shear bands in the center of the notch specimen are similar to those observed in 2D plane strain calculations. However, large plastic deformation with a cumulated shear strain as large as 0.5(see Figure II-9) induces a noticeable material contraction across the thickness that modifies noticeably the stress constraint and related stress triaxiality. In other words, the 2D plane strain calculations overestimate the magnitude of the mean stress in the material in comparison to that

observed in the 3D calculations. In terms of plastic deformation, 3D plastic fields at the center are similar to those predicted of 2D plain strain calculations, but this is not the case of maximum mean stress distribution. This is observed not only for a thickness *t* as large as 8 mm, but also for 12 mm and 15 mm (*t/R*=32, 48 and 60) for a notch radius *R* = 0.25mm and a ratio *t/R* = 32. Ductile polymers develop large plastic deformation before the nucleation of crazing that cause material's failure. Craze initiation in ductile polymer is usually considered to be governed by a critical mean stress [ISH77, NAR80, ISH83]. From the present study, 3D calculations appear necessary for such estimation. 2D plane strain analysis based on Hill's slip line analysis [ISH77] or modified slip lines with accounting of the pressure dependent threshold [NAR80, ISH83] and also calculations with a more realistic constitutive law [LAI97] have to be considered carefully when one tries to derive quantitative estimates of the critical mean stress for craze initiation. The use of an a priori thick sample (10 or 14mm in [NAR80, ISH83] and even 50mm in [GEA04]) does not ensure plane strain conditions. The ratio between the thickness and the notch radius needs to be considered. Plane strain conditions are not met in terms of stress distribution for a ratio *t/R* as large as 32 (8mm thick with 0.25 notch radius). A recent investigation on the influence of the thickness in the competition in fracture between ductile tearing or 'brittle' failure by crazing by Kattekola et al. [KAT13] suggest that for a ratio *t/R* larger than 25 plane strain conditions are ensured, which is not observed in the present study. In the present work, we observe that the mean stress distribution derived from 2D plane strain calculations is larger than that observed for 3D calculations for *t/R*=25 or even larger ratio for *t/R* up to 60 (see Figure II-12 where the case with *t/R*=60 is also reported). What is also observed is the variation of the maximum mean stress that become independent on the thickness for *t/R* larger than 48. In Figure II-14, the variation of the maximum mean stress for *t/R*= 48 and 60 is identical, but noticeably smaller than that predicted in the 2D plain strain simulation. Thus, the magnitude of the stress distribution reaches an asymptotic value and a similar estimation of the mean stress is expected for larger thickness, but the 3D calculations are not equivalent to 2D plain strain conditions for samples as thick as 15 mm.

A dependence on the stress distribution with the material's thickness is more commonly observed in the fracture of thin samples, and in particular in polymer films. In the present study, the plastic zone

for the thinnest samples corresponding to t/R = 1 is qualitatively similar to observations on thin film [COR07] consisting in a flame like distribution of the plastic deformation with the maximum strain localized along the notch symmetry plane in the middle of the thickness. A transition from t/R = 1 to t/R = 4, from sample 0.25 to 1mm thick results in a mean stress increase by 20% for a given load level (see Figure II-14). The definition of a thickness corresponding to plane stress conditions appears difficult and 3D calculations can help in this evaluation. The present 3D description can also serve in estimating the conditions for using the Essential Work of Fracture (for instance [MAI86]) for the estimation of the resistance to fracture of thin polymer samples. The essential work of fracture is generally characterized for a given thickness. This is interpreted here with a dependence on the stress distribution with the stress triaxality that influence the material's viscoplastic response. In particular, the plastic zone at the surface and in the center, although not as different as in the thick sample is distinct for thin specimens ($t / R = 1$ or 4) and so is the stress distribution.

II.6. Conclusion

The main results are now summarized. 2D and extensive 3D calculations have been carried out to investigate the influence of the thickness of ductile polymers in the stress distribution. An initial blunt notch with radius equal to 0.25mm is considered (reference case) and a smaller one of 0.1mm and larger of 0.5mm are investigated too. The ratio between the thickness t and the notch radius R is found suitable to qualify the results. For thin specimens ($t / R \leq 4$), a flame like plastic zone is predicted with little but no negligible difference of its profile at the surface and in the center of the specimen. For a geometry with $t / R > 4$, a clear difference is observed between the plastic deformation at the surface and in the center: the magnitude of the cumulated plastic shear strain is larger at the center of the thickness. The deformation proceeds by strain localization in the form of shear bands for a polymer like response with softening upon yielding followed by progressive hardening. For thick samples, the plastic zone observed at the center of the thickness is qualitatively similar to that predicted with a 2D plane strain simulation.

Difference between 2D plane strain conditions and full 3D calculations are evidenced in the magnitude of the stress distribution. The development of the plastic zone causes a shift in the location of the maximum mean stress ahead of the notch tip. The maximum mean stress for a given load level increases with the thickness. It rapidly reaches a plateau for the thinner samples while it progressively increases with loading for the larger thickness. The variation of the maximum mean stress is observed to become thickness independent for a ratio thickness over notch radius ($t / R \geq 48$) corresponding to a 12mm thick or larger with a notch radius of 0.25mm. However, the magnitude of the maximum mean stress estimated from the 3D calculations is noticeably smaller than that found from 2D plane strain calculations. This has an important implication in the evaluation of the critical mean stress for craze initiation in ductile polymers. 3D calculations are necessary for its evaluation.

References For Chapter II

[ABA10] Abaqus, version 6.10-2, simulia, Dassault systems.

[ARG73] Argon AS. A theory for the low-temperature plastic deformation of glassy polymers. Phil. Mag. 1973, 28, pp. 839–865

[ARR93] Arruda EM, Boyce MC. A three-dimensional constitutive model for large stretch behaviour of rubber elastic materials. J. Mech. Phys. Solids, 1993, 41, pp. 389–412

[BAS02] Basu S, Van der Giessen E. A thermo-mechanical study of mode I, small-scale yielding crack-tip fields in glassy polymers. Int. J. Plast. 2002, 18, pp. 1395–1423

[BOY88] Boyce MC, Parks DM, Argon AS. Large inelastic deformation of glassy polymers. I. Rate dependent constitutive model. Mech. Mater. 1988, 7, pp. 15–33

[COR07] P.-P. Cortet, L. Vanel and S. Ciliberto, 2007, Dynamical Law for Slow Crack Growth in Polycarbonate Films, Phys Rev Lett, 99, 205502

[COR08] P.-P. Cortet, L. Vanel and S. Ciliberto, 2008, Surface oscillations and slow crack growth controlled by creep, Eur. Phys. J. E 27:185–195

[GEA04] B.P. Gearing, L. Anand. Notch-sensitive fracture of polycarbonate, Int J Solids and Structures. 2004, 41:827–845.

[HAS00] S. Hashemi, and J.G. Williams. Temperature dependence of essential and non-essential work of fracture parameters for polycarbonate film. Plastics, Rubber and Composites. 2000, 29:294–302

[HIL50] HIL50: R. Hill, 1950, The mathematical theory of plasticity, reprinted in 1998 by Oxford classic series, London.

[ISH77] M. Ishikawa, I. Narisawa, H. Ogawa. Criterion for craze nucleation in polycarbonate. J. Polym. Sci. 1977, 15, pp. 1791–1804

[ISH83] Ishikawa M , Narisawa I. The effect of heat treatment on plane strain fracture of glassy polymers. Journal of Materials Science. 1983, 18, pp 2826-2834

[KAT13] Brunda Kattekola, Abhishek Ranjan, Sumit Basu. Three dimensional finite element investigations into the effects of thickness and notch radius on the fracture toughness of polycarbonate. Int Journal of Fracture. 2013, 181:1–12

[KWE13] S. Kweon, A.A. Benzerga. On the localization of plastic flow in glassy polymers. European Journal of Mechanics A/Solids. 2013, 39: 251–267

[LAI97] J.Lai, E.Van der Giessen. A numerical study of crack-tip fields in glassy polymers. Mechanics of Materials. 1997, 25:183–197.

[LU99] J. Lu and K. Ravi-Chandar. Inelastic deformation and localization in polycarbonate under tension. International Journal of Solids and Structures. 1999, 36, 391–425.

[MAI86] Y-W MAi and B. Cotterell. On the essential work of ductile fracture in polymers. Int Journal

Fracture. 1986, 32:105–125.

[NAR80] I. Narisawa, M. Ishikawa, H. Ogawa. Notch brittleness of ductile glassy polymers under plane strain. J. Mat. Sci. 1980, 15:2059–2065.

[SAA06] N Saad-Gouider, R. Estevez, C Olagnon, R. Séguéla. Calibration of a viscoplastic cohesive zone for crazing in PMMA. Eng. Fract. Mech. 2006, 2503–2522.

[TVE08] Tvergaard V., Needleman A. An analysis of thickness effects in the Izod test. Int. J. Solids Struct. 2008, 45:3951–3966

[Wu93] Wu, P.D., Van der Giessen, E. On improved network models for rubber elasticity and their applications to orientation hardening in glassypolymers. J. Mech. Phys.Solids.1993, 41:427.

[Wu96] Wu, P.D., Van der Giessen, E. Computational aspects of localized deformations in amorphous glassy polymers. Eur. J. Mech. A. 1996, 15:799–823.

3D STUDY OF DUCTILE POLYMER FRACTURE

Failure characteristics and toughness at the initiation of crack nucleation are investigated. Polycarbonate is taken as representative of a ductile glassy polymer at room temperature, but also because of its commercial importance in structural application. Its fracture toughness is known to be dependent on a number of factors including the molecular weight, the processing, including ageing time, loading rate and specimen geometry. In this chapter, the influence of the specimen geometry is investigated and in particular that of the material's thickness, which is the only varied parameter. A realistic constitutive law for the bulk with softening upon yielding followed by hardening at continued deformation is used. Failure by crazing is considered and described with a cohesive model. A transition in the failure mode from ductile tearing to fracture by crazing is observed with increasing thickness. Ductile tearing is likely to be captured for a critical plastic stretch and crazing, even if incorporated in the description, does not develop for thin samples. When the thickness increases, crazing ensures some load bearing capacity that results in a noticeable difference in the load level for which craze initiation is observed with respect to the nucleation of a crack and related onset of crack propagation. The influence of the thickness on the predicted toughness is reported and a condition for the ratio thickness t / notch radius R for a minimum toughness is observed when t/R is larger than 16. The consequence on the appropriate geometry for the estimation of the minimum toughness is discussed.

Table of contents

III. 3D study of ductile polymer fracture III-1
Table of contents III-2
III.1. Introduction III-3
III.2. Constitutive law for glassy polymers III-6
III.2.1. Modelling background III-6
III.2.2. Materials under considerations III-9
III.3. Modelling failure by crazing in glassy polymers III-11
III.3.1. Review of cohesive models for crazing III-11
III.3.2. Simple cohesive surface formulation for crazing in ductile polymers III-13
III.4. Problem formulation III-15
III.4.1. Description of geometry and mesh discretization III-15
III.5. Results III-18
III.5.1. Influence of the thickness on the polymer fracture for the reference parameters for the bulk and the cohesive model III-19
III.5.2. Influence of the maximum traction of debonding T_{max} on the fracture process III-27
III.5.3. Influence of the strain softening on 3D fracture simulations III-36
III.5.4. Influence of cohesive critical opening Δ_{max} III-44
III.6. Discussion and concluding remarks III-47

III.1. Introduction

Failure characteristics and toughness at the initiation of crack nucleation are investigated. Polycarbonate is taken as representative of a ductile glassy polymer at room temperature, but also because of its commercial importance in structural application. Its fracture toughness is known to be dependent on a number of factors including the molecular weight, the processing, including ageing time, loading rate and specimen geometry. In this chapter, the influence of the specimen geometry is investigated and in particular that of the specimen thickness, which is the only varied parameter. For thick specimen, fracture in glassy polymers depends on the competition between shear yielding and crazing, which are two rate dependent plastic mechanisms, although at different length scales. Shear yielding corresponds to strain localization in the form of shear bands related to the bulk constitutive law with softening upon yielding followed by hardening at continued deformation. Crazing involves also some plasticity but at a different scale. A rate dependent description of these two mechanisms is accounted for by Estevez et al. [EST00] who showed that the ductile to brittle transition with increasing loading rate can be captured and is related to a reduction in the bulk plasticity prior to failure. Their analysis is performed under the assumption of 2D plane strain conditions which imply an infinitely large thickness. The influence of the specimen thickness is investigated here for a given polycarbonate in terms of molecular weight, processing and ageing time. A unique geometry corresponding to a single edge notch specimen (SENT) subjected to uniaxial tension is considered with a blunt notch R of 0.25mm. A blunt notch is accounted for as sharp cracks are difficult to machine in PC. It allows for a well defined geometry. The thickness t is varied from t/R =1 to 16, larger ratios are considered in some cases. Evidences of the influence of the thickness on the fracture toughness are found in Parvin and Williams [PAR75], Fraser and Ward [FRA77] for instance, while Nisitani and Hyakutake [NIS85] investigated the influence of the notch radius. In the present study, and following the results reported in chapter 2, we consider that the ratio t/R is more suitable for characterizing the 3D effects.

The ductile to brittle transition in ductile polymers is not only related to loading rate effects governed by the time scales between the test rate and those involved in shear yielding and crazing. For a given test condition in terms of loading rate, increasing the thickness from thin or film samples to thick specimens results in two fracture modes: from ductile tearing in the case of polymer films and thin samples to failure by crazing for thicker ones [PAR75]. For thin samples, a flame like plastic zone is observed ahead the notch tip [COR07, HAS00] and failure takes place by ductile tearing for a critical cumulated plasticity [GEA04]. For thick samples, the shape of the plastic zone is similar to slip lines predicted by HILL [HIL50] with localization of the plastic deformation in the form of shear bands [LAI97]. In ductile polymers, failure by crazing is generally preceded by the development of this latter type of plastic zone with the initiation of crazing at the tip of the plastically deformed region [ISH77, NAR80]. In the literature, a criterion for the onset of failure is associated with the initiation of crazing [LAI97, GEA04, BAS02, KAT13] and a single critical mean stress is considered. The estimation of the critical stress state for craze initiation is derived from 2D plane strain calculations [ISH77, NAR80]. A value ranging in 70-90 MPa is found. As reported in chapter 2, the estimation of the critical stress state for the nucleation of crazing requires a 3D analysis as the stress distribution around the notch is noticeably thickness dependent so that a condition derived from 2D plain strain calculation is certainly an approximation. The appropriate criterion for craze initiation remains an open question in the polymer community as illustrated in the numerous expression found in the literature [STE73, OXB73, ARG77, ISH77, SAA06, BUCK07, EST11] based on experimental observations, continuum models or molecular dynamics calculations: criteria based on a critical mean stress or combining the shear and mean stress or simply the maximum principle stress are found.

Craze thickening ensures some load carrying capacity so that failure corresponding to craze fibrils breakdown takes place for a load level larger than that for craze initiation. The description of the mechanism underlying failure, even in a simplistic form appears more suitable to estimate the fracture toughness.

The objective of this chapter is to gain insight for the estimation on whether plane stress and/or plane strain conditions are dominant or mixed in the characterization of glassy polymer fracture, under

quasi-static conditions. A numerical study is carried out with implementation of Boyce et al. constitutive law [BOY88] in the version modified by Wu and Van der Giessen [Wu96] through a UMAT routine in Abaqus [ABA10]. The Single Edge Notched Tension (SENT) configuration is considered with a given dimension regarding the length, width and crack length. A configuration with a blunt notch specimen is preferred than that with a natural crack as experimentally machining a natural crack is difficult in ductile polymers while preparing a blunted one is tractable. 3D effect on glassy polymer fracture have been investigated recently by Gearing and Anand [GEA04] and Kattekola et al. [KAT13] for a given thickness [GEA04] and variable thickness [KAT13]. In these studies, failure is considered when a continuum criterion is met first: a critical plastic stretch or a critical mean stress, depending on the stress triaxiality of the test [GEA04] or on the specimen thickness [KAT13]. In the present study, in addition of accounting for a realistic constitutive law for glassy polymers, a simple cohesive model is used to mimic crazing mechanically with a traction separation law of which maximum traction and critical opening are representative for crazing. The influence of the specimen thickness on the fracture toughness is investigated first for a set of reference material parameters, representative of polycarbonate for the bulk. A parametric study is conducted to analyse the influence of the maximum traction. The analysis is compared with an examination of the influence of the maximum opening corresponding to craze fibrils breakdown, and ultimately the influence of the bulk material and in particular that of its strain softening is explored.

The chapter is organized as follows: the governing equations for the bulk constitutive law is presented and then the cohesive model for crazing. The problem formulation and the results are presented. The chapter ends with a discussion and conclusive remarks.

III.2. Constitutive law for glassy polymers

III.2.1. **Modelling background**

In the absence of crazing, glassy polymers can undergo a deformation up to 100% with an intriguing constitutive law with softening upon yielding followed by hardening. In an analysis of the crack tip plasticity under a mode I loading, Lai and Van der Giessen [LAI97] have shown that the observed softening is intrinsic to the material response and is not due to a structure or geometrical effect. Their prediction of the shape of the plastic zone and trajectories of the shear bands is in good agreement with reported observations of Ishikawa et al. [ISH77]. The constitutive law used to model the large strain plasticity is based on original ideas due to Boyce et al. [BOY88] but with some modifications introduced later by Wu and Van der Giessen [WU93] for the hardening part. We present the governing equations to point out the parameters to be identified. The constitutive equations presented here have been implemented in a UMAT subroutine in Abaqus [ABA10] following the [WU96] for the computational aspects.

The mechanics of fully three-dimensional large strain deformation involves the deformation gradient tensor $\boldsymbol{F}$, which maps a material point of the reference configuration into the current configuration. The deformation gradient is multiplicatively decomposed as $\boldsymbol{F} = \boldsymbol{F}^e \boldsymbol{F}^p$, with $\boldsymbol{F}^p$ a deformation from the initial to an intermediate, "relaxed" or "natural" configuration, followed by an elastic transformation $\boldsymbol{F}^e$ up to the final deformation $\boldsymbol{F}$. The velocity gradient in the current configuration is $\boldsymbol{L} = \dot{\boldsymbol{F}}\boldsymbol{F}^{-1} = \dot{\boldsymbol{F}}^e \boldsymbol{F}^{-e} + \boldsymbol{F}^e \dot{\boldsymbol{F}}^p \boldsymbol{F}^{-p} \boldsymbol{F}^{-e}$ of which symmetric and anti-symmetric part correspond to the strain and spin tensor respectively. When the elastic part $\boldsymbol{F}^e$ of the deformation gradient is small compared to the plastic one $\boldsymbol{F}^p$ (i.e. $\boldsymbol{F}^e \approx \boldsymbol{I}$), the velocity gradient results in $\boldsymbol{L} \approx \boldsymbol{L}^e + \boldsymbol{L}^p$ so that the total strain rate $\boldsymbol{D}$ becomes the sum of the elastic and plastic parts as $\boldsymbol{D} = \boldsymbol{D}^e + \boldsymbol{D}^p$. Prior to the yield stress, most amorphous polymers show a non linear stress-strain response due to small viscoelastic effects. These are not considered explicitly but their effect on the mechanical response is accounted for by using a secant Young modulus instead of that derived from ultra-sonic measurements of the elastic wave velocities. Its value is estimated from unixial compression tests and an average value for different strain rates of $E^{secant}=\sigma_y/\varepsilon_y$, with σ_y the yield stress and ε_y the corresponding yield strain, is

used. In view of these approximations, the hypo-elastic law is used to express the bulk mechanical response as

$$\overset{\nabla}{\boldsymbol{\sigma}} = \boldsymbol{\mathcal{L}}_e \boldsymbol{D}^e = \boldsymbol{\mathcal{L}}_e (\boldsymbol{D} - \boldsymbol{D}^P) \tag{1}$$

where $\overset{\nabla}{\boldsymbol{\sigma}}$ is the Jaumann rate of the Cauchy stress, $\boldsymbol{\mathcal{L}}_e$ the fourth-order isotropic elastic tensor in terms of secant Young modulus E^{secant} and Poisson's ratio ν, which is in Cartesian components

$$\mathcal{L}_{ijkl} = \frac{E^{\text{secant}}}{2(1+\nu)}\left[\left(\delta_{ik}\delta_{jl} + \delta_{il}\delta_{jk}\right) + \frac{2\nu}{1-2\nu}\delta_{ij}\delta_{kl}\right].$$

Within the elastic-viscoplastic framework used here, the plastic strain rate $\boldsymbol{D}^P$ is

$$\boldsymbol{D}^P = \dot{\gamma}^P \frac{\overline{\boldsymbol{\sigma}}'}{\sqrt{2}\tau}, \tag{2}$$

with $\dot{\gamma}^P(\tau, p, T)$ the equivalent shear strain rate which is temperature and stress dependent, and $\tau = \sqrt{\overline{\sigma}' : \overline{\sigma}' / 2}$ the equivalent shear stress. In Eq. 2, the tensor $\overline{\boldsymbol{\sigma}}'$ corresponds to the deviatoric part of the driving or effective stress which is the difference between the applied Cauchy stress $\boldsymbol{\sigma}$ and a back stress $\boldsymbol{b}$ as $\overline{\boldsymbol{\sigma}} = \boldsymbol{\sigma} - \boldsymbol{b}$. The back stress tensor $\boldsymbol{b}$ is due to the entropic back forces generated by the deformation of the polymer chains during the plastic deformation, and will be defined later on. The equivalent plastic shear strain rate $\dot{\gamma}^P$ is taken according to Argon's original idea [ARG73]

$$\dot{\gamma}^P = \dot{\gamma}^0 \exp\left[-\frac{A(s_0 + \alpha p)}{T}\left(1 - \left(\frac{\tau}{s_0 + \alpha p}\right)^{5/6}\right)\right], \tag{3}$$

in which A and $\dot{\gamma}^0$ are material parameters and T is the absolute temperature. The athermal shear strength s_0 in Argon's original formulation is $s_0 = \frac{0.077 \times G}{1-\nu}$, with G the shear modulus at high frequency and ν the Poisson ratio. It is worth noting here that the shear modulus G involved in (3) is *not* connected to the the secant Young modulus E^{secant} used in the bulk constitutive law (1). The first determines the activation energy responsible for plasticity locally while the E^{secant} is thought to represent the influence of viscoelastic effects on the bulk mechanical response. This choice for the value of G from ultrasonic measurements appears more consistent than an estimate from a tensile or

compression tests for which the value derived is dependent on the prescribed strain rate or stress level at which the measurement is performed. The coefficient α represents the pressure sensitivity of the polymer which results in an asymmetric yield stress in tension and compression, for instance.

From a micromechanical point of view, the expression of the temperature and rate dependency of Eq. 3 is general enough to describe the variation of the yield stress of glassy polymers due to viscoplasticity and we adopt this expression even if the physical arguments underlying Argon's view do not receive full agreement in the polymer community.

Following Boyce et al. [BOY88], intrinsic softening is accounted for with the definition of an internal variable s which varies from s_0 to s_{ss} at continued plastic deformation. The internal law $\dot{s} = h\left(1 - s / s_{ss}\right)\dot{\gamma}^P$ governs its variation during deformation, with h a parameter controlling the rate of softening and s_{ss} the value of s in a steady state regime.

The progressive hardening due to the plastic deformation and induced molecular orientation results in a back stress tensor $\boldsymbol{b}$ which can be considered as the development of internal stresses during the deformation. Its description is based on ideas borrowed from theories for rubber elasticity with the cross-links of the rubbers considered as "entanglements" in the case of glassy polymers [BOY88, Wu93]. The deformation of the resulting network is assumed to derive from the cumulated plastic stretch [Wu93] so that the principal back stress components b_α are functions of the principal plastic stretches λ_β as

$$\boldsymbol{b} = \sum_\alpha b_\alpha \left(\boldsymbol{e}_\alpha^p \otimes \boldsymbol{e}_\alpha^p\right),\ b_\alpha = b_\alpha\left(\lambda_\beta\right), \tag{4}$$

in which $\boldsymbol{e}_\alpha^p$ are the principal directions of the plastic stretch. The estimate of the back stress $\boldsymbol{b}$ used in our description is due to Wu and Van der Giessen [Wu93] on the basis of their analysis of the fully three-dimensional orientation distribution of molecular chains in a non-Gaussian network. Wu and Van der Giessen have shown that a fairly good estimate of the back stress tensor $\boldsymbol{b}$ can be obtained with the following combination of the three-chains and eight-chains [ARR93] models as

$$b_\alpha^{n-ch} = (1-\rho) b_\alpha^{3-ch} + \rho b_\alpha^{8-ch}, \tag{5}$$

with $\rho = 0.85\,\bar{\lambda}/\sqrt{N}$, $\bar{\lambda} = \max(\lambda_1, \lambda_2, \lambda_3)$ the maximum plastic stretch and N the average number of segments between entanglements. The limit stretch of a molecular chain is $\lambda_{\max} = \sqrt{N}$. The expressions for the principal components of b_α^{3-ch} and b_α^{8-ch} contain an additional parameter: the shear modulus C^R of the network taken as $C^R = nk_BT$, n being the entanglement density, k_B the Boltzmann constant and T the temperature.

The above constitutive model has been implemented in a user-define UMAT subroutine in Abaqus [ABA10] 'standard'. Quasi-static calculations are carried out. The time integration scheme and related tangent stiffness matrix presented in [Wu96] are used and implemented in the UMAT. The back stress (Eq. 5) is calculated from the current value of the plastic strain tensor. The related non linear constitutive equations (1-5) are solved with an iterative Newton Raphson procedure.

III.2.2. **Materials under considerations**

A set of two bulk parameters representative of polycarbonate is used and named 'Mat-A' and 'Mat-B'. The material B has a larger strain softening than 'Mat-A'. Their response for uniaxial compression at a constant strain rate $\dot{\varepsilon}_0 = 1\times10^{-3}/\text{s}$ is presented in Figure III-1. The corresponding parameters are presented in Table III-1. The two materials under considerations differ only by the ratio between the steady state yield strength s_{ss} with respect to the initial one s_0. The temperature is T=293K and a value of the shear strength s_0=88MPa is used. The notch tip plasticity for a Single Edge Notch Tension (SENT) is examined next for two dimensional (2D) plane strain conditions and in three dimension (3D) calculations. Crazing is modelled with a cohesive surface described in the next section. The competition between bulk plastic deformation by shear yielding and crazing is examined for a variable thickness.

	E/s_0	ν	α	As_0/T	$\dot{\gamma}_0(/s)$	s_{ss}/s_0	h/s_0	C^R/s_0	N
Mat A	14.7	0.39	0.08	649.	9.2×10^{-9}	0.77	5.1	0.19	3
Mat B	14.7	0.39	0.08	649.	9.2×10^{-9}	0.66	5.1	0.19	3

Table III-1 : Bulk parameters for the materials under consideration, for the reference material A, and for material B exhibiting a larger strain softening than material A, the yield strength s_0=88MPa.

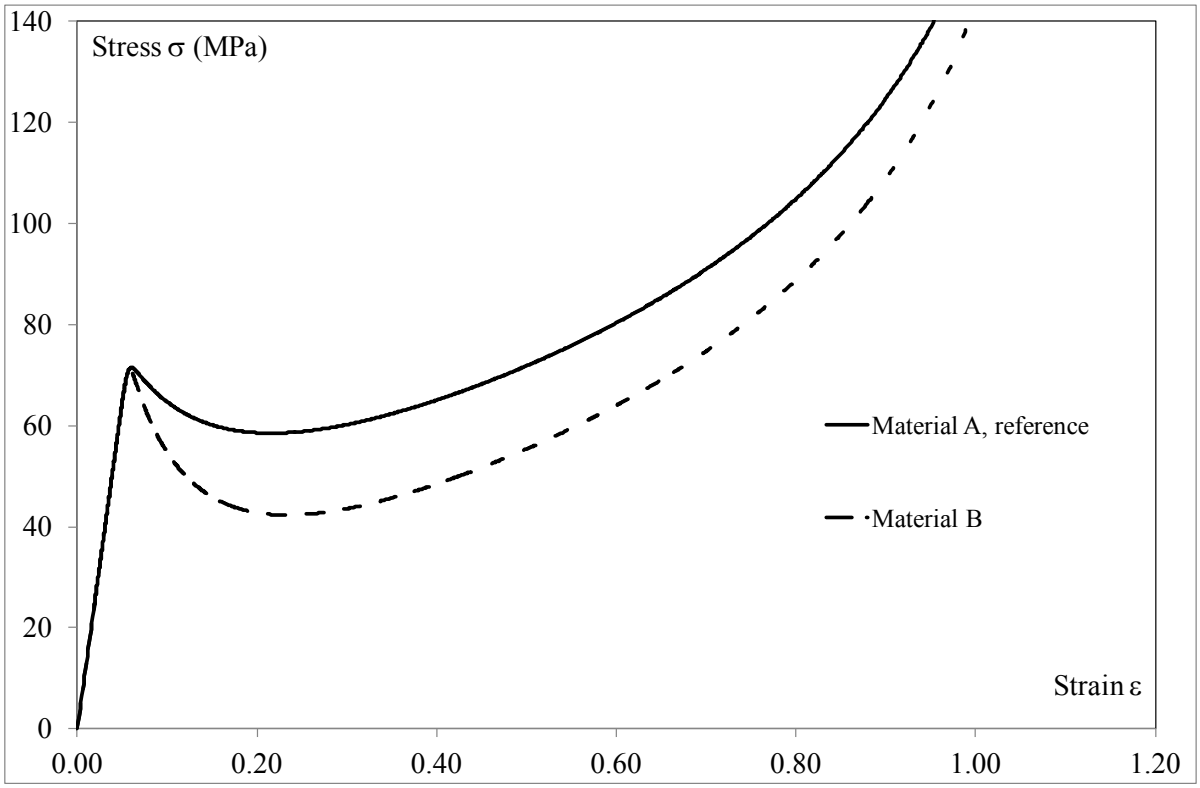

Figure III-1**:** Stress – Strain response of the materials under consideration for uniaxial compression at strain rate $\dot{\varepsilon} = 1\times10^{-3}$/s for the reference material A, and for material B exhibiting a larger strain softening.

III.3. Modelling failure by crazing in glassy polymers

In this section, a review of available cohesive models for crazing reported in the literature is presented. The motivation for adopting a simplified version is presented and the adopted model, available in Abaqus [ABA10] is presented. The characteristic parameters of the cohesive model, the maximum traction at the onset of debonding T_{max} and the critical opening corresponding to the nucleation of a crack locally Δ_{max} are chosen chosen based on this review: T_{max} is of the order of 100MPa while Δ_{max} is of some microns so that the energy of separation $\Gamma_0 \sim T_{max} \times \Delta_{max}$.

III.3.1. Review of cohesive models for crazing

Pioneer investigations on crazing and the related shape of the plastic zone are due to Döll [DOL83, DOL90]. The successful comparison between the shape of the craze profile measured by optical interferometry and the predictions derived from the Dugdale model [DUG60] (see Figure III-2a) have made very popular the use of this description for crazing. From later investigations by Kramer and co-workers [KRA83, KRA90], craze thickening is shown to originate in a draw-in mechanism across the craze surface from the bulk into a web of craze fibrils, which implies localised plasticity at the craze bulk interface. By borrowing these ideas, Tijssens et al. [TIJ00, EST00] proposed a rate dependent cohesive model (see Figure III-2b) that results in a rate dependent Dugdale description with the magnitude craze stress governed by the local rate displacement fields. This formulation results in a rate dependent work of separation that corresponds to the energy release rate in the absence of plasticity. This formulation has been experimentally verified for quasi-static conditions by Saad-Gouider et al. [SAA06] for PMMA, the fracture in PMMA being not preceded by bulk plasticity. However, other descriptions in the literature suggest different traction-opening profiles for the cohesive surface formulation of failure in fracture tests, usually under dynamic loadings. Murphy and Ivankovic [MUR05, MUR06] (see Figure III-2c) propose a decaying traction upon onset of debonding followed by a plateau from the comparison between the crack patterns in dynamic fracture tests and predictions of their calculations. In a thermomechanical comparison between the temperature measurements of a running crack in PMMA and predictions with accounting for crazing as heat source from the plastic dissipation of the work of separation, Bjerke and Lambros [BJE03]

compared their experimental thermal data with the temperature fields derived for thermomechanical simulations of their fracture tests. They compared different traction-opening profile and observed that the best fit is found when a decaying traction-opening response is considered (see Figure III-2d) , the decays being linear or non linear. The physically motivated description of crazing within a cohesive surface formulation of Tijssens et al. [TIJ00, EST00], corresponding to a rate dependent Dugdale model, is found consistent with experimental data but other description derived from dynamic tests have also to be considered. Thus, there is no general agreement on the formulation of the cohesive model for crazing in the literature, essentially because an un- direct identification of the traction-opening profile is performed. However, recently, Réthoré and Estevez [RET13] proposed a methodology for the identification of the traction-opening profile from the displacement fields around a crack subjected to a mode I loading and failure by crazing. The identified traction-opening relationship is in intermediate between a plateau with a constant craze stress and a decay of the traction from the value at the onset of debonding down to zero when the critical opening Δ_{max} is attained. The foregoing proposed cohesive models for crazing considered the case of PMMA. The experimental results reported by Döll [DOL83, DOL90] and the detailed investigation of Saad-Gouider et al. [SAA06] suggest that a rate dependent formulation is necessary in the case of PMMA to capture the rate dependent toughness evidenced experimentally. The traction-separation profile is likely to resemble a Dugdale like reponse, with some decay in the traction-opening relationship [RET13]. However, no cohesive model for crazing in polycarbonate is available, as a direct identification in the spirit of Réthoré and Estevez [RET13] is not straightforward when crazing and failure is preceded by large plastic deformation in the bulk. In addition, Tvergaard and Hutchinson [TVE92] observed that the shape of the traction-opening profile is of little importance when failure is preceded by plasticity in the bulk. Based on this observation, and the cohesive model for crazing in polycarbonate remaining to be identified, we adopt a simple cohesive surface formulation available in abaqus [ABA10] that corresponds schematically to that presented in Figure III-1d. The approach is phenomenological but simple and gets along with two parameters: the maximum traction at the onset of debonding T_{max} and the critical opening Δ_{max} that corresponds to the nucleation of a crack locally. However, T_{max} and Δ_{max} have a physical meaning. The critical opening Δ_{max} has been measured

experimentally by Döll et co-workers by optical interferometry, although at temperature smaller than room temperature. Its magnitude varies from 3 to 10 microns. The maximum traction T_{max} corresponds to the onset of craze thickening and is estimated to be around 100 MPa [DOL83, DOL90].

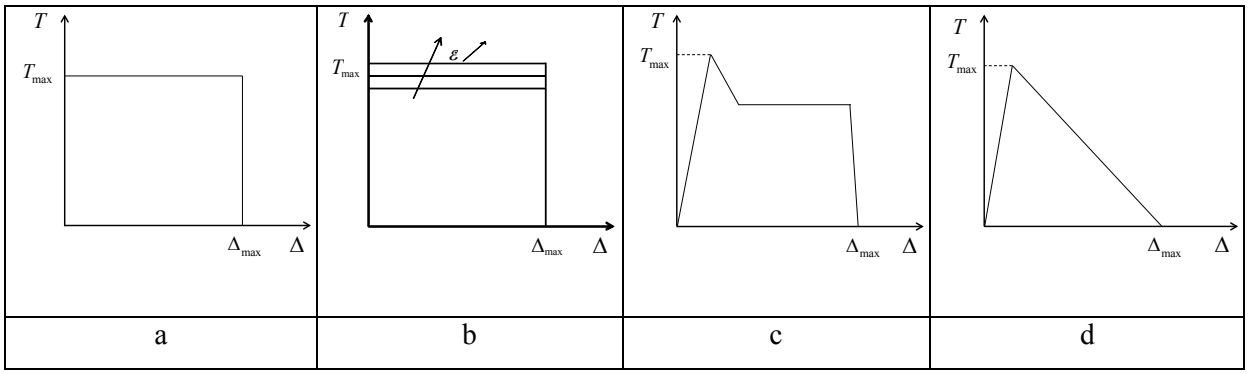

Figure III-2 : Schematic description of the traction-opening profile for cohesive models used for the description of failure by crazing in glassy polymers: (a) Dugdale model [DUG60], (b) Tijssens et al. [TIJ00, EST00], (c) Murphy et al. [MUR05, MUR06], (d) Bjerke and Lambros [BJE03]

III.3.2. Simple cohesive surface formulation for crazing in ductile polymers

The cohesive model depicted schematically in Figure III-2d is adopted to mimic failure by crazing in polycarbonate. The formulation implemented in abaqus [ABA10] is derived from damage mechanics with the definition of a damage variable D that varies from zero for the safe cohesive surface to one at the onset of crack propagation. The description accounts for an initial thickness which serves in defined a relative opening instead of a direct evaluation of the displacement jump across the surfaces. A cohesive surface mid-plane defines the tractions along its normal and the tangential directions. The traction vectors T_n, T_t and T_s are thus connected to the opening Δ_n, Δ_t and Δ_s through the strain like variables $\varepsilon_n = \Delta_n / t_0, \varepsilon_t = \Delta_t / t_0$ and $\varepsilon_s = \Delta_s / t_0$. At continued opening, the damage variable evolved as

$$D = \frac{\Delta_{\max}\left(\max(\Delta_m) - \Delta_m^0\right)}{\max(\delta_m)\left(\Delta_{\max} - \Delta_m^0\right)} \quad \text{with} \quad \Delta_m = \sqrt{\langle \Delta_n \rangle^2 + \Delta_t^2 + \Delta_s^2}\,, \tag{6}$$

with max(□m) the current maximum opening along the direction n, t or s. In the present formulation, no mode mixity between the direction n, t and s is considered and an identical initial stiffness is taken for each contribution. Under the mode I loading under investigation, the opening is along the normal direction of the cohesive surfaces so that the traction is governed by

$$T_n = (1 - D) K_0 \Delta_n\,, \tag{7}$$

where the initial stiffness K_0 is taken as $K_0 = T\max/\Delta_{\max}\times 100$ to ensure the continuity of the displacement fields prior to the onset of debonding when $T_{\max}$ is reached. The damage D is governed by Eq. 6. Account for a debonding through a cohesive model can induce some convergence problems when a quasi-static formulation is used, as discussed by Gao and Bower [GAO04]. The solution used in abaqus is different to that proposed by Gao and Bower. A time dependent damage variable D_v is used instead of D in (7) that is governed by

$$\dot{D}_v = \frac{1}{\mu}\left(D - D_v\right), \tag{8}$$

where D is the current damage estimated from (6), and μ a viscosity that prevent snap-back problems during debonding. In the present work, the viscosity is set to 1×10^{-4}s. An appropriate maximum time step δt needs to be selected carefully and practically the maximum time increment δt is set to 1×10^{-5}s.

Whithin this cohesive formulation, the energy of separation is $\Gamma_0 = \frac{1}{2} T_{\max} \times \Delta_{\max}$. Two values of the maximum traction are considered for a critical opening $\Delta_{\max}$. These are reported in Table III-2. The critical opening of three microns is taken from Döll observations [DOL83, DOL90]. In polycarbonate, the critical opening is observed to be noticeably molecular weight dependent and the value of 3 microns appears to be a lower bound for its magnitude according to the results reported by Döll [DOL83] but is found appropriate to save computation time with no loss of generality. The maximum traction is taken equal to 100-120MPa, that will be shown to correspond to a mean stress at craze initiation of the order of 70-100MPa as found in the literature [ISH77, NAR80, GEA04]

Cohesive parameters	$T_{\max}$ (MPa)	$D_{\max}$ (microns)
CZ-REF	100	3
CZ-B	120	3
CZ-C	120	6

Table III-2 : Cohesive parameters considered in the study.

III.4. Problem formulation

In this section, we present the geometry of the specimen under consideration and the mesh used for the finite element analysis.

III.4.1. Description of geometry and mesh discretization

The 2D and 3D SENT specimens have an identical geometry with height h=80 mm, width w=20mm and a crack length a=10mm. The geometry and mesh discretization are presented in Figure III-3. Refined elements are used around the notch to capture accurately the stress-strain fields. In the region remote from the notch area, coarser elements are used. For the bulk, the element type is CPE4 for the 2D plane strain calculations consisting in four nodes quadratic elements. In the 3D calculations, the 3D elements are C3D8 consisting in 8-node bricks. Cohesive surface elements COH3D8 are inserted along the notch symmetry plane. The amount of elements across the thickness is increased with the thickness increasing, their dimension remaining identical. For instance with R=0.25mm and thickness t=1 mm, the mesh comprises of 6 layers of elements through the thickness of the specimen a total number of 48998 bulk elements and 68735 nodes are employed. The smallest bulk element has an edge of 5.5 microns. The extent of the plastic zone can be estimated approximately by $\Lambda^{CZ}\sim E/T_{max}\times\Delta_{max}$ ≈39 microns for the parameters in Table III-1Table III-2. The length of the cohesive elements is set to 10 microns in order to capture the traction-opening with sufficient accuracy. A constant displacement rate $\dot{u}$ =5 mm/s is prescribed on the top surface to mimic a Single Edge Notch Tension for all calculations. An example of a 3D geometry and mesh of thickness t=4mm is presented in Figure III-3. Different mesh densities are used to reduce the total amount of nodes. The larger mesh density is found around the notch. This progressively decays with the distance from the notch. Each part is meshed separately and 'TIE' conditions are prescribed between each part consisting in abaqus in prescribing a continuous displacement. The remote displacement rate is $\dot{u}_0 = 5\,\mathrm{mm/s}$ corresponding to a strain rate $\dot{\varepsilon}_0 = \dot{u}_0 / h = 1.25\times10^{-1}/s$. For such a strain rate, thermal effects are likely to be observed (see for instance [BAS02, EST05, EST08] and a coupled thermomechanical calculations necessary. This has not been considered here as varying the strain rate induces only a variation of the apparent yield stress and a vertical shift in the mechanical response presented in Figure III-1. Thus, the

choice of the prescribed strain rate is somehow arbitrary but we have used the same remote conditions for all calculations. A blunted notch is used that would correspond to the blunting of a sharp crack up to this initial geometry. This is also motivated by experimental issues in which practically machining a sharp notch in ductile polymers like polycarbonate is difficult if not impossible experimentally. The preparation of a blunted notch is preferred for the fracture measurements to be reproducible. The foregoing bulk constitutive law is implemented in a UMAT subroutine in Abaqus 6.10-2 [ABA10] and the cohesive element library available in Abaqus is employed for the description of the failure mechanisms.

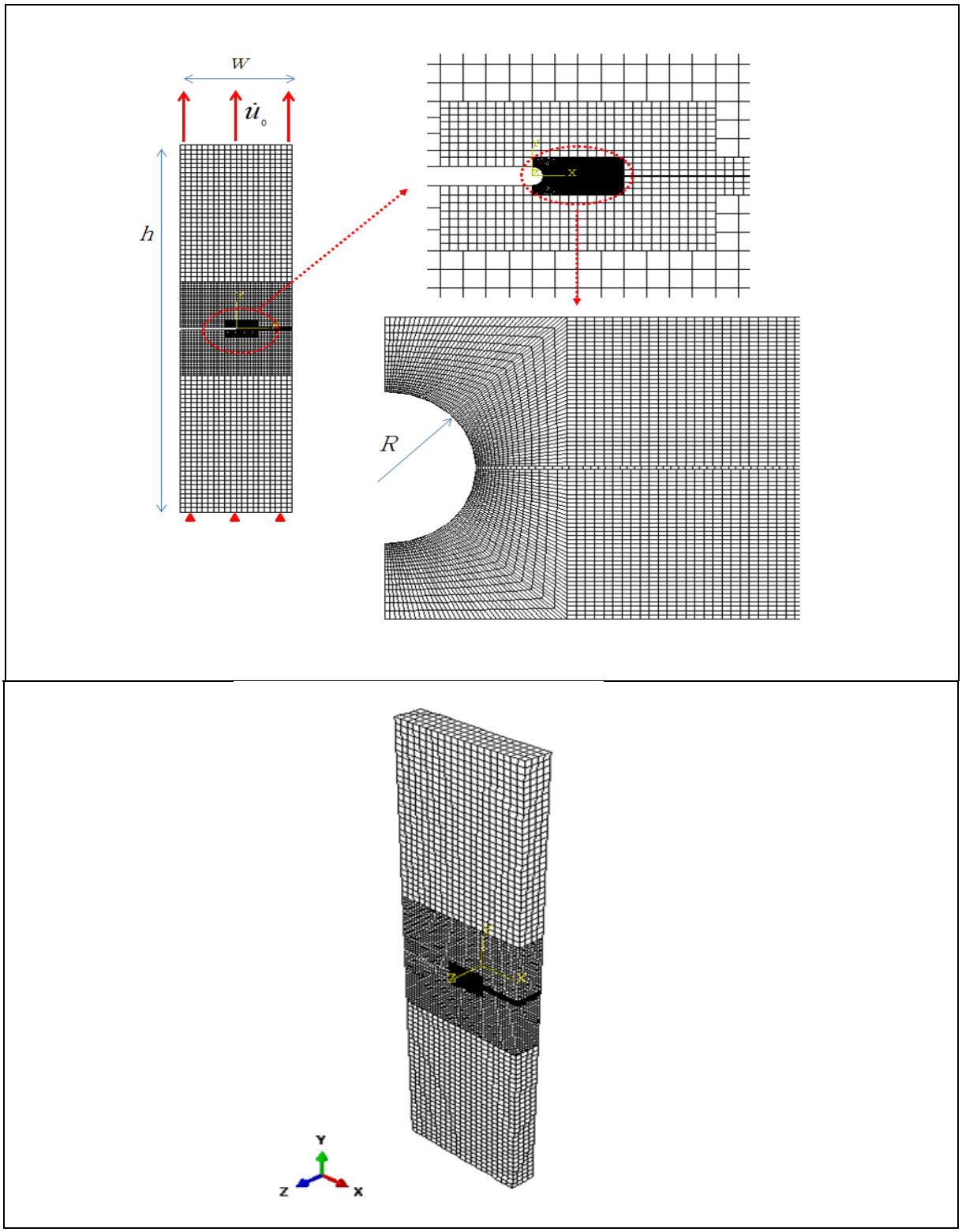

Figure III-3 Description of the mesh used for the 2D plane strain. Cohesive elements are laid down along the notch symmetry plane, where failure is allowed. For the 3D simulations, an extrusion of the above section is performed along the thickness *t*. The total height *h*=80mm, the width is *w*=20mm and the initial notch length is 10mm. The mesh is refined around the notch of which radius is denoted *R*=0.25mm taken as a reference notch radius. The sample is subjected to a uniform displacement rate $\dot{u}_0 = 5\,\text{mm/s}$ corresponding to the strain rate $\dot{\varepsilon}_0 = \dot{u}_0 / h = 6.25\times10^{-2} / s$.

III.5. Results

The condition for craze initiation as found for instance by Ishikawa et al. [ISH77, NAR80] corresponds to the observation reported in Figure III-4 for a polycarbonate sample 10mm thick loaded under tension. The mirror zone corresponds to a well defined surface. From this observation, it is difficult to distinguish if a crack or a craze is observed as the opening is not measurable. However, such observation is generally used to determine the onset of craze initiation. Whether this corresponds to the nucleation of voids of some nanometers [KRA83, KRA90] is questionable. In the present study, we assume the traction –opening depicted in Figure III-2d with the parameters reported in Table III-2 represent crazing with T_{max} the onset of craze thickening up to the critical opening Δ_{max}. In all calculations reported in the sequel, the onset of debonding is reached during the loading. The load-carrying capacity of the cohesive surfaces allows the development of plastic deformation in the bulk at the notch region. We will observe that its magnitude and shape of the plastic zone depend on the sample thickness. We then discuss the interpretation of a craze initiation criterion based on fracture tests observations. The analysis of the predicted toughness with the thickness is also analysed.

We start with the case of the bulk material A (see Table III-1) with the cohesive parameters CZ-REF in Table III-2. The influence of the thickness is investigated. The analysis is followed by an investigation of the influence of the maximum traction T_{max} (CZ-B in Table III-2), that of the bulk softening (Material B in Table III-1) and eventually that of Δ_{max}.

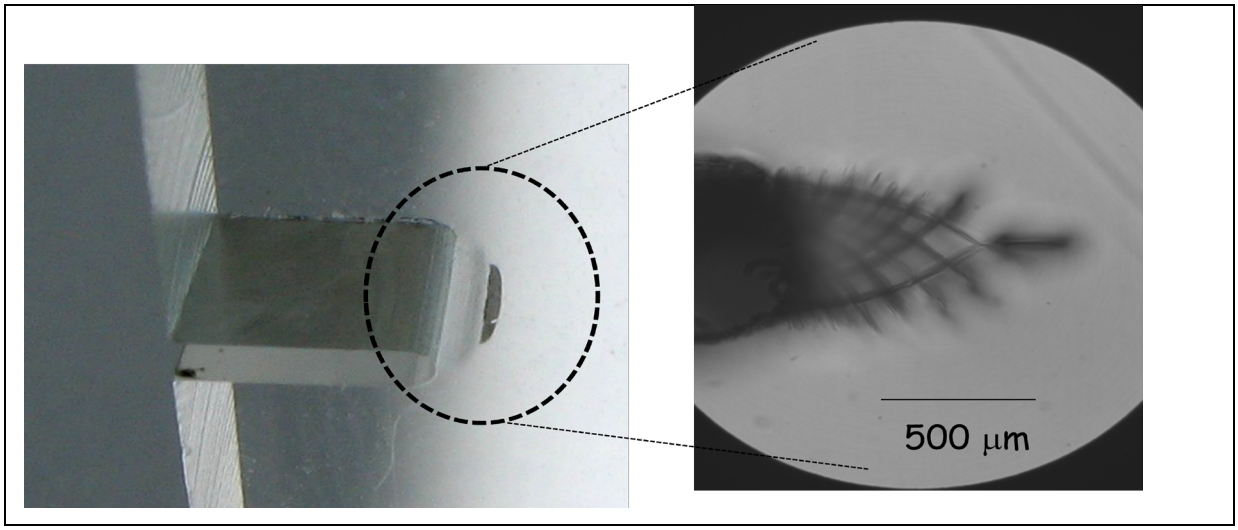

Figure III-4: SENT sample of polycarbonate loaded under tension (geometry identical to that presented in Figure III-3). Observations by transmission plastic zone (opaque zone on the left, slip lines on the right) at the tip of the plastic zone, a stable crack has initiated, where the maximum mean stress is located.

III.5.1. Influence of the thickness on the polymer fracture for the reference parameters for the bulk and the cohesive model

The bulk parameters in Table III-1 for MAT-A and cohesive parameters in Table III-2, CZ-REF are used in the simulations presented in this section. Crazing is allowed in all calculations. Careful examination of the stress distribution at the onset and during cohesive debonding up to the nucleation of a crack is presented. 2D plane strain calculations are presented first followed by 3D simulations for which the thickness is varied from 0.25 to 5mm. The influence of the thickness on the shape of the plastic zone in the presence of crazing is analysed. The related stress component normal to the cohesive surfaces or the mean stress and cumulated plasticity are studied and the predictions of the toughness with varying thicknesses are reported.

III.5.1.1. *2D plane strain simulation of fracture*

The plot in Figure III-5a presents the variation of the macroscopic strain with the loading time. The circle corresponds to the onset of debonding of the cohesive surface. For this load level, the bulk response exhibits a cumulated plastic deformation smaller than 20% of which the contour is not reported. The distribution of the stress component normal to the cohesive surface shows a maximum near the tip (Figure III-5b) where initiation of debonding takes place. At the onset of crack nucleation (Figure III-5c), the location of the crack is ahead the notch tip. The distributions of the cumulated shear strain plasticity (Figure III-5d-e) at the onset of crack nucleation (d) and during crack propagation (e) show that some plastic deformation develops during the cohesive surface debonding. Some shear bands are observed at the onset of crack nucleation and during propagation (Figure III-5d-e). The crack nucleates at the shear bands cross, where the stress concentrates. Crazing noticeably reduces the amount of plasticity able to develop at the notch tip. Once a crack nucleates, it extends at almost a constant macroscopic load level that is used to estimate the material's toughness. The present 2D plane strain analysis will be compared to the finite geometry accounted for in the 3D calculations.

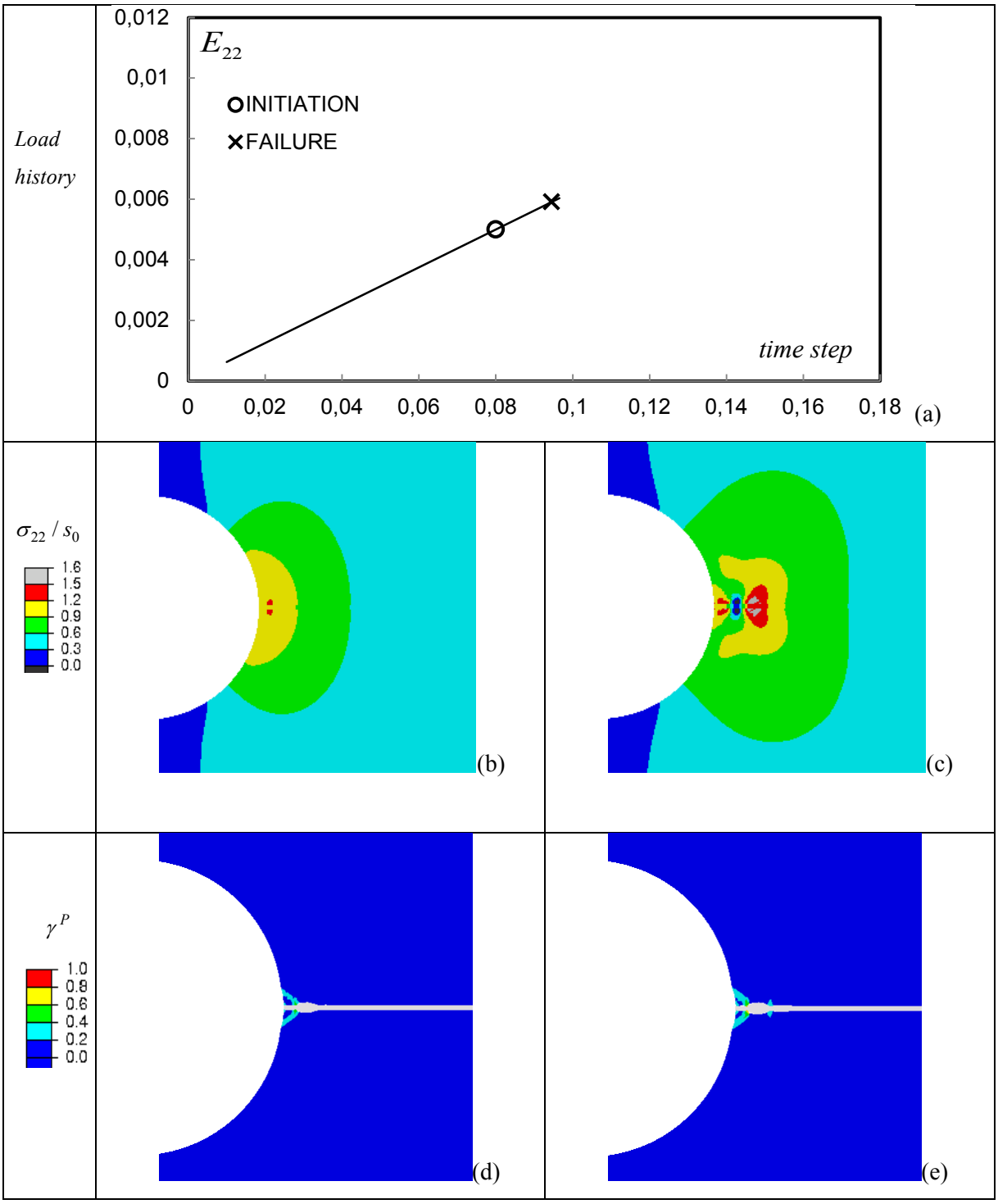

Figure III-5 : 2D plane strain calculations for T_{max}=100MPa: (a) the macroscopic axial strain with loading time, the circle corresponds to the onset of debonding, the cross to the nucleation of a crack; (b-c) contours of the stress compoment normal to the cohesive surface at the load level corresponding to the circle (b) and the cross (c) ; (d-e) contours of the cumulated plastic deformation at the onset of fracture (d) and during crack propagation (e).

III.5.1.2. *3D simulations of fracture*

In Figure III-6, we report the results of the simulations for the thinner samples under consideration t=0.25mm and t/R=1. On the load history plot in Figure III-6a, we observe that initiation of debonding takes place at a smaller load level in terms of axial strain compared to the 2D plane strain case (see Figure III-5a). The onset of crack nucleation and related failure is observed for a load level almost three times larger than that at the onset of debonding. The location of the initiation of debonding is located at the maximum of the contour of the stress component normal to the cohesive surface, at the notch tip (Figure III-6b). The maximum of this stress component is shifted ahead the notch tip as debonding continues (Figure III-6c), indicating the location of the cohesive tip. Due to the load carrying capacity of the cohesive surfaces, plastic deformation develops in the surrounding bulk during debonding. The contours of the cumulated plastic deformation during debonding (Figure III-6d) and , at the onset of fracture (Figure III-6e) show that the shape of the plastic zone resembles a flame like with a modest magnitude (less than 40%).

In Figure III-7, we present the results corresponding to the thickness t=1mm, t/R=4. For this thickness, we observe that the onset of debonding takes place for a larger macroscopic load level but plasticity less than 20% takes place at the onset of debonding . The difference between the load level at the onset of debonding and at fracture is smaller than that in the case with t/R=1. The location of onset of debonding and fracture is ahead the notch tip, where the stress concentrates in Figure III-7b and where the stress if close to zero in Figure III-7c. During debonding, the cohesive surfaces separate in directions towards the notch tip and further inside the bulk. Some plasticity is observed at fracture initiation (Figure III-6d), that continues to develop up to crack nucleation (Figure III-6e). The initiation and growth of a crack is presented in the perspective view in Figure III-6f-g. The crack grows similarly to what is observed experimentally (Figure III-4) with an extension of a mirror like zone observable prior to unstable failure. In Figure III-8, the case with thickness t=4mm and t/R=16 is reported. The observations are similar to the case with t/R=4 but the magnitude of the plasticity at the onset of debonding and failure is smaller. Thus, the location of cracking for t=4mm is slightly closer to the notch tip than that for t=1mm (t/R=4).

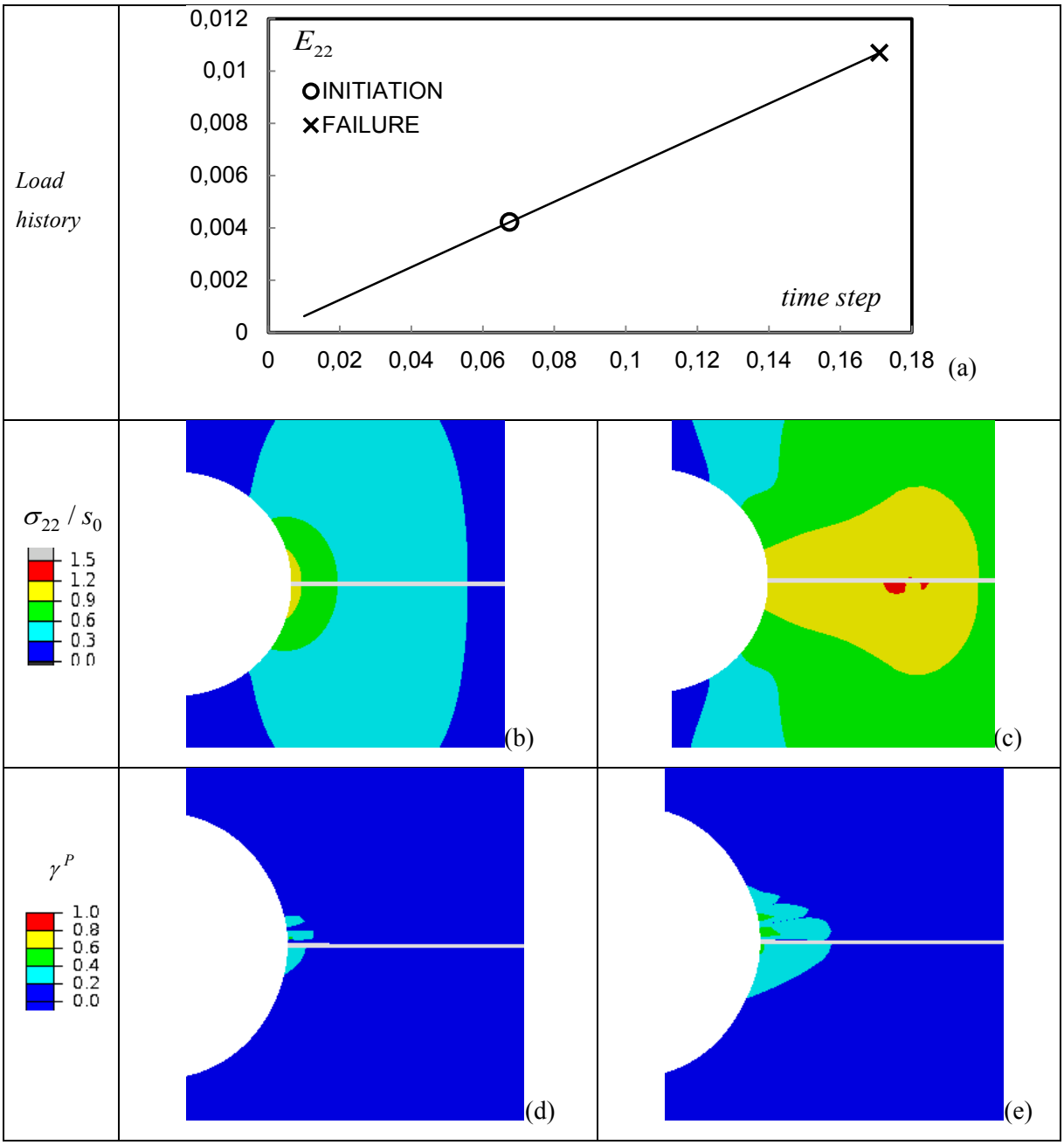

Figure III-6 : 3D simulation for the thickness t=0.25mm, t/R=1, maximum cohesive traction T_{max}=100MPa: (a) the macroscopic axial strain with loading time, the circle corresponds to the onset of debonding, the cross to the nucleation of a crack; (b-c) contours of the stress component normal to the cohesive surface corresponding to the circle (b) and the cross (c); (d-e) cumulated plastic deformation during the debonding (d) and at the onset of fracture (e).

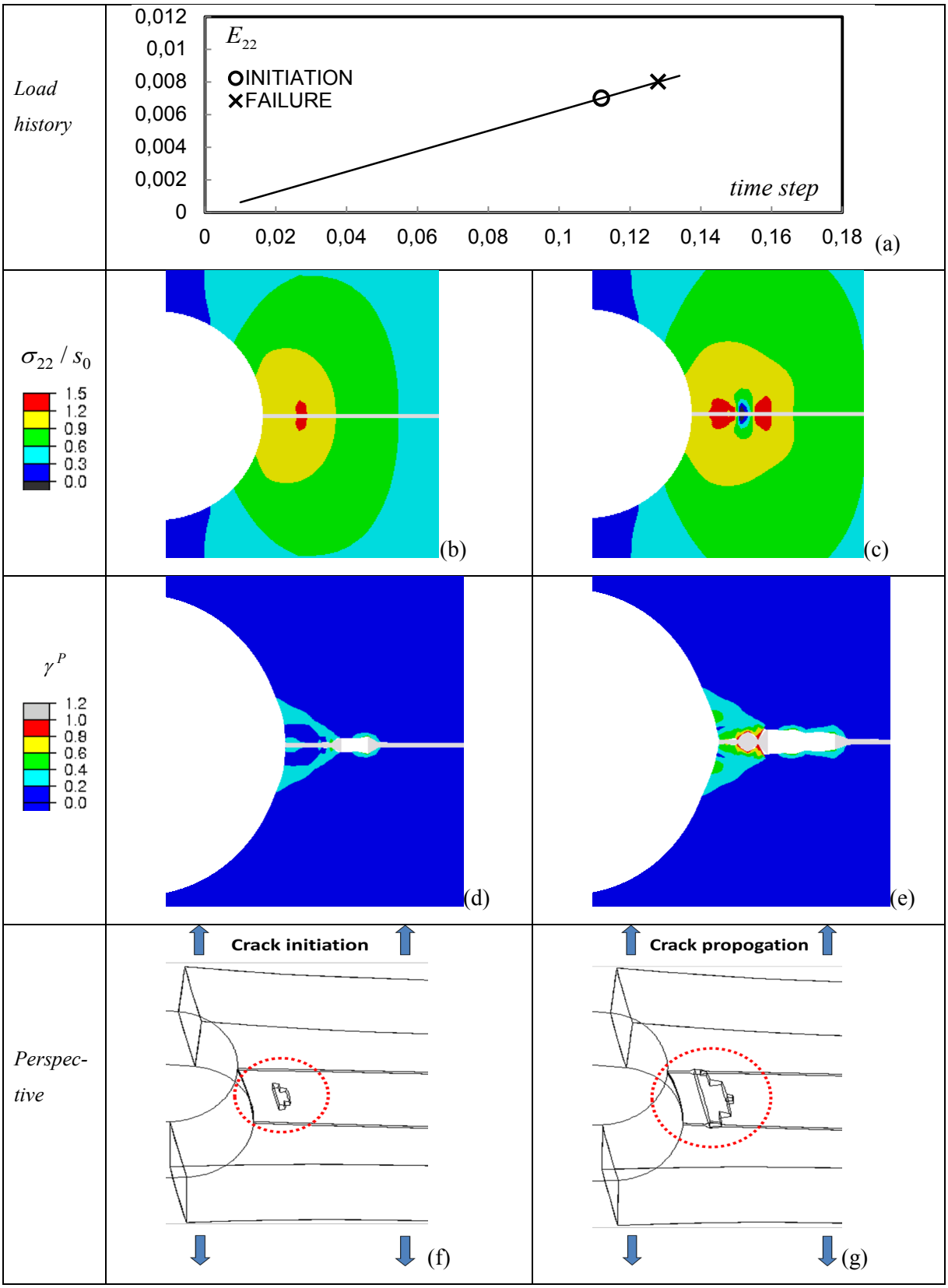

Figure III-7 : 3D simulation for the thickness t=1mm, t/R=4, maximum cohesive traction T_{max}=100MPa: (a) the macroscopic axial strain with loading time, the circle corresponds to the onset of debonding, the cross to the nucleation of a crack; (b-c) contours of the stress component normal to the cohesive surface at the load level corresponding to the circle and the cross; (d-e) the cumulated plastic deformation at the onset of crack nucleation (d) and during crack propagation (e); (f-g) the corresponding extent of the crack.

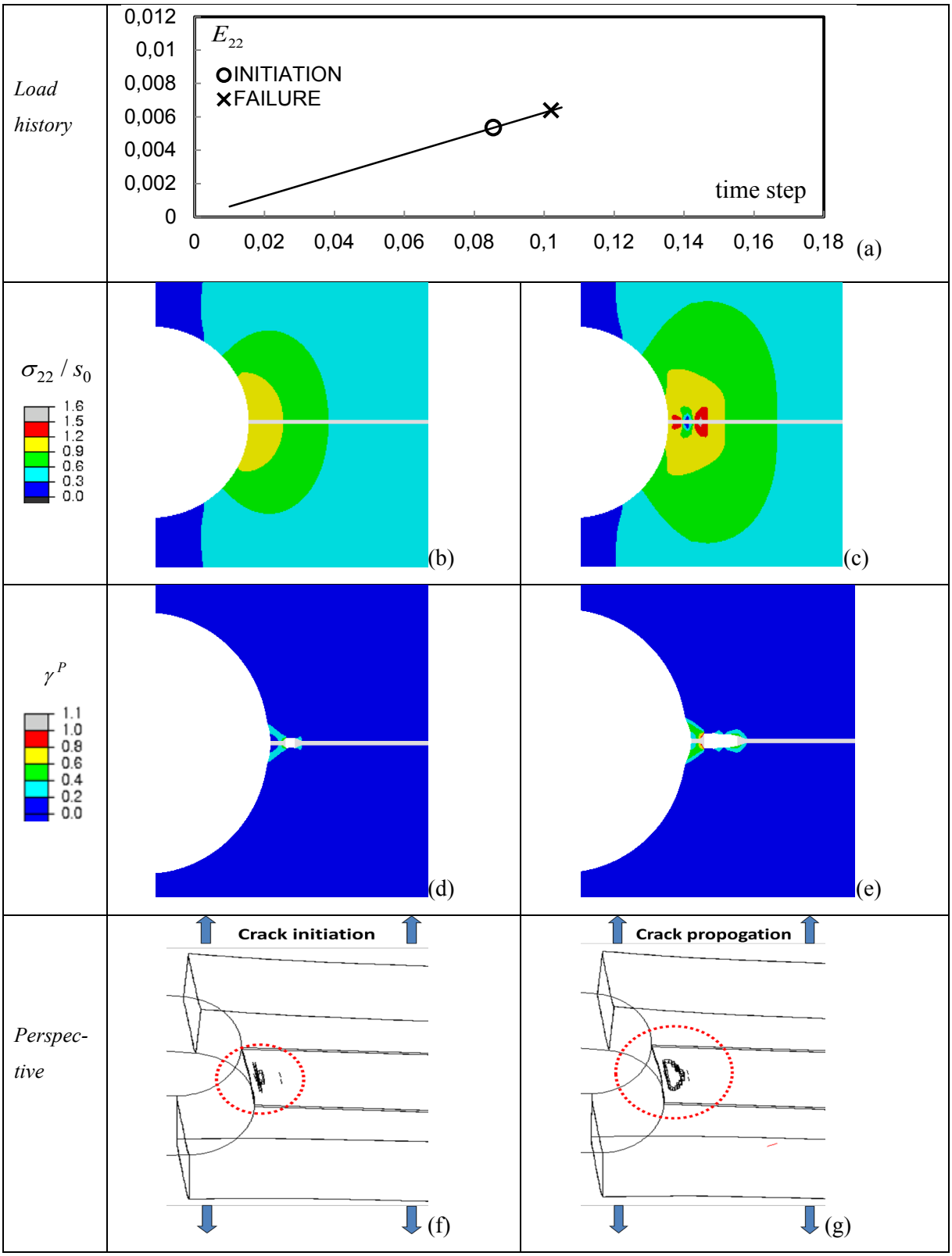

Figure III-8 :3D simulation for the thickness t=4mm, t/R=16, maximum cohesive traction T_{max}=100MPa: (a) the macroscopic axial strain with loading time, the circle corresponds to the onset of debonding, the cross to the nucleation of a crack; (b-c) contours of the stress component normal to the cohesive surface at the load level corresponding to the circle (b) and the cross (c); (d-e) the cumulated plastic deformation at the onset of crack nucleation (d) and during crack propagation (e); (f-g) the corresponding extent of the crack.

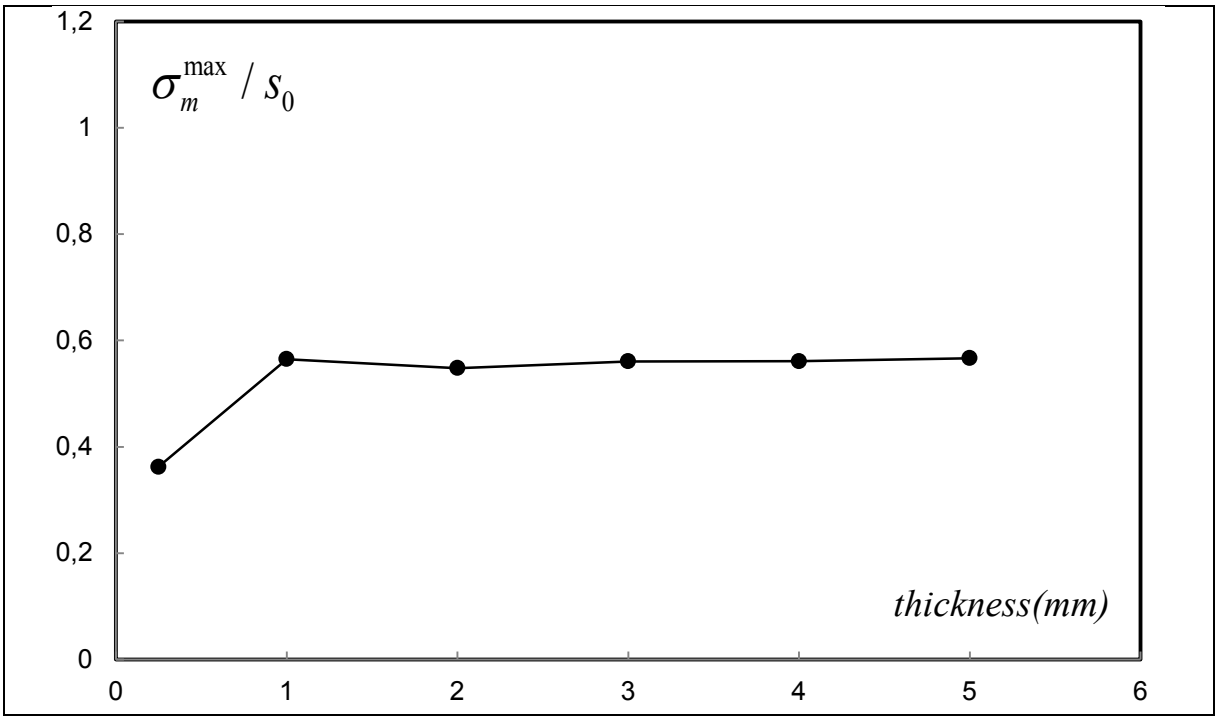

Figure III-9 : Variation of the maximum mean stress normalized with the shear strength s_0 with the thickness, for the 3D calculations with T_{max}=100MPa.

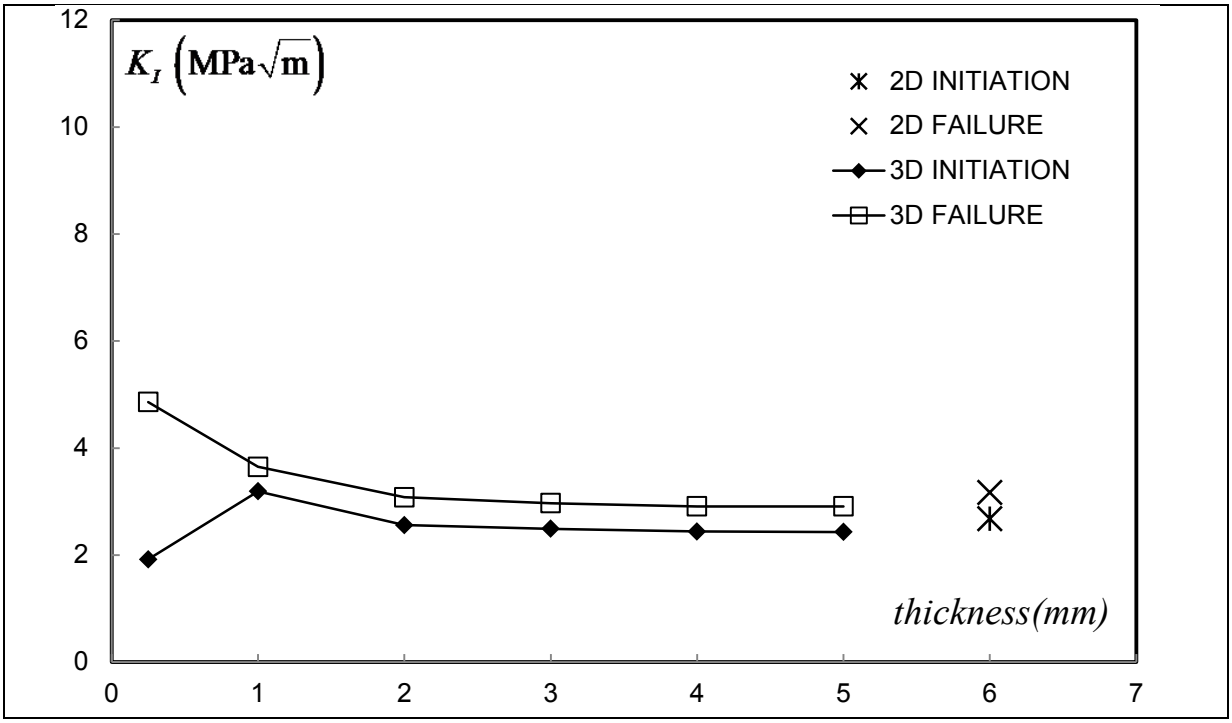

Figure III-10 : Variation of the stress intensity factor $\left(K_I \text{ in MPa}\sqrt{\text{m}}\right)$ with the thickness increasing from 0.25mm to 5mm at the onset of debonding (diamonds) and fracture (squares), for 2D and 3D calculations with T_{max}=100MPa.

In Figure III-9, we reported the variation of the maximum mean stress at the onset of debonding with thickness. For the thinnest sample, its magnitude appear to be the smallest thus corresponding to a thin sample. As soon as the thickness t is larger than 1mm, t/R=1, a constant mean stress at the onset of debonding is observed, of which magnitude $\sigma_m^{CR} \approx 0.6 \times s_0$. This variation illustrates the influence of the thickness at the onset of debonding. However, plasticity develops during debonding for the thinner sample (t=0.25mm, t/R=1) as reported in Figure III-6d-e. For t/R larger than 4, a constant maximum mean stress at the onset of debonding, corresponding to a similar amount of modest plasticity for all thickness under consideration.

In Figure III-10, we report the variation of the stress intensity factor calculated for the geometry of the sample and the macroscopic axial stress at the onset of debonding (diamond symbols) and at fracture (open square symbol). We observed that the toughness decreases with the thickness before a plateau is attained for t=3mm, t/R=12. The onset of crazing is smaller than this value. As plasticity precedes the onset of fracture, a thickness effect is observed with a decrease in the fracture toughness with increasing thickness. The magnitude of the plastic deformation scales with the shear stress that is larger for the thinnest samples and the difference in the principal stress components is enhanced when the stress component along the thickness direction is small or zero. The predicted toughness is about $3\mathrm{MPa}\sqrt{\mathrm{m}}$ which is smaller than values reported experimentally by Parvin and Williams [PAR75] for instance. Thus one may question how relevant are the cohesive parameters adopted here (Table III-2, CZ-REF) and in particular the value of the traction at the onset of debonding T_{max}=100MPa. However, thick sample predictions for the fracture toughness are comparable to that derived from 2D plane stain conditions (see Figure III-10).

If appropriate parameters for failure would be realistic, the variation of the toughness with thickness reported in Figure III-10 contains valuable for those wishing to determine experimentally the material's toughness. In the present case, a thickness larger than t/R=12 (t=3mm) is sufficient.

In the next section, we investigate the influence of the traction at the onset of debonding, with accounting for a larger value increased by 20% (Table III-2, CZ-B).

III.5.2. Influence of the maximum traction of debonding T_{max} on the fracture process

The bulk parameters in Table III-1 for MAT-A and cohesive parameters in Table III-2, CZ-B are now used in the simulations presented in this section. Crazing is allowed in all calculations but now the maximum traction T_{max} is 120MPa instead of 100MPa in the previous section. Careful examination of the stress distribution at the onset and during cohesive debonding up to the nucleation of a crack is presented. 2D plane strain calculations are presented first followed by 3D simulations for which the thickness is varied from 0.25. to 5mm. The influence of the thickness on the shape of the plastic zone in the presence of crazing is analysed. The related stress component normal to the cohesive surfaces or the mean stress and cumulated plasticity distributions are studied and the predictions of the toughness with varying thicknesses are reported.

III.5.2.1. *2D plane strain simulation of fracture*

The plot on the top in Figure III-11a presents the variations of the macroscopic strain with the loading time. The circle corresponds to the onset of debonding of the cohesive surface. For this load level, the bulk response exhibits a negligible plastic deformation as presented in Figure III-11d. The distribution of the stress component normal to the cohesive surface shows a maximum ahead the notch tip where initiation of debonding takes place (Figure III-11b). At the onset of crack nucleation (Figure III-11c), the location of the crack is also ahead the notch tip, where the stress concentration is minimum. The distribution of the cumulated shear strain plasticity shows that some plastic deformation develops during the cohesive surface debonding as observed at the onset of crack nucleation (Figure III-11e). Some shear bands are observed at the onset of failure, along directions at 45° from the notch symmetry plane. The crack nucleates ahead the notch tip, at approximately a distance x such that $x/R \approx 0.6$. Crazing and related cohesive surfaces debonding reduce the amount of plasticity able to develop at the notch tip. Once a crack nucleates, it extends at almost a constant macroscopic load level that is used to estimate the material's toughness. The present 2D plane strain analysis will be compared to the finite geometry accounted for in the 3D calculations.

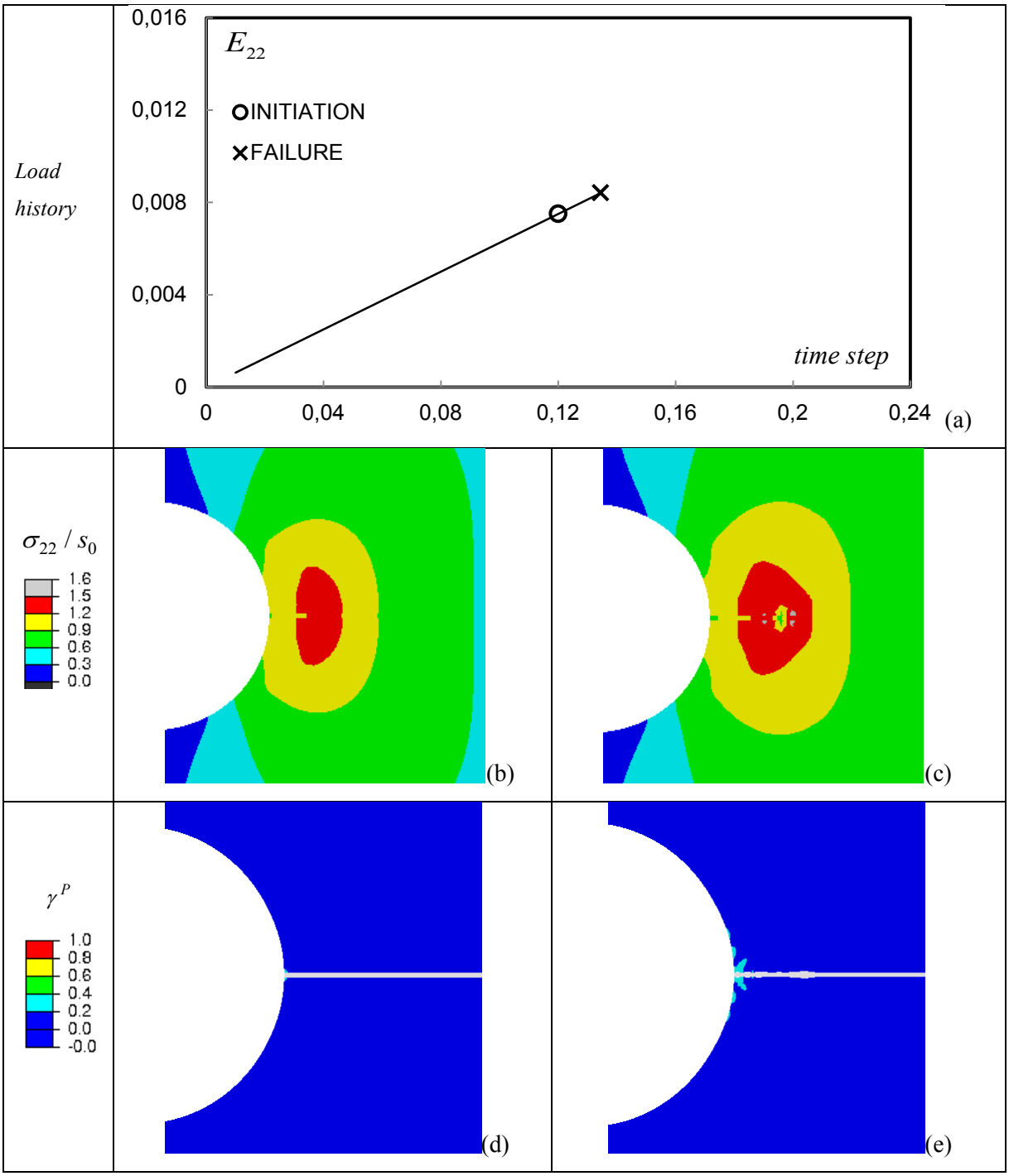

Figure III-11 2D plane strain calculations for T_{max}=120MPa: (a) the macroscopic axial strain with loading time, the circle corresponds to the onset of debonding, the cross to the nucleation of a crack; (b-c) contours of the stress compoment normal to the cohesive surface at the load level corresponding to the circle (b) and the cross (c) ; (d-e) contours of the cumulated plastic deformation at the onset of debonding (d) and at the onset of crack nucleation (e).

III.5.2.2. *3D simulations of fracture*

In Figure III-12, we report the results of the simulations for the thinner samples under consideration t=0.25mm and t/R=1. On the load history plot (Figure III-12a), we observe that initiation of debonding takes place at a smaller load level in terms of axial strain compared to the 2D plane strain case (see Figure III-11a). The onset of crack nucleation and related failure is observed for a load level almost three times larger than that at the onset of debonding. The location of the initiation of debonding is located at the maximum of the contour of the stress component normal to the cohesive surface, at the notch tip (Figure III-12b). The maximum is also at the notch tip at the onset of crack nucleation (Figure III-12c), indicated the location of the cohesive tip. Due to the load carrying capacity of the cohesive surfaces, plastic deformation develops in the surrounding bulk during debonding. The contour of the cumulated plastic deformation during debonding is reported in Figure III-12d during debonding and in Figure III-12e during crack propogation. The shape of the plastic zone is here clearly a flame like with a large magnitude in the plastic deformation approaching 100%. Large plasticity has developed during debonding. Plastic deformation is governed by the shear stress that scales with the difference in the maximum principal stresses that is the largest in the present case as the stress component along the thickness direction is small for this thickness.

In Figure III-13, we present the results corresponding to the thickness t=1mm, t/R=4. For this thickness (see Figure III-13a), debonding takes place for a larger macroscopic load level compared to the case for t/R=1 in Figure III-12a. The difference between the load level at the onset of debonding and at fracture is smaller that in the case with t/R=1. The distribution of the stress component normal to the cohesive surface shows a maximum that coincides with the location of the debonding, at the notch tip where crack nucleates also. Figure III-13d-e present the plastic distribution during debonding (d) up to the onset of fracture (e). This case is similar to the ductile tearing in Essential Work of Fracture experiments. The crack grows similarly to what is observed experimentally [HAS00, COR07]. In Figure III-14, the case with thickness t=4mm and t/R=16 is reported. The observations are similar to the case with t/R=16 with T_{max}=100MPa but the magnitude of the plasticity at the onset of debonding

and failure is larger in this case. Thus, the location of cracking for t=4mm is at a larger distance to the tip than the corresponding case with T_{max}=100MPa.

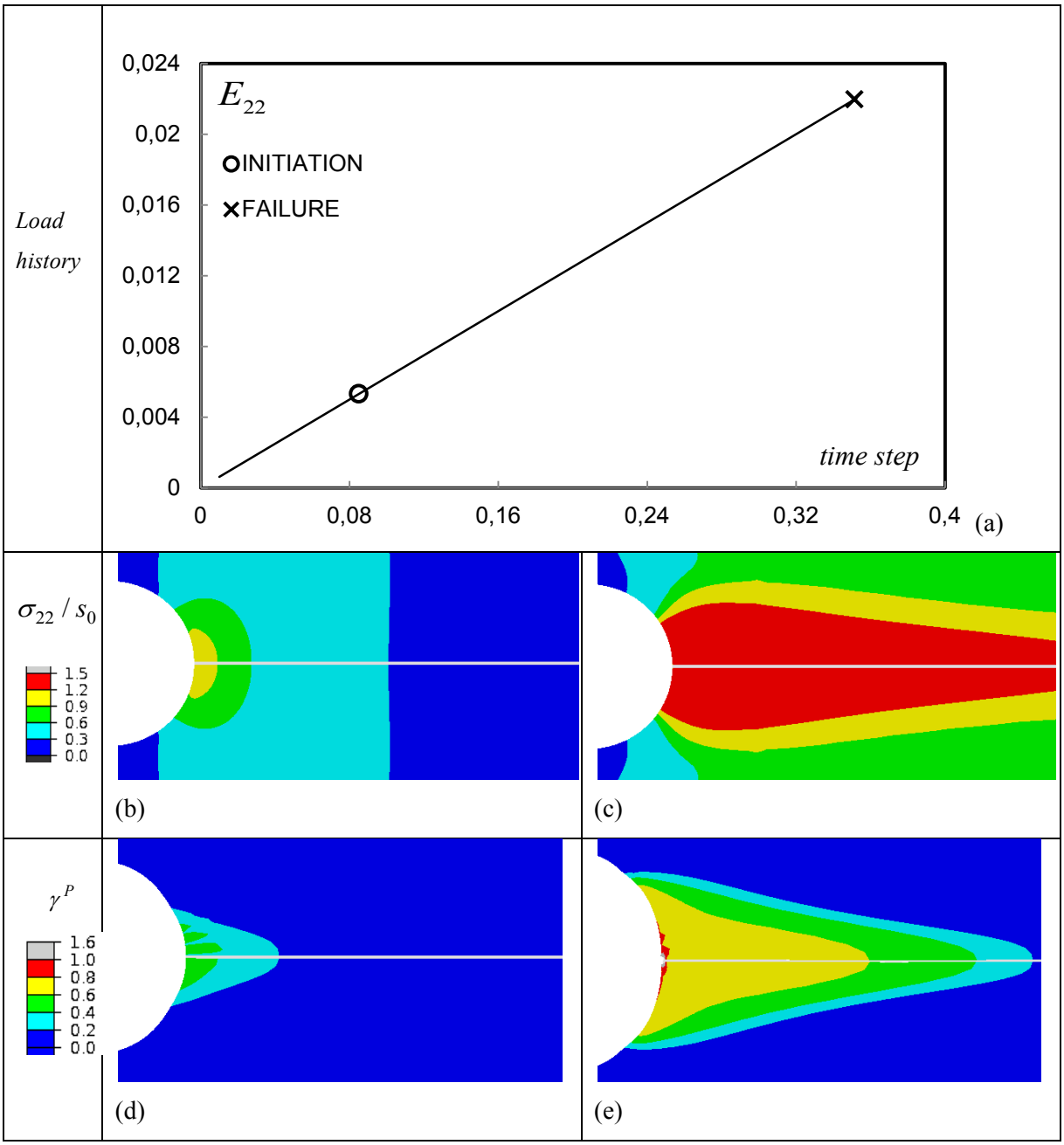

Figure III-12 : 3D simulation for the thickness t=0.25mm, t/R=1, maximum cohesive traction T_{max}=120MPa: (a) the macroscopic axial strain with loading time, the circle corresponds to the onset of debonding, the cross to the nucleation of a crack; (b-c) contours of the stress component normal to the cohesive surface corresponding to the circle (b) and the cross (c); (d-e) cumulated plastic deformation during debonding (d) and during crack propagation (e).

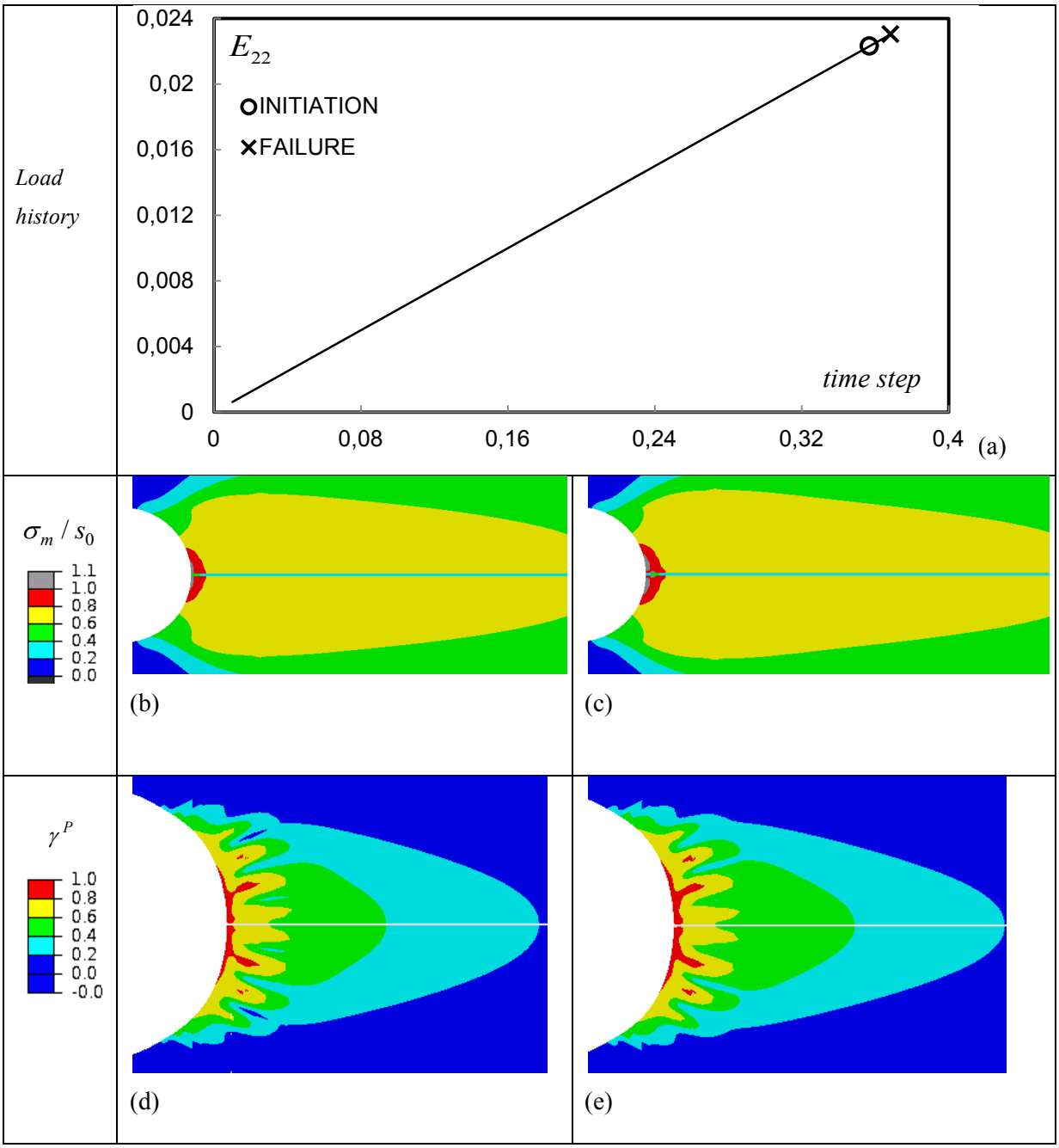

Figure III-13: 3D simulation for the thickness t=1mm, t/R=4, maximum cohesive traction T_{max}=120MPa: (a) the macroscopic axial strain with loading time, the circle corresponds to the onset of debonding, the cross to the nucleation of a crack; (b-c) contours of the stress component normal to the cohesive surface at the load level corresponding to the circle (b) and the cross (c); (d-e) the cumulated plastic deformation during debonding (d) and at the onset of crack nucleation (e).

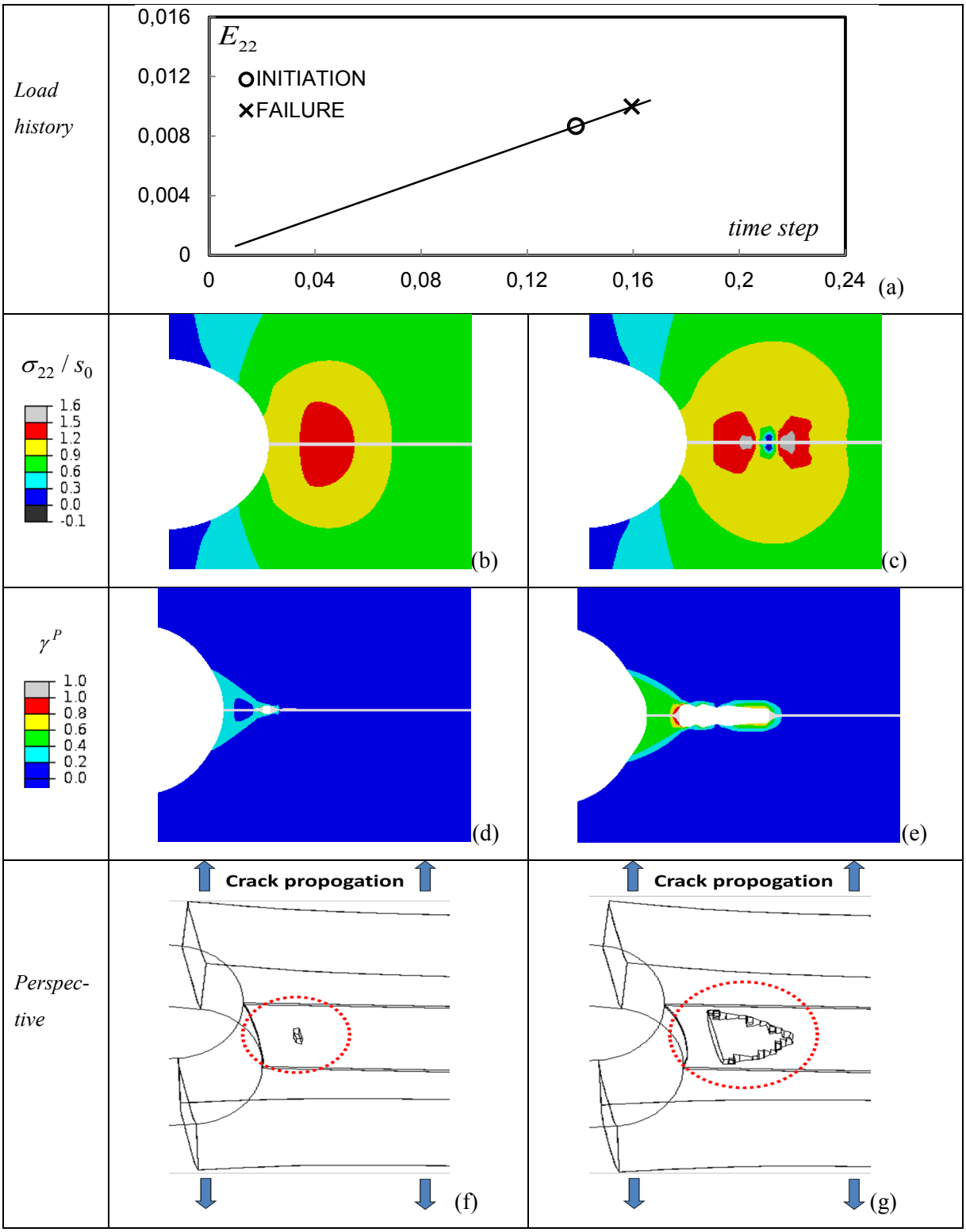

Figure III-14 : 3D simulation for the thickness t=4mm, t/R=16, maximum cohesive traction T_{max}=120MPa: (a) the macroscopic axial strain with loading time, the circle corresponds to the onset of debonding, the cross to the nucleation of a crack; (b-c) contours of the stress component normal to the cohesive surface at the load level corresponding to the circle (b) and the cross (c); (d-e) the cumulated plastic deformation at the onset of crack nucleation (d) and during crack propagation (e); (f-g) the corresponding extent of the crack.

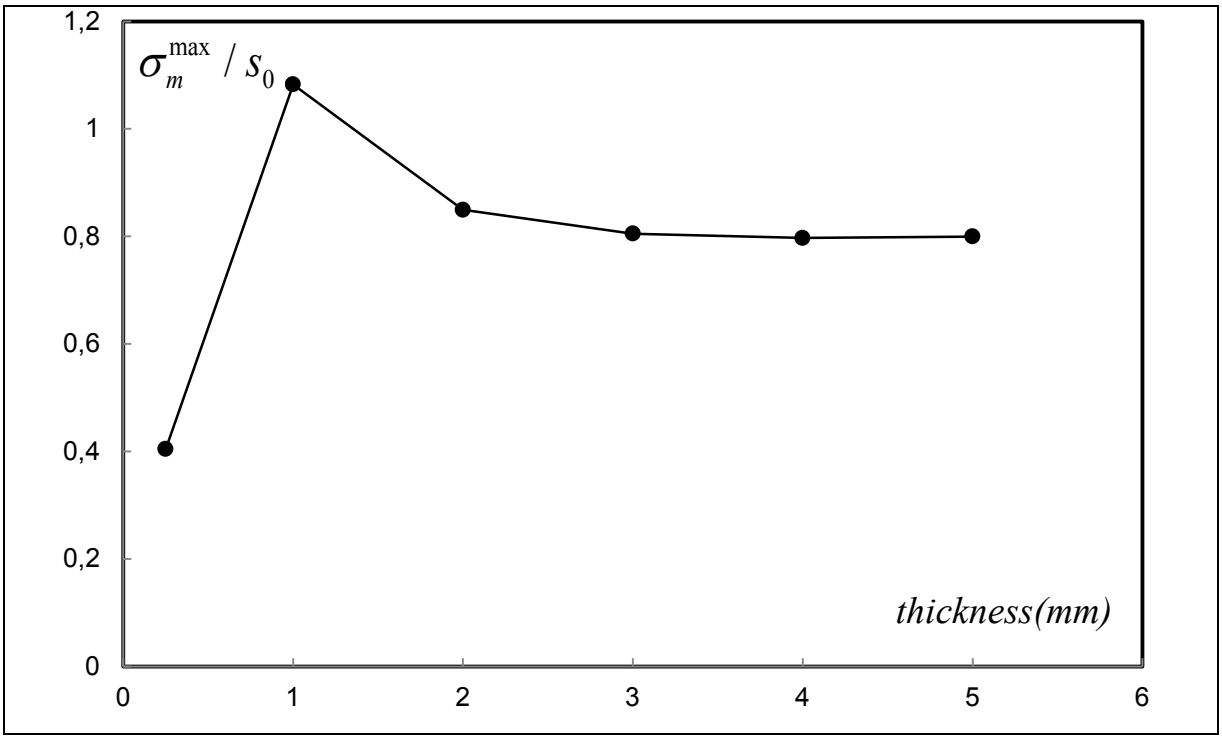

Figure III-15 : Variation of the maximum mean stress normalized with the shear strength s_0 with the thickness, for the 3D calculations with T_{max}=120MPa.

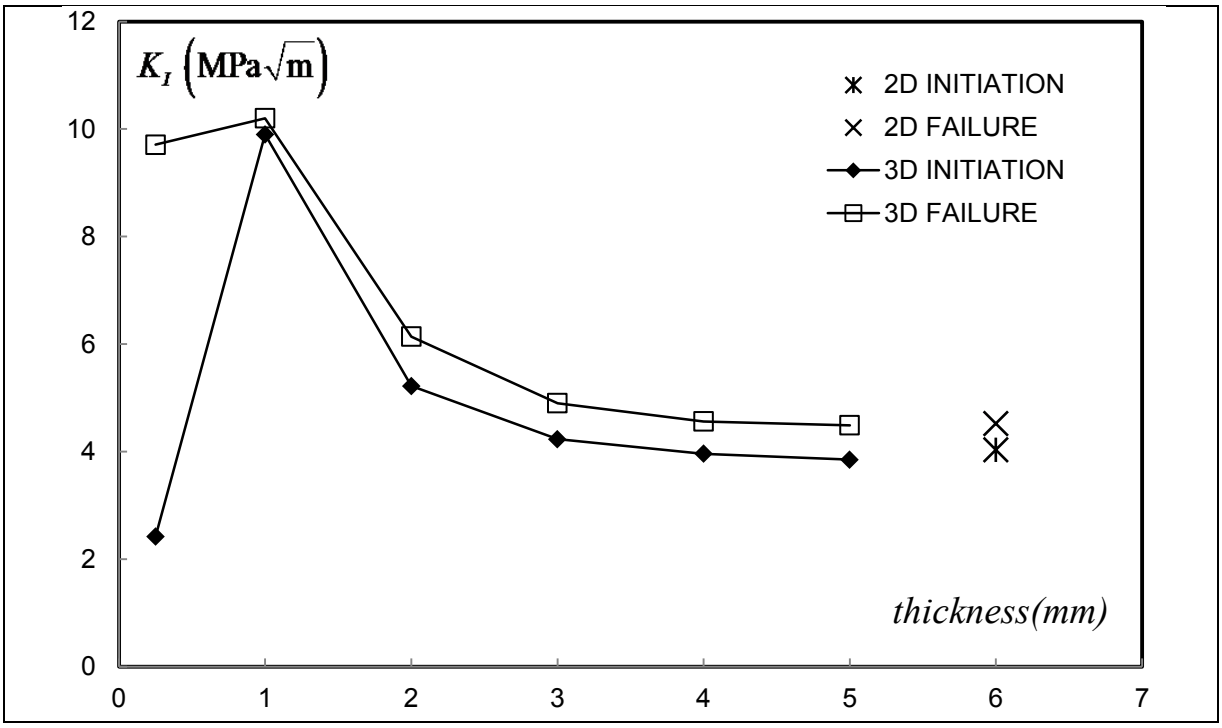

Figure III-16 Variation of the stress intensity factor $\left(K_I \text{ in MPa}\sqrt{\text{m}}\right)$ with the thickness increasing from 0.25mm to 5mm at the onset of debonding (diamonds) and fracture (squares), for 2D and 3D calculations with T_{max}=120MPa.

In Figure III-15, we report the variation of the maximum mean stress at the onset of debonding with thickness. For the thinnest sample, for which the onset of debonding is not preceded by large plastic deformation, its magnitude is the smaller compared to thick samples. For *t/R* larger than 12, a constant maximum mean stress at the onset of debonding is observed, related to 3D stress distribution. An transient reponse is observed for *t*=1mm and 2mm for which the maximum mean stress at the onset of debonding decays with thickness. For the thick specimens with *t/R* larger than 12, the level of the mean stress for the onset of debonding shows a plateau for $\sigma_m^{\max} / s_0 \approx 0.8$ with the present maximum traction $T_{\max}$=120MPa, while a plateau was observed for $\sigma_m^{\max} / s_0 \approx 0.6$ for $T_{\max}$=100MPa in the previous section (Figure III-9). The increase in the level of the maximum mean stress is about 33%. The increase in the maximum traction is of 20%. The larger critical mean stress at th onset of debondnig originates in the development of plasticity that induces an increase in the mean stress in order to ensure the continuity of the displacement fields.

In Figure III-16, the variation of the stress intensity factor calculated for the geometry of the sample and the macroscopic axial stress at the onset of debonding and at fracture is reproted. The fracture toughness decreases with the thickness before a plateau is attained for *t*=4mm, *t/R*=16, for a thickness larger than that for $T_{\max}$=100MPa. Its value is about $4.5\,\mathrm{MPa}\sqrt{\mathrm{m}}$, similar to that reported by Parvin and Williams [PAR75], although these authors considered sharp notches, or at least as sharp as possible. The plasticity that develops prior to fracture is likely to induce large notch blunting so that the present value is compared to that reported in [PAR75] for thick samples.

Using a larger traction at the onset of debonding in the cohesive model results in a prediction of the plastic zone at the onset of fracture (Figure III-12d-e and Figure III-13d-e) qualitatively comparable to that reported in [HAS00, COR07] for thin specimens, polymer films: the plastic zone has a a flame like profile. A plastic zone comparable to Hill's slip line fields [HIL50, LAI97] is observed for the thick samples (Figure III-14d-e). This observation can be used to approximately select the traction at the onset of debonding in the cohesive model.

In Figure III-16, the fracture toughness corresponded to the 2D plane strain calculation is also reported. The plateau of the minimum fracture toughness observed in the 3D calculations is close to that estimated from the 2D plane strain calculations.

Two information can be derived from Figure III-16 with the variation of the fracture toughness with thickness. This plot indicates that for a thickness with notch radius t/R larger than 16 to 20, a minimum toughness can be estimated. This information is valuable for those wishing to determine experimentally the material's toughness, provided that the cohesive model for crazing is realistic. For the fracture toughness predicted in the thick 3D calculations with t/R larger than 16, the related estimations match with that estimated from 2D plane strain calculations. As the fracture is governed by the characteristics of the cohesive model, these predictions between thick samples and 2D plane strain simulations converged to a similar toughness for sufficiently thick samples.

In the following section, we investigate the influence of the bulk strain softening and cohesive maximum critical opening on the crack tip fields and fracture predictions.

III.5.3. Influence of the strain softening on 3D fracture simulations

The bulk parameter in Table III-1 is now for MAT-B and cohesive parameters in Table III-2, CZ-B are used in the simulations presented in this section. Crazing is allowed in all calculations but now the maximum traction T_{max} is 120MPa and a larger strain softening of the bulk upon yielding is considered. This material is thus prone to major shear yielding and formation of multiple shear bands as reported in charpter 2. Careful examination of the stress distribution at the onset and during cohesive debonding up to the nucleation of a crack is presented. 2D plane strain calculations are presented first followed by 3D simulations for which the thickness is varied from 0.25 to 5mm. The influence of the thickness on the shape of the plastic zone in presence of crazing is analysed. The related stress component normal to the cohesive surfaces or the mean stress and cumulated plasticity are studied and the predictions of the toughness with varying thicknesses are reported.

III.5.3.1. *2D plane strain simulation of fracture*

The plot on the top in Figure III-17 presents the variation of the macroscopic strain with the loading time. The circle corresponds to the onset of debonding of the cohesive surface. The distribution of the stress component normal to the cohesive surface (Figure III-17b) shows a maximum ahead the notch tip corresponding to the location where initiation of debonding takes place. At the onset of crack nucleation (Figure III-17c), the location of the crack is also ahead the notch tip, where the minimum stress is observed. The distribution of the cumulated shear strain plasticity shows that some plastic deformation develops during the cohesive surface debonding (Figure III-17d). A web of shear bands is now observed, compared to the contours reported for MAT-A, at the onset of crack nucleation and during crack propogation (Figure III-11d-e). The crack nucleates at the shear bands crossing. Once a crack nucleates, it extends at almost a constant macroscopic load level that is used to estimate the material's toughness. The present 2D plane strain analysis will be compared to the finite geometry accounted for in the 3D calculations.

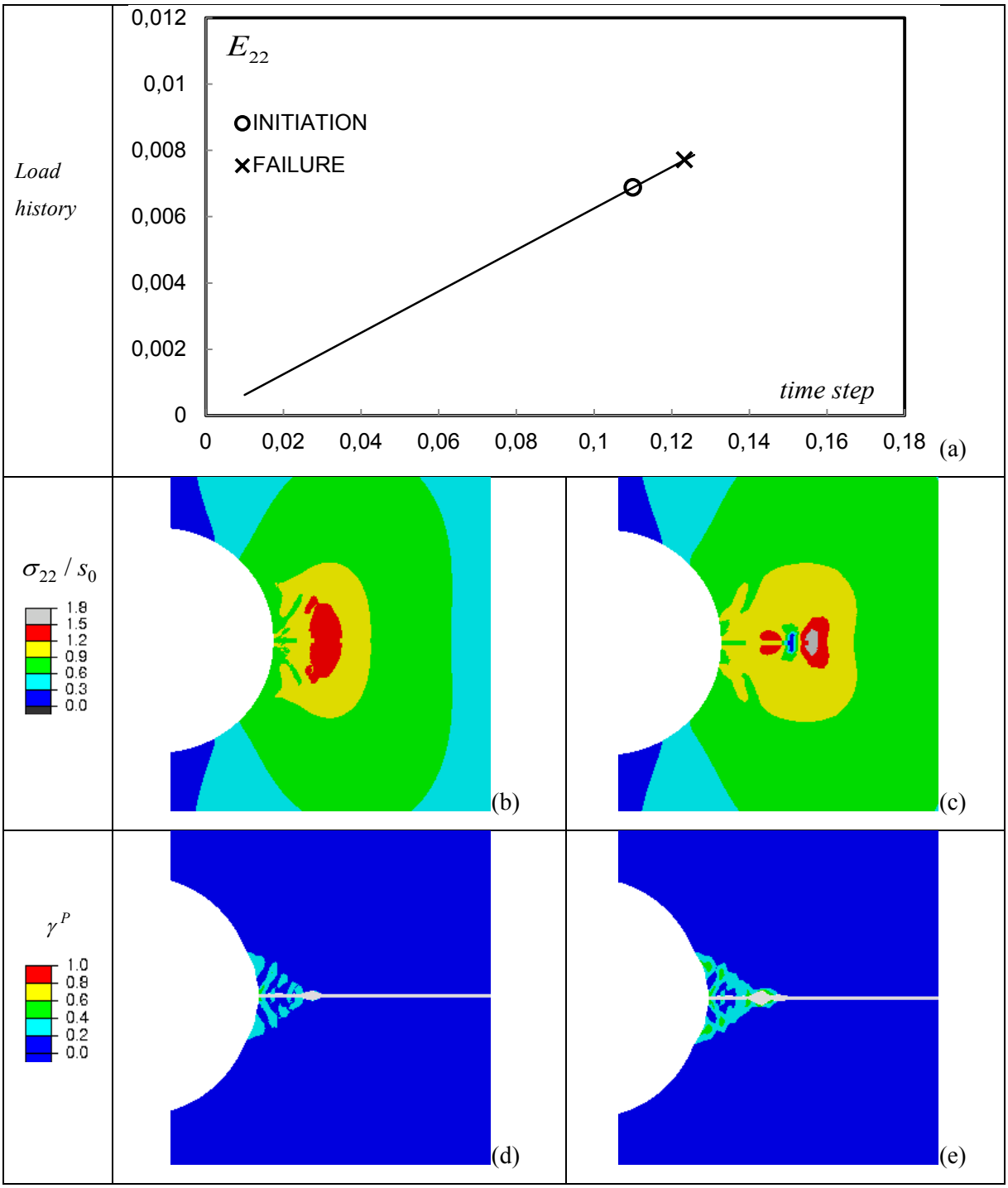

Figure III-17 : 2D plane strain calculations for T_{max}=120MPa and the bulk parameter MAT-B in Table III-1: (a) the macroscopic axial strain with loading time, the circle corresponds to the onset of debonding, the cross to the nucleation of a crack; (b-c) contours of the stress compoment normal to the cohesive surface at the load level corresponding to the circle (b) and the cross (c) ; (d-e) contours of the cumulated plastic deformation at the onset of fracture (d) and during crack propagation (e).

III.5.3.1. *3D simulations of fracture*

In Figure III-18, we report the results of the simulations for the thinner samples under consideration t=0.25mm and t/R=1. Figure III-18a presents the load history in terms of axial macroscopic strain component with loading time. Initiation of debonding takes place at a smaller load level in terms of axial strain compared to the 2D plane strain case (Figure III-17a). The onset of crack nucleation and related failure is observed for a load level almost three times larger than that at the onset of debonding. The location of the initiation of debonding is located at the maximum of the contour of the stress component normal to the cohesive surface, at the notch tip (Figure III-18b). At the onset of fracture, the maximum stress is also at the notch tip (Figure III-18c). The contours of the cumulated plastic shear strain are presented in Figure III-18d during debonding and at the onset of crack nucleation (Figure III-18e). Noticeable plasticity proceeds during the opening of the cohesive surfaces with a plastic zone that has a flame like profile. The magnitude of the plastic deformation at the onset of failure approaches 100% so that failure by ductile tearing is likely to take place.

In Figure III-19, we present the results corresponding to the thickness t=1mm, t/R=4. For this thickness, we observe that the onset of debonding takes place for a larger macroscopic load level (Figure III-19a). The difference between the load level at the onset of debonding and at fracture is smaller than that in the case with t/R=1. The distribution of the stress component normal to the cohesive surface (Figure III-19b-c) show a maximum that coincides with the location of the debonding and at fracture, at the notch tip too. Large plasticity takes place at the onset of debonding (Figure III-19d) and at the onset of fracture (Figure III-19e). The plastic zone has a flame like shape that is characteristic of thin samples [HAS00, COR07]. Due to a larger strain softening of the bulk, a more heterogeneous plastic zone is observed, however. In Figure III-20, the case with thickness t=4mm and t/R=16 is reported. The observations are similar to the case with t/R=16 with T_{max}=120MPa and bulk material-A (Table III-1). The location for the onset of debonding corresponds to that of the stress concentration in Figure III-20b and that for crack nucleation corresponds to the minimum stress location in Figure III-20c. Figure III-20d-e show the cumulated plastic shear strain at the onset of failure and during crack propagation. The plastic zone is comparable to that observed in for the

previous bulk parameters (see Figure III-14) and resembles a plastic zone predicted by Hill's slip lines [HIL50, LAI97] .

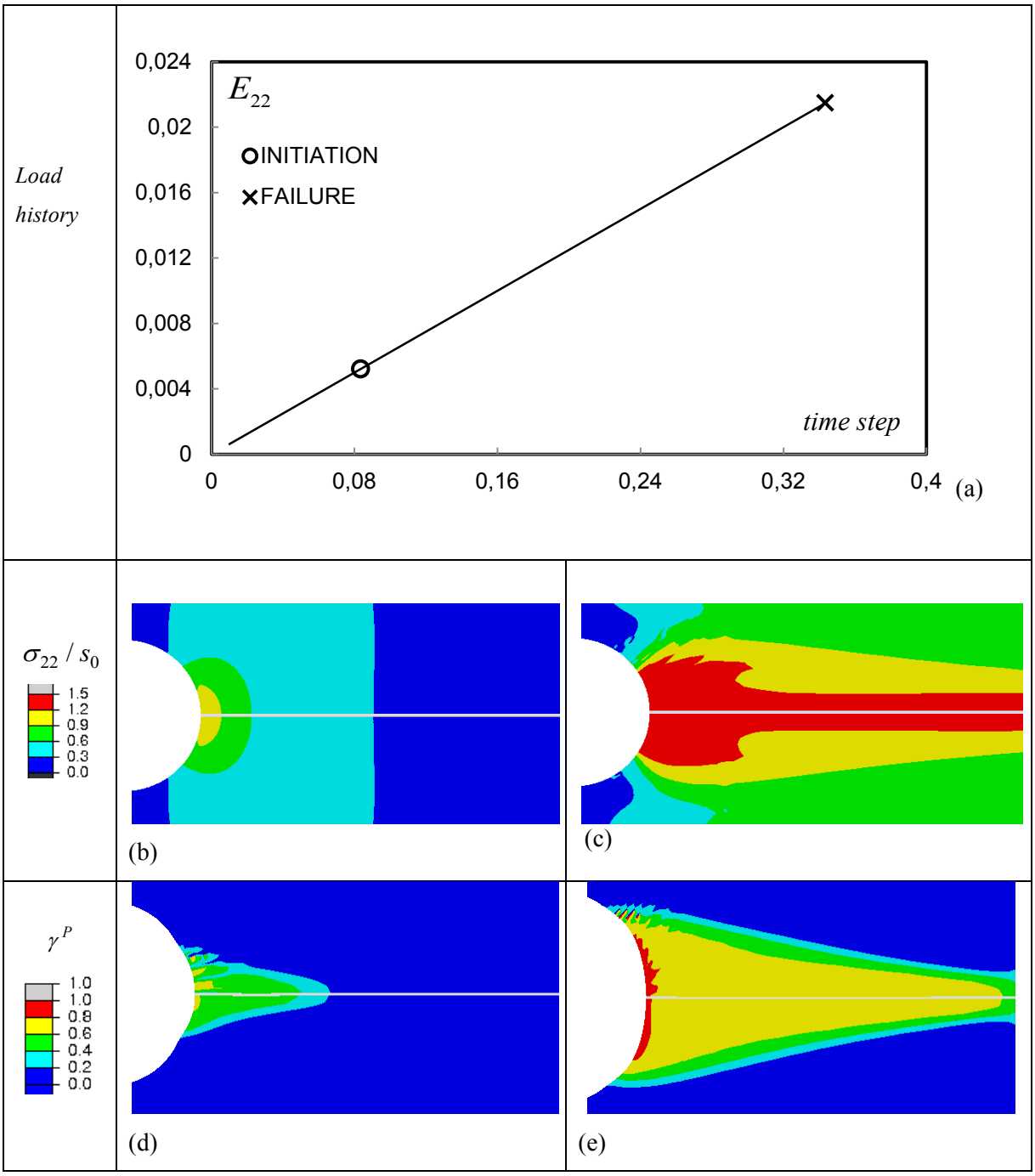

Figure III-18: 3D simulation for the thickness t=0.25mm, t/R=1, maximum cohesive traction T_{max}=120MPa and the bulk parameter MAT-B in Table III-1: (a) the macroscopic axial strain with loading time, the circle corresponds to the onset of debonding, the cross to the nucleation of a crack; (b-c) contours of the stress component normal to the cohesive surface corresponding to the circle (b) and the cross (c); (d-e) cumulated plastic deformation during debonding (d) and at the onset of fracture (e).

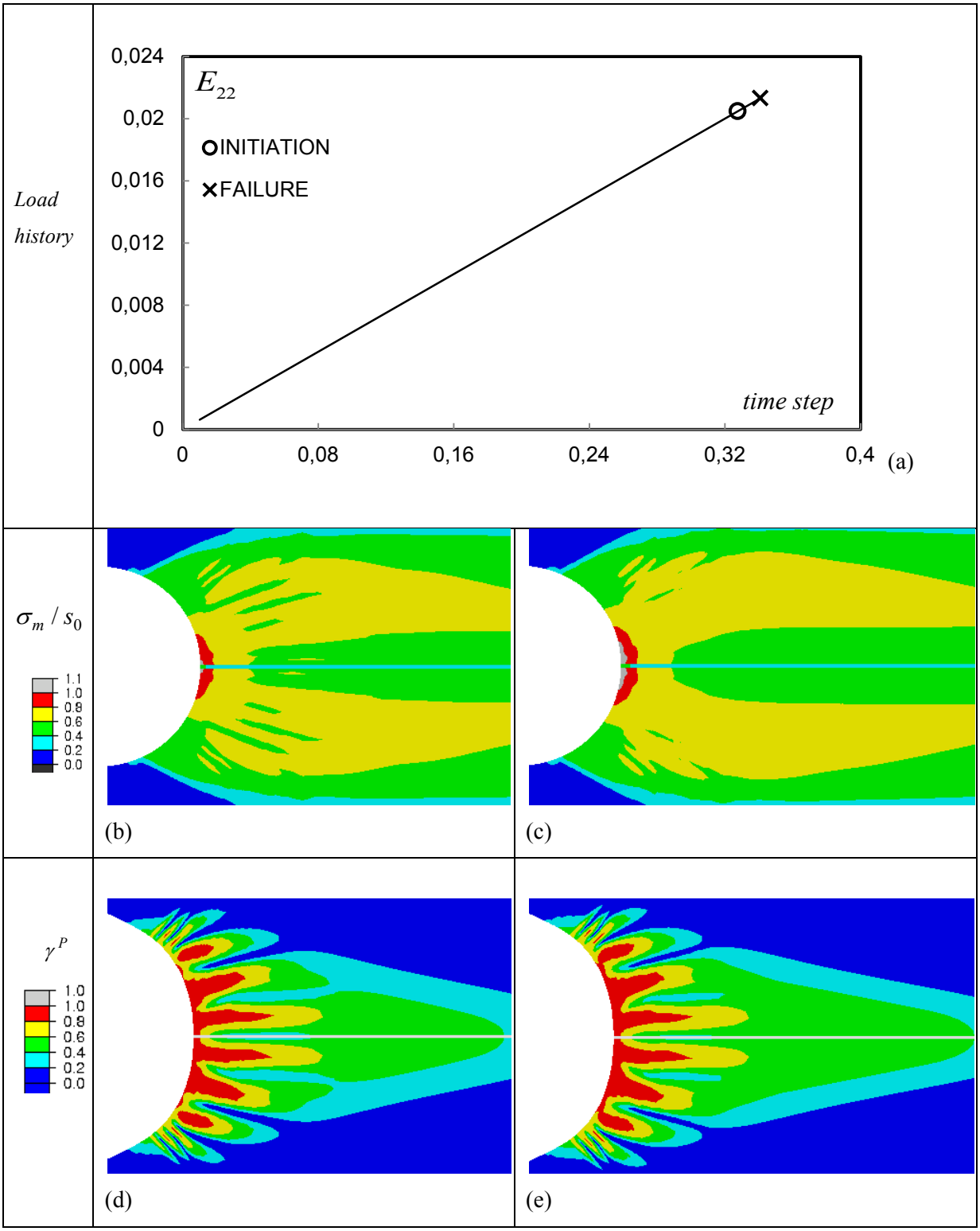

Figure III-19 3D simulation for the thickness t=1mm, t/R=4, maximum cohesive traction T_{max}=120MPa and the bulk parameter MAT-B in Table III-1: (a) the macroscopic axial strain with loading time, the circle corresponds to the onset of debonding, the cross to the nucleation of a crack; (b-c) contours of the stress component normal to the cohesive surface corresponding to the circle (b) and the cross (c); (d-e) cumulated plastic deformation during debonding (d) at the onset of fracture (e).

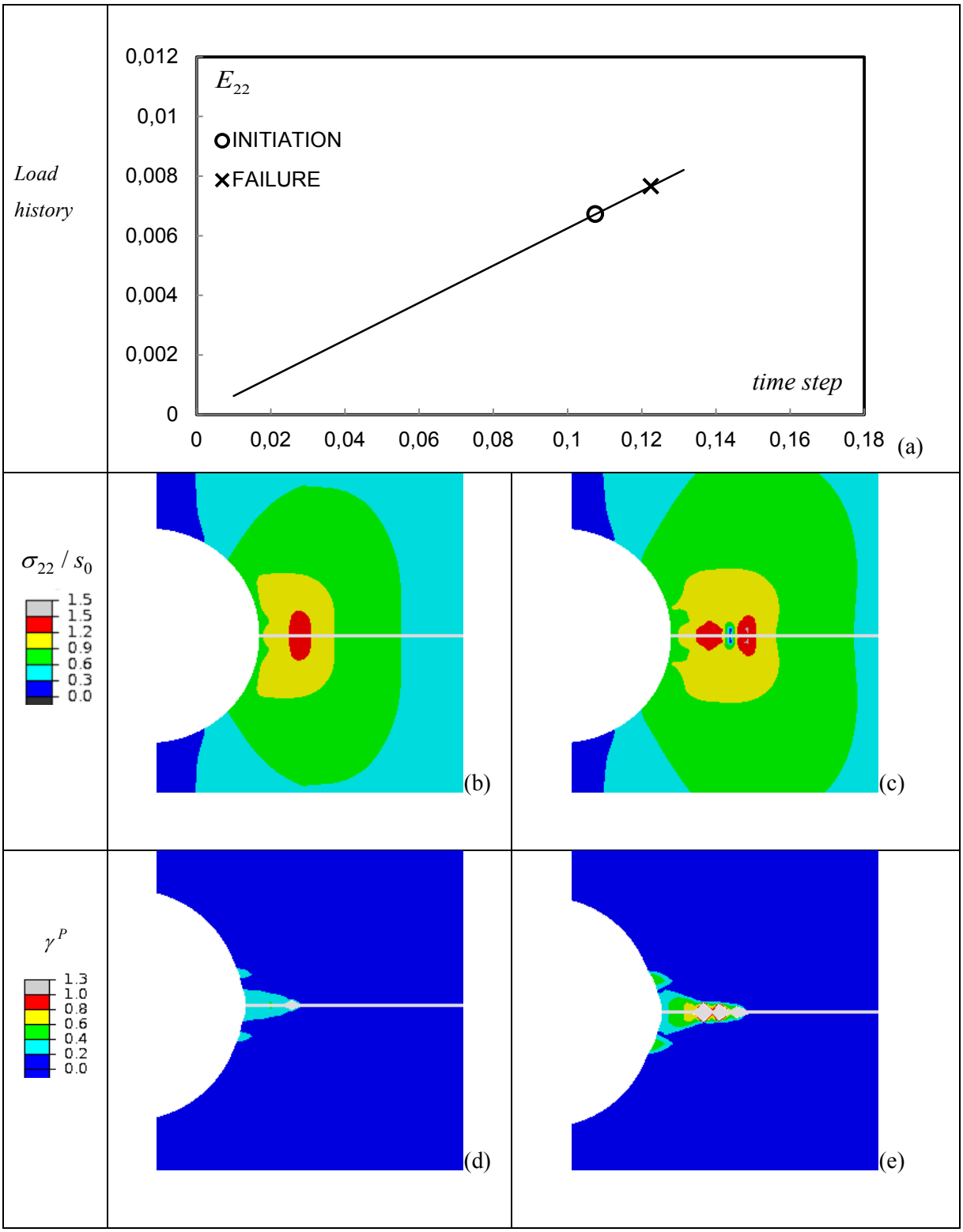

Figure III-20 **:** 3D simulation for the thickness t=4mm, t/R=16, maximum cohesive traction T_{max}=120MPa and the bulk parameter MAT-B in Table III-1: (a) the macroscopic axial strain with loading time, the circle corresponds to the onset of debonding, the cross to the nucleation of a crack; (b-c) contours of the stress component normal to the cohesive surface corresponding to the circle (b) and the cross (c); (d-e) cumulated plastic deformation at the onset of fracture (d) and during crack propagation (e).

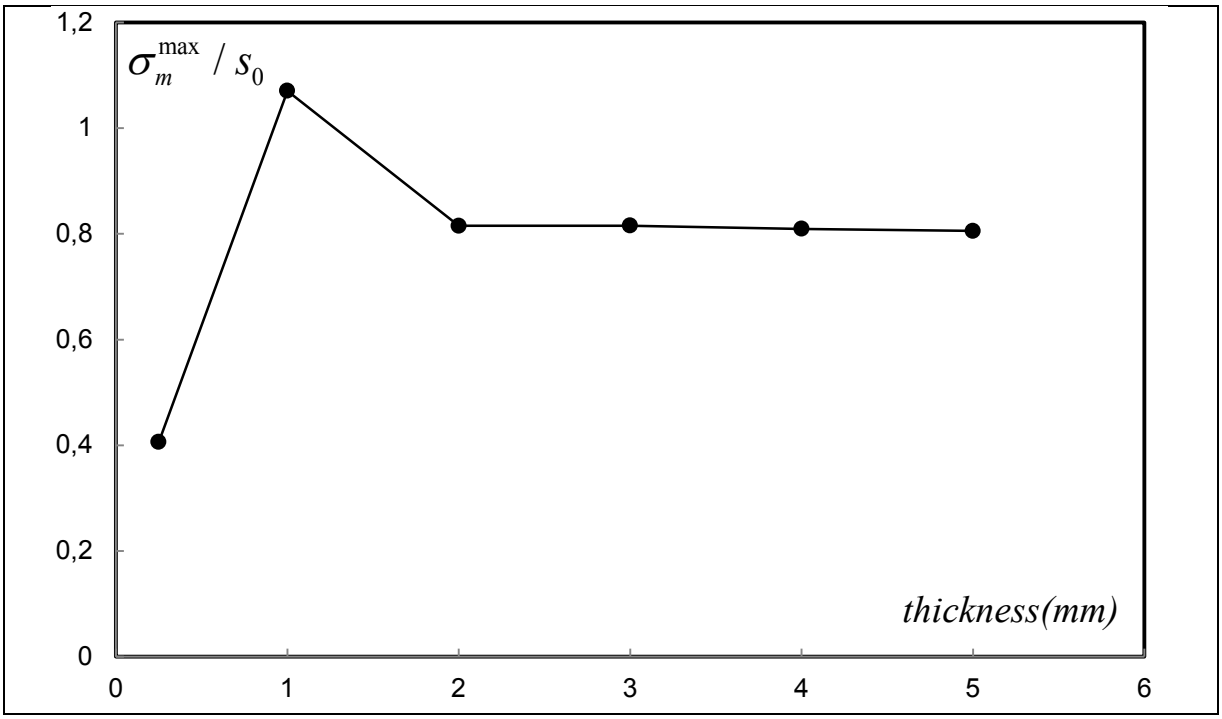

Figure III-21 : Variation of the maximum mean stress normalized with the shear strength s_0 with the thickness, for the 3D calculations with T_{max}=120MPa and bulk material MAT-B.

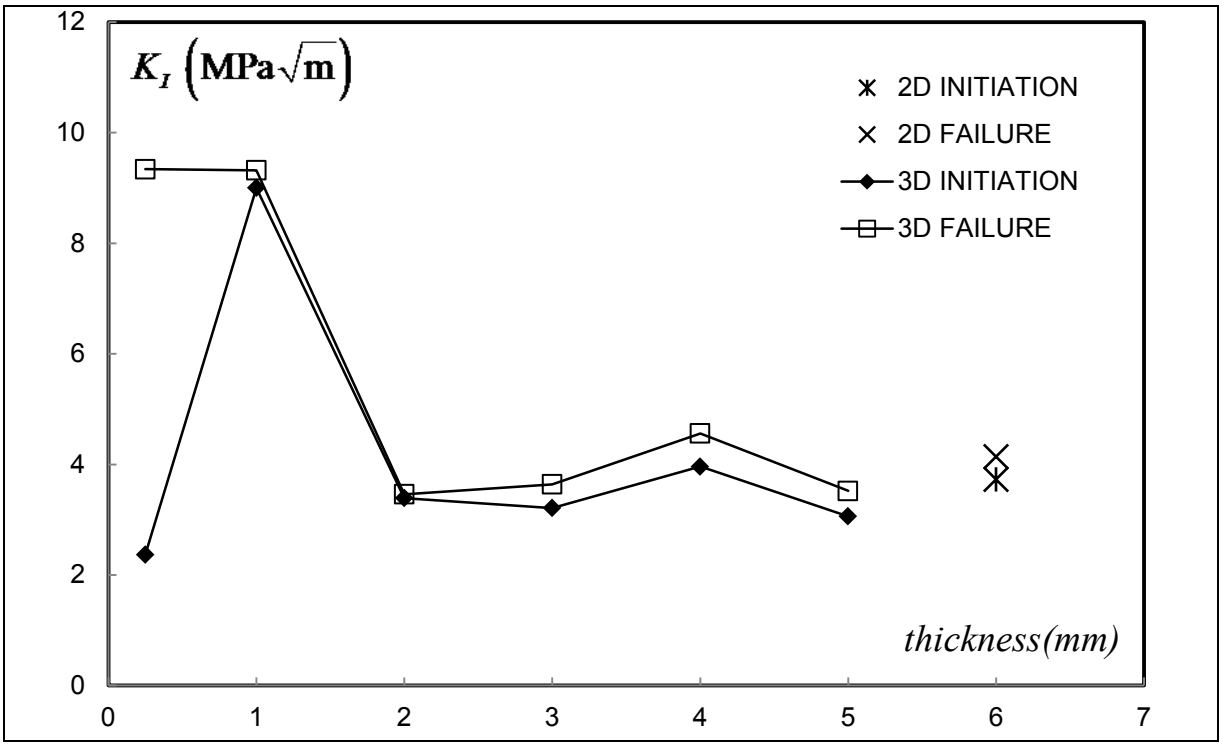

Figure III-22 : Variation of the stress intensity factor $\left(K_I \text{ in MPa}\sqrt{\text{m}}\right)$ with the thickness increasing from 0.25mm to 5mm at the onset of debonding (diamond) and fracture (squares), for 2D and 3D calculations with T_{max}=120MPa and bulk material MAT-B.

In Figure III-21, the variation of the maximum mean stress at the onset of debonding with thickness is reported. For the thinnest sample with t=0.25mm (t/R=1), the lowest value of the mean stress is observed as in Figure III-9 and Figure III-15. The maximum mean stress is the highest for t=1mm ($t/$R=4) and gradually decays with thickness. The transition from plane stress to plane strain calculation is observed. For t/R larger than 8, a constant maximum mean stress at the onset of debonding, corresponding to a similar amount of modest plasticity is observed. The value of this plateau is comparable to that observed in Figure III-15 for the bulk material A.

In Figure III-22, we report the variation of the stress intensity factor calculated for the geometry of the sample and the macroscopic axial stress at the onset of debonding and at fracture. After a bump like variation between t=0.25mm to t=2mm, the toughness decreases with the thickness before a plateau is attained for a thickness larger than t=2mm, t/R=8. The plateau of the fracture toughness is reached for a thickness smaller than that for T_{max}=120MPa, bulk MAT-A. This plot indicates that for a thickness with notch radius t/R larger than 8, a minimum toughness can be estimated, although some variations are observed. This is likely due to the heterogeneous stress fields developed during debonding due to the formation of a more heterogeneous plastic zone. The toughness is comparable to that estimated from 2D plane strain calculations, however. This information is valuable for those willing to determine experimentally the material's toughness, provided that the cohesive model for crazing is realistic.

III.5.4. Influence of cohesive critical opening Δ_{max}

The influence of the critical opening Δ_{max} corresponding to the nucleation of a crack is examined. The reference bulk material A (Table III-1) is used with the maximum traction T_{max} =120MPa. The cohesive parameters CZ-C (Table III-2) with a maximum opening Δ_{max}=6 μm are now considered for the thick specimens, with a thickness t larger than 2 mm, and an additional calculations with Δ_{max}=9μm will be also reported. Illustrations are reported for the case with 4mm. Results are present in Figure III-23. The plot in Figure III-23a shows the load level for the intiation of debonding and that for the onset of failure. In Figure III-23b-c, the distribution of the stress component normal to the cohesive surface is reported. The location of debonding corresponds to that of the stress concentration in Figure III-23b. A crack nucleates where the stress is minimum in Figure III-23c. Both locations are ahead the notch tip, in the bulk. Figure III-23d presents the distribution of the cumulated plastic shear strain at the onset of failure and during crack propagation (Figure III-23e). The variation of the fracture toughness with thickness is reported in Figure III-24. The maximum opening has almost no influence on the predicted toughness for Δ_{max} ranging from 3 microns to 9 microns. Changing the value of the maximum opening has some influence on the location of the onset of fracture as reported in Figure III-25. This location increases with the maximum cohesive opening Δ_{max}. This observation can therefore be used to estimate its value. A distance x from the notch tip with respect to the notch radius R is observed to be smaller than one: this estimation is smaller than that observed by Ishikawa et al. [ISH77] for instance who report a value of x/R close to 1.5. However, the two estimates are not directly comparable as the specimen's ligament in Ishikawa et al.'s experiment is smaller than the present investigation so that constraints from boundary effects are likely to take place and influence the location of the crack.

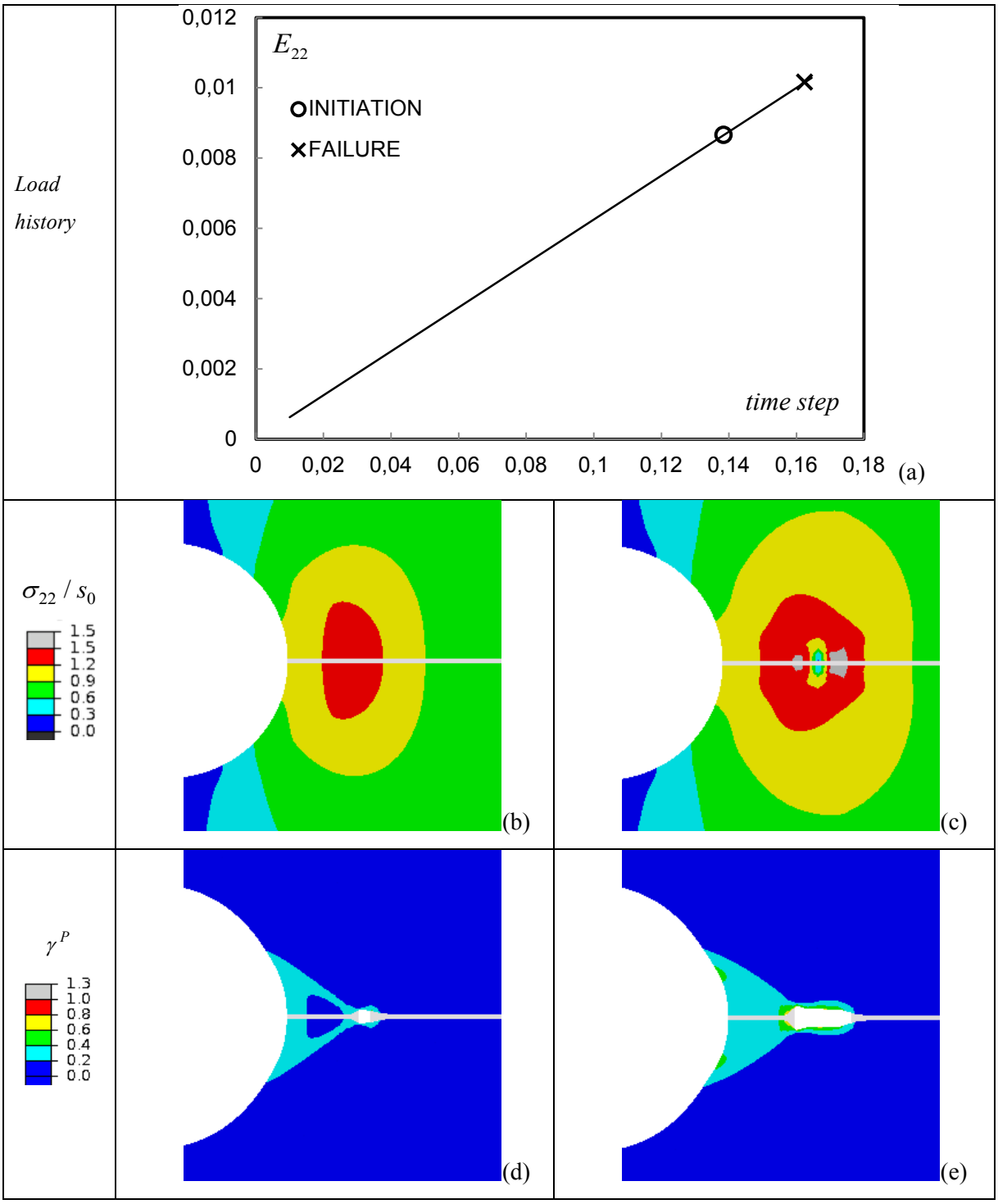

Figure III-23: 3D simulation for the thickness t=4mm, t/R=16, maximum cohesive traction T_{max}=120MPa and Δ_{max}=6mm, with the bulk parameter MAT-A in Table III-1: (a) the macroscopic axial strain with loading time, the circle corresponds to the onset of debonding, the cross to the nucleation of a crack; (b-c) contours of the stress component normal to the cohesive surface corresponding to the circle (b) and the cross (c); (d-e) cumulated plastic deformation at the onset of fracture (d) and during crack propagation (e).

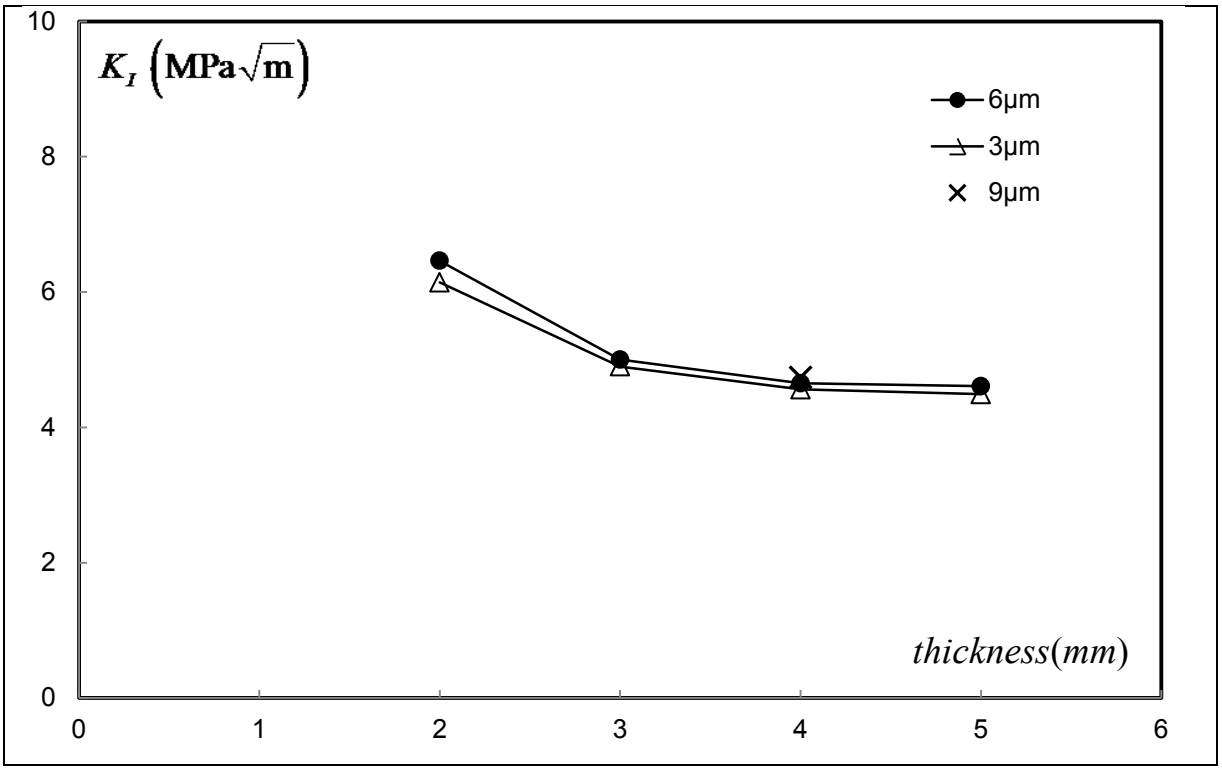

Figure III-24: Influence of the cohesive surface critical opening Δ_{max} on the fracture toughness with increasing thicknesses.

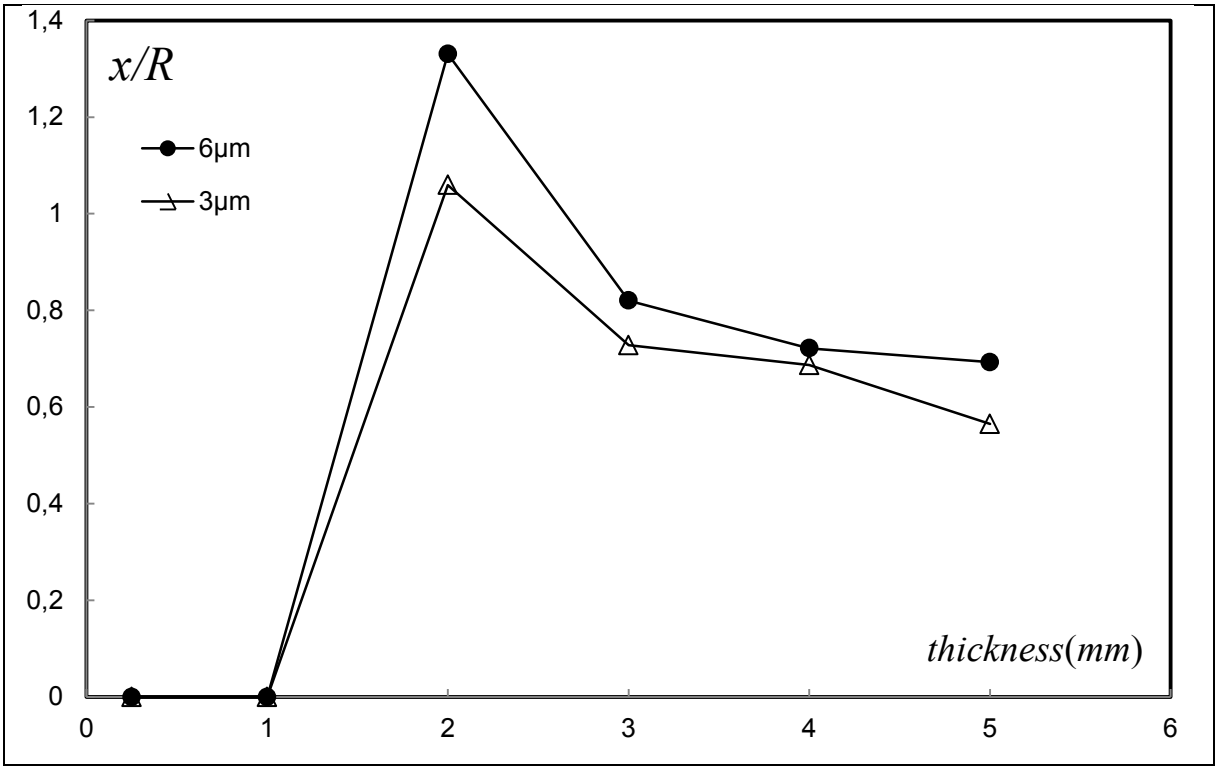

Figure III-25: Variation of the location *x* of the onset of crack location normalized by the crack notch tip radius *R* with the thickness, for Δ_{max}=3µm and 6µm.

III.6. Discussion and concluding remarks

A cohesive model is used for the description of crazing. Failure by crazing is allowed for all the samples and related thickness under consideration, starting from thin sample with t=0.25mm and t/R=1 to thick specimens up to t/R=20. The onset of craze thickening and related maximum traction for the cohesive zone debonding is reached in all cases. The load-carrying capacity of crazing allows the development of plasticity at the notch tip. Its magnitude and shape of the plastic zone depend on the thickness: for thin samples (t/R smaller that 4), a flame like profile is observed while a plastic zone similar to Hill's slip lines [HIL50, LAI97] is observed for thick specimens (t/R larger than 8). The variation of the load level in terms of stress intensity factor at the onset on debonding of the cohesive surface and the value corresponding to the nucleation of a crack locally are observed to decay for a thickness to notch radius ratio t/R=1 up to a minimum plateau as soon as t/R becomes larger than 12 to 20.

A criterion based on a local critical mean stress is motivated from a continuum analysis but has to be identified from a full 3D calculation. Gearing and Anand [GEA04] or Kattekola et al. [KAT13] used such a criterion to assess the failure by crazing, the maximum mean stress extracted shows a plateau at the onset of debonding for sufficiently thick samples. However, the magnitude of this plateau ranges from $0.6\times s_0$ to $0.8\times s_0$ corresponding to a value between 53MPa and 70MPa, well below 90MPa reported for instance by Ishikawa et al. [ISH77]. In the present analysis the maximum mean stress at the onset of debonding is governed by the magnitude of the traction T_{max} while in a continuum analysis like Ishikawa et al. [ISH77] Kattekola et al. [KAT13] the plastic deformation at the notch tip determines the level of the mean stress. Thus, large plasticity is necessary for the onset of crazing. In the present study, large plasticity is observed during debondnig, before the nucleation of a crack. The load level in terms of stress intensity factor of the onset of debonding is observed to be about 15% smaller than the fracture toughness (Figure III-10, Figure III-16, Figure III-22). The magnitude of the maximum traction at the onset of debonding is of major influences on the level of the predicted toughness, and to some extent the bulk response. The strain softening tends to trigger the fracture with a larger stress concentrates related to a more heterogeneous plastic deformation. The critical opening

related to the onset of crack nucleation is observed to have a minor influence on the material's toughness, for a given maximum traction and bulk constitutive law. The location of the crack nucleation can be used to estimate its value (Figure III-25).

The fracture toughness extracted from the 3D calculations converge to the 2D plane strain estimate, for a sufficiently large thickness. The ratio between the thickness t and the notch radius R for which a minimum toughness is observed depends on the bulk mechanical response and the maximum traction at the onset of debonding. Thus, 3D calculations are necessary to estimate whether a geometry is thick enough for the measurement of the fracture toughness. When this condition is met, 2D plane strain calculations can be carried out to analyse the crack tip fields and to attempt the identification of the cohesive model that represents crazing. The present work suggests that an estimation of the fracture toughness requires a specimen with a ratio t/R which is large enough. A value larger than 20 appears sufficient to provide a minimum estimation of the material's toughness. However, carrying out 3D calculations is necessary for the study of ductile polymer fracture.

A cohesive model for crazing in polycarbonate is not available at the moment. Its identification in the spirit of the methodology presented by Réthoré and Estevez [RET13] could provide this information, provided that plasticity from the bulk is suppressed or noticeably reduced, by performing the test at high rates or at a temperature smaller than the room temperature. An alternative is to derive the traction-separation from molecular dynamics (MD) simulations. However, experimental observations coupled to numerical analyses are necessary to derive the macroscopic toughness of a given ductile material. Specific experiments, either measurements by digital image correlation as reported by Réthoré and Estevez [RET13] or MD simulations to extract a cohesive model representative for crazing in ductile polymers remain to be developed.

REFERENCES

[ABA10] Abaqus, version 6.10-2, simulia, Dassault systems.

[AGA91] Agassant JF, Avenas P, Sergent JPh, Carreau PJ (1991) Polymer processing: principles and modelling, Hanser Gardener Pubns, Munich

[ANA03] L. Anand, M. E. Gurtin, 2003, IJSS, A theory of amorphous solids undergoing large deformations, with application to polymeric glasses 40: 1465-1487

[ARG73] Argon AS, A theory for the low-temperature plastic deformation of glassy polymers. Phil. Mag. 1973, vol. 28, pp. 839–865

[ARG77] Argon AS, Hannoosh JG, Initiation of crazes in polystyrene, Phil Mag, 1977, vol.36, pp. 1195-1216

[ARR93] Arruda EM, Boyce MC. A three-dimensional constitutive model for large stretch behaviour of rubber elastic materials. J. Mech. Phys. Solids, 1993, vol.41, pp. 389–412

[ARR95] Arruda EM, Boyce MC, Jayachandran R., Effects of strain rate, temperature and thermomechanical coupling on the finite strain deformation of glassy polymers, Mechanics of Materials, 1995, vol.19, pp. 193-2012

[BAS02] Basu S, Van der Giessen E., A thermo-mechanical study of mode I, small-scale yielding crack-tip fields in glassy polymers, Int. J. Plast., 2002, vol.18, pp. 1395–1423

[BJE03] Bjerke TW, Li Z, Lambros J., Theoretical development and experimental validation of a thermally dissipation cohesive zone model for dynamic fracture of amorphous polymers, Journal of Mechanics and Physics of Solids, 2003, vol. 51, pp.11147-1170

[BOY88] Boyce MC, Parks DM, Argon AS. Large inelastic deformation of glassy polymers. I. Rate dependent constitutive model. Mech. Mater. 1988, vol.7, pp. 15–33

[BRO73] Brown HR, Ward IM, Carze shape and fracture in poly(methyl methacrylate), Polymer, 1973, vol.14, pp. 469-475

[BRO81] Brown HR, Kramer EJ, Craza microstructure from small-angle x-ray scattering (SAXS), J. Macromol. Sci.-Phys, 1981, vol. B19(3), pp. 487-522

[BRO91] Brown HR, A molecular interpretation of the toughness of glassy polymers, Macromolecules, 1991, vol. 24(10), pp. 2752-2756

[BUC07] Bucknall C., New criterion for craze initiation, Polymer, 2007, vol. 48, pp. 1030-1041

[COR07] P.-P. Cortet, L. Vanel and S. Ciliberto, 2007, Dynamical Law for Slow Crack Growth in Polycarbonate Films, Phys Rev Lett, vol.99, p. 205502

[COR08] P.-P. Cortet, L. Vanel and S. Ciliberto, 2008, Surface oscillations and slow crack growth controlled by creep, Eur. Phys. J. vol.E 27:185–195

[DOL73] Döll W, An experimental study of the heat generated in the plastic region of a running crack in different polymeric materials, Engng Fract Mech, 1973, vol. 5, pp. 229-268

[DOL79] Döll W, Schinker MG, Könczöl L (1979) Int J. Fract 15:R145

[DOL83] Döll W, Optical interference measurements and fracture mechanics analysis of crack tip craze zones, Adv Polym Sci, 1983, vol. 52-53, pp. 105-168

[DOL90] Döll W, Könczöl L, Micromechanics of fracture: optical interferometry of crack tip craze zone. Advances in Polymer Science, 1990, vol. 91-92, pp. 138-214

[DUG60] Dugdale DS, Yielding of steel sheets containing slits, J Mech Phys Solids, 1960, vol. 8, pp. 100-101

[EST00] Estevez R, Tijssens MGA, Van der Giessen E, Modeling of the competition between shear yielding and crazing in glassy polymes, J Mech Phys Solids, 2000, vol. 48, pp. 2585-2617

[EST05] Estevez R, Basu S, Van der Giessen E, Analysis of temperature effects near mode I cracks in glassy polymers, Int J Fracture, 2005, vol. 132, pp. 249-273

[EST11] Estevez R, Long D., Probing and characterizing the early stages of cavitation in glassy polymers in molecular dynamics simulations, Model. Dimul. Mat. Sci. Engng, 2011, vol. 19, pp. 045004

[FUL75] Fuller K.N.G. , Fox P.G. , Field J.E., The temperature rise at the tip of fast-moving cracks in glassy polymers, Proc R Soc Lond A, 1975; vol. 341, pp. 537-557

[GAO04] Y.F. Gao and A.F. Bower, A simple technique for avoiding convergence problems in finite elements simulations of cracks nucleation and growth on cohesive interfaces, Modelling Simul. Mater. Sci. Eng, 2004, vol. 12, pp. 453-463

[GEA04] Gearing B.P., Anand L., Notch-sensitive fracture of polycarbonate, Int J Solids and Structures. 2004, vol.41, pp. 827–845.

[GEA04b] Gearing B.P. and Anand L., On modeling the deformation and fracture response of glassy polymers due to shear-yielding and crazing, Int J Solids Structures, 2004, vol. 41, pp.3125-3150

[HAW68] Haward RN, Thackray G, The use of a Mathematical Model to describe Isothermal Stress-Strain Curves in Glassy Thermoplastics, Proc R Soc Lond A, 1968, vol. 302, pp. 453-472

[HUI92] Hui CY, Ruina A, Creton C, Kramer EJ, Micromechanics of crack growth into a craze in a polymer glass, Macromolecules, 1992, vol.25, pp. 3948-3955

[HAS00] S. Hashemi, and J.G. Williams, Temperature dependence of essential and non-essential work of fracture parameters for polycarbonate film, Plastics, Rubber and Composites, 2000, vol.29, pp. 294-302

[HIL50] Hill.R, The mathematical theory of plasticity, reprinted in 1998 by Oxford classic series, 1950, London.

[ISH77] Ishikawa. M, Narisawa.I, Ogawa.H, Criterion for craze nucleation in polycarbonate, J. Polym. Sci., 1977, vol. 15, pp. 1791-1804

[ISH83] lshikawa. M, Narisawa. I, The effect of heat treatment on plane strain fracture of glassy Polymers, Journal of Materials Science, 1983, vol.18, pp. 2826-2834

[KAM73] Kambour RP, A review of crazing and fracture in thermoplastics, J Polymer Sci, 1973, vol.7, pp. 1-154

[KAU83] Kausch HH ed, Crazing in Polymers, Advances in Polymer Science, 1983, 52-53, Heidelberg-Berlin: Springer

[KAU87] Kausch HH, Polymer Fracture 2nd ed., Springer Berlin Heidelberg New York, 1987

[KAU90] Kausch HH ed, Crazing in Polymers Vol. 2, Advances in Polymer Science, 1990,91-92, Heidelberg-Berlin: Springer

[KRA83] Kramer E.J., Microscopic and molecular fundamentals of crazing, Adv. Polym. Sci., 1983, vol.52-53, pp. 1-56

[KRA90] Kramer E.J., Berger L.L., Craze growth and fracture, Adv. Polym. Sci., 1990, vol.91-92, pp. 1-68

[KAT13] Brunda Kattekola, Abhishek Ranjan, Sumit Basu., Three dimensional finite element investigations into the effects of thickness and notch radius on the fracture toughness of polycarbonate, Int Journal of Fracture, 2013, vol.181, pp.l-12

[KWE13] S. Kweon, A.A. Benzerga., On the localization of plastic flow in glassy polymers, European Journal of Mechanics A/Solids, 2013, vol.39, pp. 251-267

[LAU79] Lauterwasser BD, Kramer EJ, Microscopic mechanisms and mechanics of craze growth and fracture, Phil Mag A, 1979, vol.39(4), pp. 469-495

[LEE95] Leevers P.S., Impact and dynamic fracture of tough polymers by thermal decohesion in a Dugdale zone, Int J Fract, 1995, vol.73(2), pp. l09-127

[LIN08] Lindgreen B., Tvergaard V., Needleman A., Dynamic neck development in a polymer tube under internal pressure loading, Int Journal of Solids and Structures, 2008, vol.45, pp. 580-592

[LIN08b] Lindgreen B., Tvergaard V., Needleman A., Bulge formation and necking in a polymer tube under dynamic expansion, Model. Simul. Mat. Sei. Engng., 2008, vol.l6, pp. 085003 (14pp)

[LAI97] J.Lai, E.Van der Giessen, A numerical study of crack-tip fields in glassy polymers. Mechanics of Materials, 1997, vol.25, pp. 183-197.

[LU99] J. Lu and K. Ravi-Chandar, Inelastic deformation and localization in polycarbonate under Tension, Int J of Solids and Structures, 1999, vol.36, pp. 391-425.

[MAI86] Y-W MAi and B. Cotterell, On the essential work of ductile fracture in polymers, Int J Fracture, 1986, vol.32, pp.105-125.

[MAR74] Marshall GP, Coutts LH, Williams JG, Temperature effects in the fracture of PMMA, J Mat Sci, 1974, vol.9, pp. 1409-1419

[MEL03] Melick HGH.V., Govaert L.E., Meijer HEH., Localisation phenomena in glassy polymers: influence of thermal and mechanical history, Polymer, 2003, vol.44, pp. 3579-3591.

[MOR77] Morgan GP, Ward IM, Temperature dependence of craze shape and fracture in poly(methyl methacrylate), Polymer, 1977, vol.18, pp. 87-91

[MUR05] N. Murphy, A. Ivankovic, The prediction of dynamic fracture evolution in PMMA using a cohesive zone model, Engng Fract Mech., 2005, vol.72, pp. 861-875

[MUR06] N. Murphy, M. Ali, A. Ivankovic, Dynamic crack bifurcation in PMMA, Engng Fract Mech, 2006, vol.73, pp. 2569-2587

[NAR80] I. Narisawa, M. Ishikawa, H. Ogawa., Notch brittleness of ductile glassy polymers under plane strain, J. Mat. Sci., 1980, vol.15, pp. 2059-2065.

[NEE87] Needleman A, A continuum mode1 for void nucleation by inclusion debonding, J Appl Mech, 1987, vol.54(3), pp. 525-531

[NIM 92] Nimmer, R.P., Woods, J.T., An investigation of brittle failure in ductile notch sensitive Thermoplastics, Polymer Engineering and Science, 1992, vol.32, pp. 1126-1137.

[OXB73] Oxborough R.J., Bowden P.B., A general critical-strain criterion for crazing in amorphous glassy polymers, Phil. Mag., 1973, vol.28, pp. 547-559

[PAR75] Parvin M., Williams J.G., Ductile-Brittle transitions in polycarbonate, Int J Fracture, 1975, vol.11. pp. 963-972

[RAH72] Raha S, Bowden PB, Birefringence of plastically deformed poly(methyl methacrylate), Polymer, 1972, vol.l3, pp. 174-183

[PIT79] Pitman GL, Ward IM, Effect of molecular weight on craze shape and fracture toughness in polycarbonate, Polymer, 1979, vol.20, pp. 895-902

[RET13] J. Réthoré, R. Estevez, Identification of a cohesive zone model from digital images at the micron-scale, J. Mech. Phys. Sol., 2013, vol.61, pp. 1407-1420

[RIT96] Rittel D, Maigre H, An investigation of dynamic crack initiation in PMMA, Mech Mat, 1996,vol.23,pp.229

[RIT98] Rittel D, Experimental investigation of transient thermoplastic effects in dynamic fracture, Int. J. Sol Struct, 1998, vol.35, pp. 2959

[ROT02] Rottier J, Robins MO, Jamming under tension in polymer crazes, Phys Rev Let., 2002, vol.89, pp. 1955

[ROT03] Rottier J, Robins MO, Shear yielding of amorphous glassy solids: Effect of temperature and strain rate, Phys Rev E, 2003, vol.68, pp. 118

[SAA06] N Saad-Gouider, R. Estevez, C Olagnon, R. Séguéla, Calibration of a viscoplastic cohesive zone for crazing in PMMA, Eng. Fract. Mech, 2006, pp. 2503-2522.

[SCH90] Schirrer R., Optical interferometry: Running crack-tip morphologies and craze material properties. In : Crazing in Polymers , Adv Polym Sei., 1990, vol. 2, pp. 215-216

[SHA95] Sha Y, Hui CY, Ruina A, Kramer EJ., Continuum and discrete modeling of craze failure at a crack tip in a glassy polymer, Macromolecules, 1995, vol. 28, pp. 2450-2459

[SHA99] Sha Y, Hui CY, Kramer EJ., Simulation of craze failure in a glassy polymer: rate dependent drawing and rate dependent failure models, J Mat Sci., 1999, vo1.34, pp. 3695-3707

[SIH68] Sih GC Liebowitz H. In: Liebowitz H (ed) Fracture. 1968, Academic Press, San Diego, Vol.2, pp. 67

[SOC01] Socrate S, Boyce MC, Lazzeri A., A micromechanical model for multiple crazing in high impact polystyrene, Mech Mat. 2001, vol. 33, p. 155-175.

[STE69] Sternstein SS, Ongchin L., Yield criteria for plastic deformation of glassy high polymers in general stress fields, Polym Preprints., 1969, vol.10, pp. 1117-1124

[STE73] Sternstein S.S., Myers F.A., 1973, Yielding of glassy polymers in the second quadrant of principal stress space, J Macromol Sci-Phys B., 1973, vol.8, pp. 539-571

[TIJ00] Tijssens MGA, Van der Giessen E, Sluys LJ, Modeling of crazing using a cohesive surface Methodology, Mech Mat, 2000, vo1.32, pp. 19-35

[TIJ00b] Tijssens MGA, Van der Giessen E, Sluys LJ., Simulation of mode 1 crack growth in polymers by crazing, Int J Solids and Structures, 2000, vol.37, pp. 7307-7327

[TIJ02] Tijssens MGA, Van der Giessen E, A possible mechanism for cross-tie fibril generation in crazing of amorphous polymers, Polymer, 2002, vol.43, pp. 831

[TVE92] V. Tvergaard, J.W. Hutchinson, The relation between crack growth resistance and fracture process parameters in elastic-plastic solids, J. Mech. Phys. Sol., 1992, vol.40, pp.1377-1397

[TVE08] Tvergaard V., Needleman A, An analysis of thickness effects in the lzod test, Int J Solids and Structures, 2008, vol.45, pp. 3951-3966

[VAN90] Van Krevelen DW. Properties of Polymers, 3rd edn., Elsevier. 1990

[VAN97] Van der Giessen E., Localized plastic deformations in glassy polymers, European Journal of Mechanics A/Solids, 1997, vol. 16, pp. 87-106

[VAN97] Van der Giessen E, Lai J. Proc. 1Oth Int. Conf. on Deformation, Yield and Fracture of Polymers. 1997, Cambridge 35

[WAD92] Wada H, Determination of dynamic fracture toughness for PMMA, Engng Fract Mech, 1992, vol.41, pp. 821

[WAD96] Wada H, Seika M, Kennedy TC, Calder CA, Murase K, Investigation of loading rate and plate thickness effects on dynamic fracture toughness of PMMA, Engng Fract Mech, 1996, vol.54, pp. 805-812

[WEI78] Weidman GW, Doll W., Some results of optical interference measurements of critical displacements at the crack tip, Int J Fract, 1978, vol.14, pp. R189-R193

[WIL81] Williams JG, Hodgkinson JM, Crack-blunting mechanisms in impact tests on polymers, Proc R Soc Lond A, 1981, vol.375, pp. 231

[WIL84] Williams JG, Fracture Mechanics of Polymers, 1984, Ellis Horwood, New York

[Wu90] Wu.S., Chain structure, phase morphology, and toughness relationships in polymers and blends, Polym Engng Sci., 1990, vol.30, pp. 753-761

[Wu93] Wu P.D., Van der Giessen E., On improved network models for rubber elasticity and their applications to orientation hardening in glassy polymers, J. Mech. Phys. Solids, 1993, vol.41, pp. 427.

[Wu95] Wu P.D., Van der Giessen E., On neck propagation in amorphous glassy polymers under plane strain tension, Int. J. Plast, 1995, vol.ll, pp. 211-235.

[Wu96] Wu P.D., Van der Giessen E., Computational aspects of localized deformations in amorphous glassy polymers, Eur. J. Mech. A, 1996, vol.15, pp. 799-823.

CONCLUSION AND PERSPECTIVES

Extensive 3D calculations have been carried out to investigate the influence of the specimen thickness on the crack tip fields and on the onset of crack nucleation and related fracture. When a continuum analysis is carried out with no account for crazing, the stress distribution in terms of maximum mean stress and related triaxiality is observed to be noticeably dependent of the thickness. This effect is represented by the thickness t with notch radius R ratio, t/R. With increasing thickness, the magnitude of the maximum mean stress increases with the thickness up to a steady state observed for t/R larger than 40. An important observation is that the maximum mean stress estimated from 2D plane strain calculations if larger to than observed in 3D simulations, up to 15mm thick sample (t/R=60). The assumption of infinitely large samples is not met as the large bulk plasticity induces a non negligible strain contraction across the thickness, and this is observed even for 15mm thick samples. Therefore, post-processing analyses in the spirit of [ISH77, NAR80] performed in 2D for estimating the local load level at which a craze or a crack is observed need to be revisited in 3D for a realistic and accurate evaluation of a critical mean stress for the onset of failure. A stress triaxiality and thickness dependence of such criterion is likely to be observed.

When crazing is accounted for, although with a simple rate independent cohesive model as in the present work, the onset of craze initiation or crack initiation related to the observation of optically distinguishable mirror faces has to be defined carefully. Craze initiation is difficult to capture as

strictly speaking, this corresponds to nanometers large voids. In fracture tests, initiation of crazing is related to the onset of craze thickening with the formation of craze surfaces detectable optically [STE69, STE73]. In a cohesive description, this corresponds to the onset of debonding when a critical traction is attained. However, large plastic deformation develops in the bulk during the craze surface thickening up to the nucleation of a crack, at a critical opening. Once this condition is fulfilled, stress concentrates at the craze tip. This observation indicates that the definition of craze initiation in fracture tests similar to those reported by Ishikawa et al. [ISH77, NAR80], it is difficult to assess whether a craze or a crack is observed. If it corresponds to the nucleation of a crack by crazing, the traction-opening response of the craze affects noticeably the stress distribution, making difficult the definition of a local critical stress. Such criterion can be used as an indicator or the conditions for failure but its identification requires a coupled experimental study with 3D simulations.

The estimation of the condition for fracture can be estimated macroscopically for the measure of the fracture toughness. For this parameter, a t/R ratio larger than 12 or 16 seems sufficient when failure described with a cohesive model is considered. This information provides valuable information for the definition of the fracture tests configuration. The results presented in this study await for experimental investigations in which 3D observations are necessary. Recent experimental devices based on laminar X-rays tomography for the analysis of the onset of voiding can be invoked. Such direction is carried out at Centre des Matériaux (ENS Mines de Paris) in L. Laiarinandrasana's group for instance, which is thought promising for gaining insight in ductile glassy polymer fracture.

FOLIO ADMINISTRATIF

THESE SOUTENUE DEVANT L'INSTITUT NATIONAL DES SCIENCES APPLIQUEES DE LYON

NOM : **GUO** DATE de SOUTENANCE : **8 JUILLET 2013**
(avec précision du nom de jeune fille, le cas échéant)

Prénoms : **Shu**

TITRE : **Modélisation et simulation 3D de la rupture des polymères amorphes**

NATURE : Doctorat Numéro d'ordre : 2013ISAL0069

Ecole doctorale : Science des Matériaux

Spécialité : Génie des Matériaux

RESUME :

La rupture des polymères amorphes et leur ténacité sont gouvernées par la compétition entre la plasticité du matériau massif sous la forme de bandes de cisaillement et la craquelage. Ce dernier implique également de la localisation de la déformation plastique, mais à une échelle plus petite de l'ordre du micron. La rupture est qualifiée de ductile lorsqu'elle est précédée de plasticité dans le matériau massif, elle est fragile si seul le craquelage apparaît. Nous nous intéressons à l'influence des effets 3D sur le développement de la déformation plastique et sur les conditions de rupture d'un polymère amorphes ductile en menant une étude détaillée en 3D. Le polycarbonate est le matériau retenu, représentatif des polymères amorphes ductiles. Nous montrons qu'un analyse 2D sous l'hypothèse de déformation plane constitue une simplification importante pour l'étude de la plasticité autour d'une entaille dans le mesure où la forme des bandes de cisaillement est contrainte dans l'épaisseur. Ceci constitue également une restriction à l'analyse de la rupture par craquelage dans la mesure où sa germination est généralement gouvernée par un état de contrainte hydrostatique critique. Nous considérons ce problème à partir d'une analyse 3D par éléments finis (Abaqus) dans laquelle une loi de comportement réaliste pour le matériau massif. Le craquelage est décrit à l'aide d'un modèle cohésif dont les caractéristiques en termes de traction maximum et ouverture critique sont empruntés à des mesures empruntées à la littérature.
Nous proposons de caractériser les effets de géométrie avec le rapport épaisseur/rayon d'entaille. Bien que qualitativement la déformation plastique est comparable entre 2D et 3D dès que ce rapport est supérieur à 8, nous observons que les champs de contrainte estimés en 2D surestiment ceux obtenus à partir d'une analyse 3D, y compris pour des échantillons d'épaisseur aussi grande de 15mm. Les calculs 3D montrent cependant une estimation des contraintes variant peu avec l'épaisseur dès lors qu'un rapport épaisseur/rayon d'entaille est supérieur à 32. Ceci a une implication importante dans la définition d'essai de rupture. Une étude 3D s'avère nécessaire pour estimer des critères locaux de rupture comme un état de contrainte local critique pour l'apparition du craquelage. A mesure que la déformation augmente, nous observons une évolution de la forme de la zone plastique d'une allure comparable à une flamme vers celles correspondant à des bandes de cisaillement Nos résultats de simulations sont en accord avec ceux reportés dans la littérature et un critère de rupture basé sur une déformation locale critique apparaît approprié pour des conditions proches des conditions de contrainte plane.

MOTS-CLES :
Elements Finis, simulation 3D, Plasticité, Rupture, Effets géométriques

Laboratoire (s) de recherche :

MATEIS

Directeur de thèse:

C. Olagnon, Professeur INSA Lyon
R. Estevez, Professeur Université Joseph Fourier, Grenoble

Président de jury :
L. DAVID, Professeur Université Claude Bernard Lyon1

Composition du jury :
L. Laiarinandrasana, Maître de Recherches, Ecole Nationale Supérieure des Mines de Paris
F. Zaïri, Maitre de Conférences, HDR, Université de Lille 1
L. David, Professeur, Université Claude Bernard Lyon1
G. Parry, Maitre de Conférences, Grenoble INP
C. Olagnon, Professeur, INSA lyon
R. Estevez, Professeur, Université Joseph Fourier, Grenoble